TECHNISCHE UNIVERSITÄT MÜNCHEN

Lehrstuhl für Aerodynamik und Strömungsmechanik

Parameter and numerical model uncertainties of the Richtmyer-Meshkov instability

Volker Kristoff Tritschler

Vollständiger Abdruck der von der Fakultät für Maschinenwesen der Technischen Universität München zur Erlangung des akademischen Grades eines

Doktor-Ingenieurs

genehmigten Dissertation.

Vorsitzender:		Univ.-Prof. Wolfgang Polifke, Ph.D.
Prüfer der Dissertation:	1.	Univ.-Prof. Dr.-Ing. habil. Nikolaus A. Adams
	2.	Prof. Sanjiva K. Lele, Ph.D. Stanford University, USA

Die Dissertation wurde am 13.11.2014 bei der Technischen Universität München eingereicht und durch die Fakultät für Maschinenwesen am 01.07.2015 angenommen.

Volker Tritschler
Brudermühlstraße 23
81371 München
Germany

volker.tritschler@me.com

Released August 11, 2015
Typesetting LaTeX

Abstract

Shock-induced turbulent multi-material mixing plays an important role in many natural phenomena as well as in technical applications. The theoretical growth rate of the Richtmyer-Meshkov instability (RMI) suggests that it could play a significant role during the early stages of supernova remnant (SNR) formation. Kane et al. (1999) state that RMI contributes to the observed radio and X-ray structures in SNR as it leads to fast growth of non-uniformities in the stellar material and fundamentally alters the subsequent SNR formation proceü. RMI also drives the initial amplification of the Rayleigh-Taylor instability (RTI), which dominates the evolution of SNR at later times.

RMI occurs at the material interface between two fluids of different densities, when the interface is impulsively accelerated by a shock wave. The misalignment between the pressure gradient across the shock wave and the density gradient across the material interface results in baroclinic vorticity production. The deposited vorticity is the driving mechanism, which amplifies the initial perturbations at the material interface.

In the present thesis a generalized Roe average for multi-component models is proposed, which suppresses spurious pressure oscillations at material interfaces. It is shown that the recently developed WENO-CU6 scheme (Hu et al., 2009) together with the generalized Roe average introduces only very small numerical dissipation while preserving its shock-capturing properties, and hence is well-suited for simulations of shock-induced material mixing problems. Furthermore, two-dimensional simulations of the single-mode RMI are conducted and compared to experimental results. It is observed that previous single-component models fail to accurately predict the temporal flow evolution of the instability, when compared to the experiment. Thus, the proposed multi-component model increases prediction accuracy significantly over previous models.

In under-resolved simulations a substantial portion of the solution requires numerical modeling and special care must be taken in complex material mixing problems which are strongly anisotropic and inhomogeneous. The fact that most of the employed numerical models have been only validated for simple flows reduces confidence in the simulation results and in their physical interpretation. Thus, one focus of the present thesis is to provide a consistent framework for the systematic analysis of numerical model uncertainties as well as to provide a high-confidence numerical data set of shock-induced multi-material mixing problems.

The numerical modeling uncertainty introduced by subgrid-scale regularizations is investigated by studying the numerical properties and the convergence behavior of two fundamentally different numerical models, when applied to three-dimensional RMI. The initial interface perturbation between heavy and light gas is imposed spectrally exact by a

deterministic function. This approach allows to identify the physical effect of the subgrid-scale regularizations and to provide a high-confidence data set. Furthermore, spectral and temporal scalings that have been controversially discussed in literature are confirmed by demonstrating that they are recovered by both models.

On the other hand, initial-data uncertainties and their influence on the late-time evolution are largely unknown. Therefore, the other focus of this thesis is to establish a framework for the quantification of parameter uncertainties of experimental investigations through two-dimensional fully-resolved simulations of the shock accelerated heavy-gas cylinder. For this purpose a polynomial chaos expansion is coupled with a high-order compressible multi-component simulation model in order to propagate the initial-data uncertainties onto the output quantities of interest. Specifically, the effect of initial-data variations in the shock Mach number, the contamination of the heavy-gas cylinder with acetone and the initial deviation of the heavy-gas region from a perfect cylindrical shape on the mixing process is investigated. The results allow a better understanding of the fundamental connection between initial-data uncertainties and the experimentally measured output data.

Finally, direct numerical simulation results of shock-initiated material mixing are presented. These results are the first fully-resolved numerical simulations of three-dimensional RMI. The results conclusively show that a minimum critical Reynolds number has to be exceeded in order to observe a Kolmogorov inertial subrange scaling and to observe transition to turbulence. The scales of motion become clearly separated as the shock Mach number and thus the Reynolds number are increased. Furthermore, turbulence statistics such as probability density functions of the velocity and its longitudinal and transverse derivatives provide first evidence that non-homogeneous anisotropic turbulence evolving from RMI is not fundamentally different from generic isotropic homogeneous decaying turbulence.

The systematic framework for the quantification of parameter and numerical model uncertainties of shock-initiated material mixing together with the high-confidence data set from direct numerical simulations and from model comparison provides a unique tool for interpreting existing and future results. The thesis shows that the analysis of the effect of uncertainties in experimental and numerical investigations can guide to a complete and uniform understanding of RMI.

Kurzfassung

Stoß-induzierte turbulente Durchmischungsvorgänge spielen in vielen Naturphänomenen und technischen Anwendungen eine wichtige Rolle. Die theoretische Anfachungsrate der Richtmyer-Meshkov Instabilität (RMI) deutet darauf hin, dass sie speziell in der frühen Entstehungsphase von Supernovaüberresten (SNR) wichtig ist. Kane et al. (1999) vermuten, dass das durch RMI angefachte Wachstum von Störungen mitverantwortlich für die charakteristischen Strukturen im Radio- und Röntgenwellenbereich von SNR ist. Anfangsunregelmäßigkeiten in der Sternmaterie werden durch RMI schnell angefacht, wodurch der Entstehungsprozess von SNR entscheidend beeinflusst wird.

RMI tritt an der Grenzfläche zwischen zwei unterschiedlich schweren Gasen auf, wenn diese durch einen Verdichtungsstoß impulsiv beschleunigt wird. Dadurch wird baroklinische Wirbelstärke an der Materialgrenzfläche erzeugt, die zu einem Anwachsen der anfänglichen Störungen auf der Grenzfläche führt.

In der vorliegenden Arbeit wird ein verallgemeinertes Roe-Mittel für ein Mehrkomponentenmodell vorgestellt, welches unphysikalische Druckoszillationen an Materialgrenzflächen unterdrückt. Des Weiteren wird gezeigt, dass das kürzlich entwickelte WENO-CU6 Diskretisierungsschema (Hu et al., 2009) zusammen mit dem verallgemeinerten Roe-Mittel nur geringfügig zusätzliche numerische Dissipation erzeugt und die stoßabbildenden Eigenschaften des Schemas trotzdem erhalten bleiben. Aus diesem Grund ist das vorgeschlagene Roe-Mittel zusammen mit dem WENO-CU6 Schema ideal für die Simulation von stoß-induzierte Durchmischungsproblemen geeignet. Zudem werden zweidimensionale Simulationen der einfach gestörten RMI durchgeführt und mit experimentellen Ergebnissen verglichen. Dabei zeigt sich, dass Einzelkomponentenmodelle nicht in der Lage sind die korrekte zeitliche Entwicklung der Instabilität vorherzusagen. Daher stellt das vorgeschlagene Mehrkomponentenmodell eine signifikante Verbesserung der Vorhersagegenauigkeit gegenüber früherer Modelle dar.

In unter-aufgelösten Simulationen wird ein beträchtlicher Anteil der Lösung numerisch modelliert. Insbesondere bei komplexen Durchmischungsvorgängen, die stark anisotrop und inhomogen sind, hat die Modellierung entscheidenden Einfluss auf die Lösung. Die Tatsache, dass die meisten der verwendeten numerischen Modelle jedoch nur für einfache Strömungen validiert wurden, reduziert das Vertrauen in die Simulationsergebnisse. Ein Schwerpunkt der vorliegenden Arbeit ist somit den Vertrauensbereich der numerischen Modelle auf komplexe Durchmischungsvorgänge zu erweitern. Dies wird durch ein Framework zur systematischen Analyse von numerischen Modellunsicherheiten erreicht. Darüber hinaus werden hochgenaue Benchmark-Daten präsentiert, die zur Entwicklung von verbesserten numerischen Modellen verwendet werden können.

Die durch die feinskalige Regularisierung verursachte numerische Modellunsicherheit wird durch den Vergleich zweier grundlegend verschiedener numerischer Modelle untersucht. Zu diesem Zweck werden beide Modelle zur Simulation der dreidimensionalen RMI verwendet und einer quantitativen Analyse unterzogen. Die dafür benötigte Anfangsstörung an der Grenzfläche zwischen schwerem und leichtem Gas wird durch eine deterministische Funktion beschrieben. Die Funktion kann für beide Modelle spektral exakt verwendet werden und erlaubt somit einen direkten quantitativen Vergleich. Dieser Ansatz ermöglicht die Identifikation des physikalischen Einflusses der Regularisierung im feinskaligen Bereich.

Zum anderen sind die Parameterunsicherheiten in experimentellen Untersuchungen größtenteils unbekannt. Daher ist ein anderer Fokus dieser Arbeit ein Framework zur Quantifizierung von Parameterunsicherheiten durch voll-aufgelöste zweidimensionale Simulationen eines durch einen Verdichtungsstoß beschleunigten Gaszylinders zu etablieren. Dazu wird die Polynomial-Chaos-Expansion mit einem kompressiblen Mehrkomponenten-Simulationsmodell gekoppelt, um die Unsicherheiten in den Anfangsbedingungen auf die Zielgrößen zu transportieren. Dabei werden insbesondere die Auswirkungen der Varianz in der Stoßmachzahl, in der Verunreinigung des Gaszylinders mit Aceton und in der anfänglichen Abweichung des Gaszylinders von einer idealen Zylinderform auf den Durchmischungsvorgang untersucht. Die vorgestellten Ergebnisse ermöglichen ein besseres Verständnis des grundlegenden Zusammenhangs zwischen der Unsicherheit in den Anfangsbedingungen und der Varianz in den gemessenen Zielgrößen.

Abschließend werden noch Ergebnisse direkter numerischer Simulationen von stoß-induzierten dreidimensionalen Durchmischungsvorgängen vorgestellt. Diese Ergebnisse stellen die ersten voll-aufgelösten numerischen Simulationen der dreidimensionalen RMI dar. Die Ergebnisse zeigen, dass eine kritische Reynolds-Zahl überschritten werden muss um Turbulenztransition zu beobachten. Die turbulenten Längenskalen der Strömung separieren sich zunehmend, wenn die Stoßmachzahl und somit die Reynolds-Zahl erhöht werden. Zudem werden Wahrscheinlichkeitsdichtefunktionen der Geschwindigkeit und deren Ableitungen in Längs- und Querrichtung präsentiert. Diese belegen eindeutig, dass sich stoß-induzierte Turbulenz ähnlich zu abklingender homogener isotroper Turbulenz verhält.

Das vorgestellte Framework zur Quantifizierung von Parameter- und numerischer Modellunsicherheiten in stoß-induzierte Durchmischungsvorgängen, zusammen mit den hochgenauen Simulationsdaten aus direkten numerischen Simulationen, stellt ein einzigartiges Werkzeug für die Interpretation bestehender und zukünftiger Ergebnisse dar. Nur die detaillierte Analyse von Unsicherheiten und deren Auswirkung in experimentellen und numerischen Untersuchungen kann zu einem einheitlichen und umfassenden Verständnis von RMI führen.

Danksagung

Die vorliegende Dissertation entstand während meiner Zeit als wissenschaftlicher Mitarbeiter am Lehrstuhl für Aerodynamik und Strömungsmechanik der Technischen Universität München. An dieser Stelle möchte ich gerne einigen Menschen danken, die einen ganz besonderen Anteil am Gelingen dieser Arbeit hatten.

Zuallererst möchte ich meinem Doktorvater Professor Nikolaus Adams für seine Betreuung und das inspirierende wissenschaftliche Umfeld am Lehrstuhl danken. Er hat mich jederzeit in all meinen Vorhaben und Ideen unterstützt und mir dadurch gezeigt wie viel Freude Forschung bereiten kann. Insbesondere bin ich ihm für das Ermöglichen der Kooperation mit Professor Sanjiva Lele und dem damit verbundenen, und für mich sehr motivierenden, Aufenthalt an der Stanford University dankbar.

I also wish to thank Professor Sanjiva Lele for the pleasant time at Stanford University as well as for the fruitful collaboration. Sanjiva had always been a source of inspiration and wisdom throughout the past two years of my Ph.D. It is a great honor for me that he accepted to co-examine my thesis.

Xiangyu and Stefan, I also want to thank you for all your help and support during my time at the institute.

Was meine Promotion allerdings zu einer unvergesslichen Zeit gemacht hat, waren all die wunderbaren Freunde, Kollegen und Leidensgenossen am Lehrstuhl. Für immer in meiner Erinnerung bleiben all die grundlosen Feiern, Geburtstagsfeiern, ESPs, die Weinverkostung mit dem Preisleistungssieger aus Mazedonien und natürlich die haushoch verlorene Kneipenolympiade gegen den Lehrstuhl für Thermodynamik!

Den aller wichtigsten Anteil am Gelingen dieser Arbeit hat allerdings meine Familie. Ohne ihre Unterstützung während der letzten Jahre wäre ein Gelingen dieser Arbeit nicht denkbar gewesen. Ganz besonders möchte ich mich jedoch bei Bine für all die wundervollen zurückliegenden Jahre und ihre stete und bedingungslose Unterstützung bedanken.

Table of contents

1. Introduction

This thesis summarizes my work of the past four years at the Institute of Aerodynamics and Fluid Mechanics at the Technische Universität München. The first objective of the thesis was to establish a numerical framework for the investigation of shock initiated mixing processes and second, to study the physical mechanism of these mixing processes. It turned out that uncertainties in experimental investigations, e.g., unclear initial and boundary conditions as well as numerical model uncertainties and truncation errors play a crucial role for the fundamental understanding of shock-initiated mixing processes. Thus, the second objective became twofold: besides the physical mechanism of shock-initiated mixing processes, also the uncertainties in numerical and experimental investigations were analyzed.

The thesis is structured as follows: In this chapter a brief introduction to the Richtmyer-Meshkov instability (RMI) and to computational fluid dynamics is provided as well as a literature overview of the state-of-the-art in RMI research with special emphasis on numerical model and parameter uncertainties. In chapter 2 the numerical model is summarized including the governing equations, i.e., the Navier-Stokes equations and the multi-component mixing rules. Details about the flux reconstruction scheme and the time integration scheme are also given. In chapter 3 the main contributions of the present thesis are provided together with a short introduction for each publication. The last chapter 4 summarizes the key findings of this work. A full list of all publications is provided in appendix A and the selected main publications are attached in appendix B.

1.1. The Richtmyer-Meshkov instability

When a heavy fluid is accelerated into a lighter fluid by gravitational forces, the instability occurring at the material interface between the two fluids is known as Rayleigh-Taylor instability (Rayleigh, 1883; Taylor, 1950). A theoretical prediction for the growth rate of the initial interfacial perturbations was provided by Taylor (1950) in 1950. Richtmyer (1960) extended the theoretical prediction of Taylor (1950) to the impulsive acceleration of material interfaces. Richtmyer's predictions were later experimentally verified by Meshkov (1969) and the instability arising from the impulsive acceleration of a perturbed material interface is thus referred to as the Richtmyer-Meshkov instability (RMI).

Richtmyer (1960) replaced the constant gravitational acceleration g in the original model of Taylor (1950) by an impulsive acceleration $\Delta u \delta(t)$. From this, the early linear growth rate $\partial a/\partial t$ of a single-mode perturbation with wavenumber k follows as

$$\frac{\partial a}{\partial t} = k \Delta u A^{+} a_0^{+} \quad , \tag{1.1}$$

where a_0^{+} is the initial post-shock amplitude of the perturbed interface and $A^{+} = (\rho_1 - \rho_2)/(\rho_1 + \rho_2)$ is the post-shock Atwood number. Following Richtmyer's impulsive model other more advanced theoretical models have been proposed, like the perturbation model (Zhang and Sohn, 1997). Zhang and Sohn (1997) model the early time dynamics of the interface by the linear, compressible flow equations and the late times by the non-linear, incompressible flow equations. Mikaelian (2003) again derived a growth rate model for the late non-linear regime through the potential flow equations. A very concise overview of the different existing theoretical models and their predictive accuracy compared to numerical simulation results is given by Latini et al. (2007a).

The vorticity transport equation of a compressible flow is given as

$$\frac{D\boldsymbol{\omega}}{Dt} = (\boldsymbol{\omega} \cdot \nabla)\, \boldsymbol{u} - \boldsymbol{\omega}\, (\nabla \cdot \boldsymbol{u}) + \frac{1}{\rho^2} (\nabla \rho \times \nabla p) + \nu \nabla^2 \boldsymbol{\omega} \quad . \tag{1.2}$$

The fact that the vorticity is initially zero ($\boldsymbol{\omega} = 0$) in the flow field suggests that a non-vanishing baroclinic vorticity production term $(\nabla \rho \times \nabla p)/\rho^2$ at the material interface is the initial driving mechanism of RMI. Thus, the misalignment of the pressure gradient ∇p associated with the shock wave and the density gradient $\nabla \rho$ associated with the density variation across the material interface results in $(\nabla \rho \times \nabla p)/\rho^2 \neq 0$. The vorticity deposition leads to a growth of the initial interface perturbations, and if the initial energy input is sufficient the flow evolves eventually into a turbulent mixing zone through non-linear interactions of the material interface perturbations. For a more complete review of RMI the reader is referred to Brouillette (2002).

RMI occurs on a wide range of scales which cover the largest in astrophysics (Arnett et al., 1989; Arnett, 2000; Almgren et al., 2006; Kane et al., 1999; Ingogamov, 1999), the intermediate scales in supersonic combustion engines (Yang et al., 1993; Khokhlov et al., 1999; Yang et al., 2014) and the very small scales in inertial confinement fusion experiments (Lindl et al., 1992; Taccetti et al., 2005; Aglitskiy et al., 2010).

In the work of Kane et al. (1999) the authors conclude that RMI contributes to the observed radio and X-ray structures in supernova remnant (SNR) formation as detected in the multi-wavelength composite image of Tycho's supernova, see Fig. 1.1. The theoretical models of RMI suggest that it plays an important role during the early stages of the formation of SNR as the instability strongly amplifies non-uniformities in the stellar material. At later times the SNR formation is dominated by the Rayleigh-Taylor instability, which benefits from the initial amplifications from RMI. According to the findings of Kane et al. (1999) the combined impact of RTI and RMI needs to be included in standard SNR models.

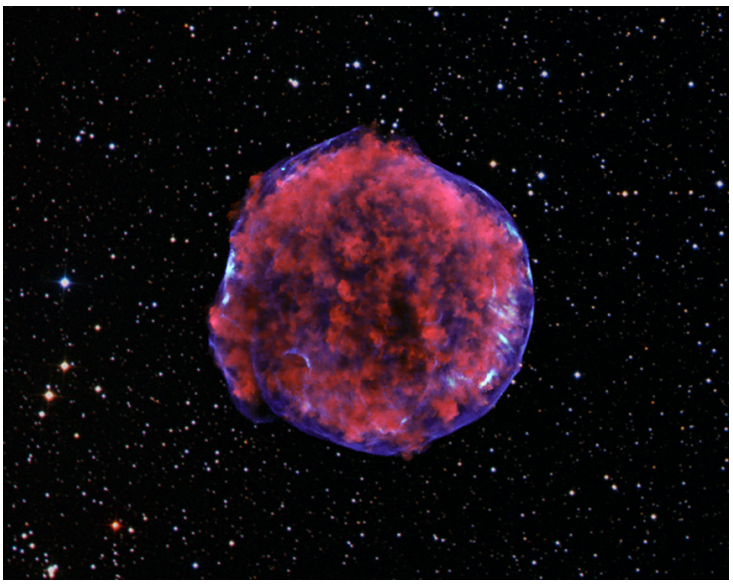

Figure 1.1.: Multi-wavelength composite image of the remnant formation of Tycho's supernova taken by the Chandra X-Ray Observatory [NASA/CXC/Rutgers/J. Warren & J. Hughes et al.].

A virtually identical fluid mechanical behavior is observed on the smallest scales in inertial confinement fusion (ICF) experiments. In ICF, laser beams are used to heat up the outer layer of a fuel containing target capsule. The experimental setting is designed such that inward traveling shock waves are created which compress the fuel inside the capsule. The dramatic increase of pressure and temperature of the fuel eventually results in a fusion reaction. RMI, however, causes an undesired mixing between the shell material of the capsule and the fuel within. This leads to a significant reduction in energy release and prevents energy break-even. A very recent publication (Hurricane et al., 2014) reported an energy gain exceeding unity in an ICF experiment. The experiment achieved an order-of-magnitude increase of energy release over past experiments by manipulating the laser pulse shape such that it reduces instabilities of Rayleigh-Taylor and Richtmyer-Meshkov type during implosion.

1.2. Computational fluid dynamics

Computational fluid dynamics (CFD) is a branch of computer-aided predictive science. Physical systems are abstracted with mathematical models, discretized and solved numerically on a computer with the objective to predict the behavior of the physical system.

In CFD, research is concerned with the development of accurate and efficient computational algorithms on one hand and on gaining new physical insight into the physics of fluid mechanics on the other hand. CFD has gained significant importance in industry and will become even more important in the near future thanks to increased computational resources. For an introduction to fluid mechanics the reader may consider the book of Smits (2000). A very comprehensive introduction to computational fluid dynamics is given in each of the following references, e.g., Anderson et al. (1995); Ferziger and Perić (2002); Versteeg and Malalasekera (2007).

The temporal and spatial evolution of fluid flows is described by a set of partial differential equations, namely the Navier-Stokes equations. In order to solve these equations numerically, the continuous equations are transformed into a set of discrete equations which can be solved iteratively. The spatial and temporal derivatives imply an approximation of the exact continuous derivatives. Thus, the truncation error of the discrete derivatives determines the accuracy of the numerical method.

If the truncation error of the numerical method has a marginal effect on the flow dynamics the simulations are referred to as direct numerical simulations (DNS). If the truncation error, however, is not small but has a significant effect on the resolved flow scales the simulations are referred to as under-resolved direct numerical simulations. Because under-resolved simulations do not capture all flow scales, the non-resolved scales have to be regularized. These subgrid-scale regularizations may have, as we will see later, a significant effect on the flow evolution, especially in multiscale problems such as RMI. Simulations in which the energy containing large scales are resolved, whereas the non-resolved small-scales are not only regularized but modeled, are referred to as large eddy simulations (LES). An introduction to LES can be found in the book of Sagaut (2002).

1.3. Uncertainties of the Richtmyer-Meshkov instability

A key issue in computer-aided predictive science is the quantification of the confidence level of numerical predictions, as the computer model only approximates the corresponding true physical system.

When a physical system is translated into a mathematical formulation and subsequently into a numerical algorithm different types of uncertainties arise. Firstly, the mathematical formulation requires model parameters to describe the physical behavior of the original system and these model parameters are subject to uncertainties. Also, simply the lack of knowledge of the underlying physical mechanism (the mathematical formulation might

not reflect all properties of the original system) results in uncertainty. Finally, when the mathematical formulation is translated into a numerical algorithm truncation and round-off errors, numerical model assumptions, as well as implementation mistakes increase the prediction uncertainty.

On the other hand, in experimental investigations the initial and boundary conditions cannot be fully controlled and allow for statistical and systematic uncertainties. As uncertainties in the initial conditions are non-linearly amplified with time, these uncertainties can have a significant effect on the flow evolution. The measuring apparatus can also increase the uncertainties in experimental results.

In RMI investigations numerical model uncertainties and parameter uncertainties dominate. Numerical model uncertainties are, e.g., numerical modeling assumptions and truncation errors, which are introduced by the discretization and the numerical solving procedure of the continuous exact equations. Parameter uncertainties are uncertainties in the input parameters, e.g. initial conditions and material properties, whose exact values are not precisely known to the experimentalist.

The methodology of uncertainty quantification (UQ) identifies and characterizes the overall output uncertainty of a numerical prediction based on the variability of the input parameters of a given physical system. Thus, UQ is the generic term for determining how likely a result is, given that not all aspects of the physical system are known and can only be described in a statistical sense. UQ is closely related to sensitivity analysis which connects the variability of an input quantity to an output quantity of interest, however, without considering the specific input uncertainty of the physical system.

1.3.1. Numerical model uncertainties

In 1994 Brouillette and Sturtevant (1994) experimentally investigated RMI evolving from a single-mode initial perturbation in a square shock tube and quantified the mixing zone growth rate of the initially diffused sinusoidal interface separating the gases. The authors showed that the growth rate is inversely proportional to the initial thickness of the material interface. Due to limitations in the spatial and temporal resolution capabilities of experimental diagnostic techniques, integral quantities like the mixing zone width and qualitative information from Schlieren imaging were the only accessible information in early experiments. Until today, it remains difficult to capture the evolution of a fully three-dimensional turbulent mixing zone in experimental investigations. Therefore, insight into the flow physics of RMI relies to a considerable extent on numerical investigations.

Because of the relatively high Reynolds numbers and the associated small Kolmogorov length scales under-resolved simulations and LES have become the state-of-the-art approaches to investigations of shock-induced turbulent mixing problems. The subgrid-scale regularization used in LES and in under-resolved simulations significantly affect the predicted material mixing transition and the late-time mixing evolution. The regularization models not only the interaction of resolved and non-resolved scales but also captures discontinuities such as shock waves and material interfaces. Due to the broad range of spatial and temporal scales numerical simulations of RMI strongly rely on the resolution

capabilities of the underlying numerical scheme for the different types of subgrid scales, i.e., turbulent small scales, shocks, interfaces. Thus, the overall numerical uncertainty is a combination of the subgrid-scale regularization and the truncation error of the discretization scheme. This is particularly important as all numerical models involve some kind of subgrid-scale regularization and are affected by numerical truncation errors.

Grinstein et al. (2011) used an implicit LES (ILES) model to study three-dimensional material mixing initiated by a shock wave. This ILES model is based on a second-order Godunov-type numerical scheme and uses additionally a van Leer limiter as a gradient term limiter. The primary goal of this investigation was to understand the performance of ILES models in under-resolved material mixing and the effects of specific initial conditions on the transitional and late-time mixing. Also, Thornber et al. (2010) used an implicit LES approach (Drikakis, 2003; Thornber et al., 2008; Drikakis et al., 2009) based on a finite-volume Godunov-type method. This numerical framework was used to study the influence of different three-dimensional broad- and narrowband multi-mode initial conditions on the growth rate of a turbulent multi-component mixing zone developing from RMI. In a later study (Thornber et al., 2011) the same authors presented a numerical study of a re-shocked turbulent mixing zone, and extended the theory of Mikaelian and Youngs to predict the behavior of a multi-component mixing zone before and after re-shock, c.f. Mikaelian (1989) and Thornber et al. (2010). Hill et al. (2006) performed a detailed numerical investigation of RMI including re-shock. The authors used an improved version of the TCD-WENO hybrid method of Hill and Pullin (2004). The method employs a switch to blend explicitly between a tuned centered-difference (TCD) stencil in smooth flow regions and a weighted essentially non-oscillatory (WENO) shock capturing stencil at discontinuities. The TCD-WENO hybrid method is used together with the stretched-vortex model (Pullin, 2000; Kosović et al., 2002) for explicitly modeling the subgrid interaction terms. This approach was also used by Lombardini et al. (2011) to study the impact of the Atwood number for a canonical three-dimensional numerical setup, and for LES of a single-shock (i.e. without re-shock) RMI (Lombardini et al., 2012).

All these investigations have applied explicit or implicit subgrid-scale modeling approaches for the investigation of shock-driven mixing processes evolving from RMI with special emphasis on initial-condition parameters such as the shock Mach number, the initial interface perturbation or the Atwood number and how these parameters affect the evolution of the instability. However, the physical effect of the specific subgrid-scale regularization remains unclear and guidance is needed in interpreting the obtained results. Turbulent mixing initiated by RMI mainly occurs at the marginally resolved and non-resolved scales. Particularly, it remains unclear which effect the marginally and non-resolved scales have on the evolution of the instability, as numerical modeling uncertainties have not yet been investigated systematically. So far, all investigations have assumed that the numerical models validated for more simple flows also accurately work for RMI and based on empirical resolution criteria that the employed resolution allow accurate prediction of the instability. However, for the correct interpretation of numerical simulation results it is of fundamental importance to clearly divide between physics as a result of the solution of the Navier-Stokes equations and numerical errors with physical interpretation.

1.3.2. Parameter uncertainties

As outlined in the previous section under-resolved simulations are dominated by numerical model uncertainties due to the employed subgrid-scale regularization and discretization errors. On the experimental side uncertainties exist primarily due to unknown or not precisely known initial and boundary conditions.

Haas and Sturtevant (1987) were the first, who investigated the interaction of shock waves with a gas bubble filled with either He or R_{22}. The authors presented qualitative shadow-photographs of the bubble evolution. Later, Quirk and Karni (1996) conducted a detailed numerical investigation of this shock-bubble interaction problem and complemented the experimental findings in a qualitative sense by numerically reproducing the transition from regular to irregular refraction, the shock wave focusing and the formation of a jet towards the inside of the bubble. Only qualitative agreement was obtained, mainly because the initial conditions could not be accurately prescribed and characterized in the experiment.

More than a decade later Jones and Jacobs (1997) developed a technique to impose arbitrary experimental initial conditions without using a plastic membrane to initially separate the gases. This membrane-free technique allows well defined experimental initial conditions with precisely prescribed interface perturbations. In the experimental investigations of the shock-cylinder interaction of Tomkins et al. (2008) and the single-mode RMI of Collins and Jacobs (2002) high-fidelity contour maps were recorded by planar laser induced fluorescence (PLIF) measurements and through accurately and reproducibly defined initial conditions using the membrane-free technique of Jones and Jacobs (1997). Tomkins et al. (2008) did not only present contour maps of the heavy gas concentration but also quantified the scalar dissipation rate for the first time experimentally.

Due to technical improvements in imaging diagnostics, particle image velocimetry (PIV) (Prestridge et al., 2000) and PLIF (Collins and Jacobs, 2002; Tomkins et al., 2008; Weber et al., 2012) can provide velocity and density fields which yield a much more detailed view on the turbulent mixing process. Also, the simultaneous PLIF and PIV measurement (Balakumar et al., 2008; Balasubramanian et al., 2012) proved its usefulness to fully characterize the mixing process of variable density flows (Orlicz et al., 2013). For a comprehensive review on experimental diagnostic techniques as well as an outlook on future directions in experiments of shock-driven turbulent mixing the reader is referred to Prestridge et al. (2013).

The progress of ever increasing resolving capabilities of the imaging techniques and better defined initial conditions allowed to study RMI down to the small scales and to understand the physical mechanism to an unprecedented level of detail. Despite the technical improvements RMI is lacking a uniform physical picture supported by both experimental and numerical investigations and predictive agreement is still only achieved in a qualitative sense.

Shankar et al. (2011) presented fully-resolved numerical results of the shock-cylinder interaction employing the initial conditions of the experiment of Tomkins et al. (2008).

But they failed to accurately predict the characteristic temporal evolution of the experiment, even though they accounted for an initial-data variability. Shankar et al. (2011) hypothesized that the initial-data variability is the key element to be able to reproduce the experiment quantitatively. In their investigation the authors varied the initial shape of the gas cylinder as well as the initial contamination of the gas cylinder with acetone.

This investigation clearly demonstrates that experimental uncertainties play a key role in understanding the discrepancies between numerical simulation results and experiments. As it will remain difficult to precisely impose initial and boundary conditions in a laboratory experimental investigation and to accurately resolve the evolution of the instability in space and time. Thus, in order to obtain a uniform picture experimental initial-data uncertainties need to be studied and quantified.

1.4. Objectives

The first objective of the present work is to develop a numerical framework suitable for shock-induced material mixing problems. Specifically, the recently proposed reconstruction scheme of Hu et al. (2010) and Hu and Adams (2011) needs to be coupled with a low-dissipation and highly accurate multi-component model.

The second objective is to analyze the physical effect of numerical errors (truncation errors and subgrid-scale regularization) on the marginally resolved to resolved scale range as these uncertainties can have physically meaningful interpretations. Knowing the effect of numerical modeling uncertainties will provide guidance in interpreting numerical investigations as this will allow to distinguish between real physics and numerical effects with physical interpretation.

The third objective is to characterize the effect of initial-data uncertainties in experimental investigations on the measured flow quantities and to provide an explanation for the observed quantitative difference between experimental and numerical investigations.

The fourth objective, finally, is to provide results from direct numerical simulations to study RMI initiated multi-material mixing down to the smallest scales and to provide a high-confidence data set, which can be used as reference for, e.g., future numerical model development and model validation.

A benchmark data set together with a consistent framework for parameter and numerical model uncertainty quantification provides the missing toolbox to (i) understand the effect of numerical model uncertainties on the evolution of RMI and to improve and adapt existing numerical models to shock initiated material mixing, to (ii) understand the influence of initial-data uncertainties in experimental investigations, and finally (iii) to gain insight into RMI initiated mixing down to the smallest scales, obtaining a uniform, consistent and complete understanding of the underlying physical mechanism.

2. Numerical model

In this chapter the governing equations and the multi-component mixing rules are summarized together with further details on the numerical approach.

2.1. Governing equations

In the present thesis the full set of compressible multi-component Navier-Stokes equations are solved. This approach has been used in all separate sub-investigations (Tritschler et al., 2013a, 2014a,b,c) except in Tritschler et al. (2013b), where a new generalized Roe average in a non-conservative formulation is proposed.

The governing equations are given by the continuity equation, the momentum equation in three space dimensions, the energy equation and one transport equation for each species. Thus, the full set of equations reads as

$$\frac{\partial \boldsymbol{U}}{\partial t} + \nabla \cdot \boldsymbol{F}(\boldsymbol{U}) = \nabla \cdot \boldsymbol{F}_\nu(\boldsymbol{U}) \quad , \tag{2.1}$$

with

$$\boldsymbol{U} = \begin{pmatrix} \rho \\ \rho \boldsymbol{u} \\ E \\ \rho Y_i \end{pmatrix}, \quad \boldsymbol{F}(\boldsymbol{U}) = \begin{pmatrix} \rho \boldsymbol{u} \\ \rho \boldsymbol{u}\boldsymbol{u} + p\underline{\boldsymbol{\delta}} \\ (E+p)\boldsymbol{u} \\ \rho \boldsymbol{u} Y_i \end{pmatrix}, \quad \boldsymbol{F}_\nu(\boldsymbol{U}) = \begin{pmatrix} 0 \\ \underline{\boldsymbol{\tau}} \\ \underline{\boldsymbol{\tau}} \cdot \boldsymbol{u} - \boldsymbol{q_c} - \boldsymbol{q_d} \\ \boldsymbol{J_i} \end{pmatrix} \quad . \tag{2.2}$$

In Eq. (2.2) $\boldsymbol{u} = [u, v, w]$ is the velocity vector, p is the pressure, E is the total energy, ρ the mixture density and Y_i is the mass fraction of species $i = 1, 2, ...N$ with N as the total number of species. The identity matrix is given by $\underline{\boldsymbol{\delta}}$. The viscous stress tensor $\underline{\boldsymbol{\tau}}$ is defined for a Newtonian fluid as

$$\underline{\boldsymbol{\tau}} = 2\overline{\mu}\left[\underline{\boldsymbol{S}} - 1/3\underline{\boldsymbol{\delta}}\left(\nabla \cdot \boldsymbol{u}\right)\right] \quad , \tag{2.3}$$

with the mixture viscosity $\overline{\mu}$ and the strain rate tensor $\underline{\boldsymbol{S}}$. According to Fourier's law we define the heat conduction as

$$\boldsymbol{q_c} = -\overline{\kappa}\nabla T \tag{2.4}$$

with $\overline{\kappa}$ being the mixture heat conductivity and the inter-species diffusional heat flux (Cook, 2009) defined as

$$\boldsymbol{q_d} = \sum_{i=1}^{N} h_i \boldsymbol{J_i} \tag{2.5}$$

with

$$\boldsymbol{J_i} \approx -\rho\left(D_i \nabla Y_i - Y_i \sum_{j=1}^{N} D_j \nabla Y_j\right) \quad . \tag{2.6}$$

h_i and D_i indicate the individual species enthalpy and the individual species effective binary diffusion coefficient. The equations are closed with the equation of state for an ideal gas

$$p(\rho e, Y_i) = \left(\overline{\gamma} - 1\right)\rho e \quad , \tag{2.7}$$

where $\overline{\gamma}$ is the ratio of specific heat capacities of the mixture and e is the internal energy

$$\rho e = E - \frac{\rho}{2}\boldsymbol{u}^2 \quad . \tag{2.8}$$

The species specific viscosity μ_i is calculated by the Chapman-Enskog viscosity model

$$\mu_i = 2.6693 \cdot 10^{-6}\frac{\sqrt{M_i T}}{\Omega_{\mu,i}\sigma_i^2} \quad , \tag{2.9}$$

where σ_i is the collision diameter and $\Omega_{\mu,i}$ is the collision integral (Neufeld et al., 1972) given as

$$\Omega_{\mu,i} = A(T_i^*)^B + C\exp\left\{DT_i^*\right\} + E\exp\left\{FT_i^*\right\} \quad , \tag{2.10}$$

with $A = 1.16145$, $B = -0.14874$, $C = 0.52487$, $D = -0.7732$, $E = 2.16178$ and $F = -2.43787$, where $T_i^* = T/(\epsilon/k)_i$ and with $(\epsilon/k)_i$ being the Lennard-Jones energy parameter.

The mass diffusion coefficient of a binary mixture is calculated from the empirical law (Poling et al., 2001)

$$D_{ij} = \frac{0.0266}{\Omega_{D,ij}}\frac{T^{3/2}}{p\sqrt{M_{ij}}\sigma_{ij}^2} \tag{2.11}$$

with the collision integral for diffusion

$$\Omega_{D,ij} = A(T_{ij}^*)^B + C\exp\left\{DT_{ij}^*\right\} + E\exp\left\{FT_{ij}^*\right\} + G\exp\left\{HT_{ij}^*\right\} \quad , \tag{2.12}$$

where $T^*_{ij} = T/T_{\epsilon_{ij}}$ and $A = 1.06036$, $B = -0.1561$, $C = 0.193$, $D = -0.47635$, $E = 1.03587$, $F = -1.52996$, $G = 1.76474$, $H = -3.89411$ and

$$M_{ij} = \frac{2}{\frac{1}{M_i} + \frac{1}{M_j}} \quad , \quad \sigma_{ij} = \frac{\sigma_i + \sigma_j}{2} \quad , \quad T_{\epsilon_{ij}} = \sqrt{\left(\frac{\epsilon}{k}\right)_i \left(\frac{\epsilon}{k}\right)_j} \quad . \tag{2.13}$$

The thermal conductivity κ_i is obtained from the species specific Prandtl number Pr_i as

$$\kappa_i = c_{p,i} \frac{\mu_i}{Pr_i} \tag{2.14}$$

where $c_{p,i}$ is the specific heat capacity, which results from

$$c_{p,i} = \frac{\gamma_i}{\gamma_i - 1} R_i \quad \text{, with} \quad R_i = \frac{\mathcal{R}}{M_i} \quad , \tag{2.15}$$

All thermodynamic gas properties are taken from Poling et al. (2001). The ratio of specific heat capacities of the mixture $\overline{\gamma}$ is calculated as

$$\overline{\gamma} = \frac{\overline{c_p}}{\overline{c_p} - \overline{R}} \quad \text{, with} \quad \overline{c_p} = \sum_i^N Y_i c_{p,i} \quad . \tag{2.16}$$

The specific gas constant of the mixture $\overline{R} = \mathcal{R}/\overline{M}$ is calculated from the molar mass of the mixture which is given by

$$\overline{M} = \left(\sum_i^N \frac{Y_i}{M_i} \right)^{-1} \quad . \tag{2.17}$$

For the gas mixture Dalton's law $p = \sum_i p_i$ shall be valid with $p_i = \rho R_i T$. The viscosity $\overline{\mu}$ and the heat conductivity coefficient $\overline{\kappa}$ of the mixture is calculated according to Wilke (1950) with Herning and Zipperer's approximation (Herning and Zipperer, 1936)

$$\overline{\mu} = \frac{\sum_{i=1}^N \mu_i Y_i / M_i^{1/2}}{\sum_{i=1}^N Y_i / M_i^{1/2}} \quad , \quad \overline{\kappa} = \frac{\sum_{i=1}^N \kappa_i Y_i / M_i^{1/2}}{\sum_{i=1}^N Y_i / M_i^{1/2}} \quad , \tag{2.18}$$

see also Poling et al. (2001). The effective binary diffusion coefficients of species i is approximated as (Ramshaw, 1990)

$$D_i = (1 - X_i) \left(\sum_{i \neq j}^N \frac{X_j}{D_{ij}} \right)^{-1} \quad , \tag{2.19}$$

where X_i is the mole fraction of species i. Eq. (2.19) ensures that the inter-species diffusion fluxes balance to zero.

2.2. Numerical scheme

The hyperbolic part of the Navier-Stokes equations can be considered as a Riemann problem which consists of a partial differential equation describing a conservation law with piecewise constant initial condition and a single discontinuity. There are two different types of Riemann solvers, exact and approximate ones. Roe's approximate Riemann solver (Roe, 1981) and the HLL (Harten-Lax-van Leer) solver (Harten et al., 1987) are the most common approximate Riemann solvers. In the original formulation of Roe's approximate Riemann solver the corresponding Roe-averaged matrix is derived only for a single-component fluid. In the present thesis Roe's approximate Riemann solver for a multi-component system is used to compute the inter-cell flux.

A non-linear system of hyperbolic partial differential equations

$$\frac{\partial \boldsymbol{U}}{\partial t} + \frac{\partial \boldsymbol{F}(\boldsymbol{U})}{\partial x} = 0 \tag{2.20}$$

can be transformed into a set of quasi-linear hyperbolic equations by applying the chain rule

$$\frac{\partial \boldsymbol{U}}{\partial t} + \boldsymbol{A}(\boldsymbol{U})\frac{\partial \boldsymbol{U}}{\partial x} = 0 \quad , \tag{2.21}$$

where $\boldsymbol{A} = \boldsymbol{A}(\boldsymbol{U}) = \partial \boldsymbol{F}/\partial \boldsymbol{U}$ is the Jacobian matrix of the flux vector $\boldsymbol{F}(\boldsymbol{U})$. The hyperbolic part of the Navier-Stokes equations Eq. (2.1) written as a quasi-linear system is

$$\frac{\partial}{\partial t}\begin{pmatrix} \rho \\ \rho \boldsymbol{u} \\ E \\ \rho Y_i \end{pmatrix} + \boldsymbol{A}\frac{\partial}{\partial x}\begin{pmatrix} \rho \\ \rho \boldsymbol{u} \\ E \\ \rho Y_i \end{pmatrix} = 0 \quad , \tag{2.22}$$

where $\boldsymbol{A}$ has $N-1$ real eigenvalues $\lambda_i(\boldsymbol{U})$ corresponding to $N-1$ eigenvectors $R_i(\boldsymbol{U})$. For a multi-component system with N species the Jacobian $\boldsymbol{A}$ is (Larouturou and Fezoui, 1989; Fedkiw et al., 1997)

$$\boldsymbol{A} = \begin{pmatrix} 0 & 1 & 0 & 0 & 0 & 0 & \cdots & 0 \\ -u^2+\frac{1}{2}(\overline{\gamma}-1)q^2+\mathcal{X} & (3-\overline{\gamma})u & (1-\overline{\gamma})v & (1-\overline{\gamma})w & \overline{\gamma}-1 & \mathcal{X}_1 & \cdots & \mathcal{X}_{N-1} \\ -uv & v & u & 0 & 0 & 0 & \cdots & 0 \\ -uw & w & 0 & u & 0 & 0 & \cdots & 0 \\ u[\frac{1}{2}(\overline{\gamma}-1)q^2-H]+u\mathcal{X} & H-(\overline{\gamma}-1)u^2 & (1-\overline{\gamma})uv & (1-\overline{\gamma})uw & \overline{\gamma}u & u\mathcal{X}_1 & \cdots & u\mathcal{X}_{N-1} \\ -uY_1 & Y_1 & 0 & 0 & 0 & u & \cdots & 0 \\ \vdots & \vdots & \vdots & \vdots & \vdots & & \ddots & \\ -uY_{N-1} & Y_{N-1} & 0 & 0 & 0 & 0 & \cdots & u \end{pmatrix} \quad , \tag{2.23}$$

where H is the enthalpy and $q = \|\boldsymbol{u}\|^2$ and $\mathcal{X}$ and $\mathcal{X}_i$ are given by

$$\mathcal{X} = \frac{\partial \overline{\gamma}}{\partial \rho}\rho e \tag{2.24}$$

$$\mathcal{X}_i = \frac{\partial \overline{\gamma}}{\partial \rho Y_i}\rho e \quad \text{for} \quad i \in [1, N-1] \quad . \tag{2.25}$$

The numerical solution of Eq. (2.22) requires a flux projection on local characteristics. For this purpose the corresponding Roe-averaged matrix $\widetilde{\boldsymbol{A}}$ needs to be calculated, along

with its right and left eigenvectors (Roe, 1981). The Roe-averaged matrix $\widetilde{\boldsymbol{A}}$ has to satisfy the following properties: (i) the hyperbolicity of the original system must be conserved, i.e., $\widetilde{\boldsymbol{A}}$ must have $N-1$ eigenvalues $\widetilde{\lambda}_i$ associated to $N-1$ independent eigenvectors $\widetilde{\boldsymbol{R}}_i$, (ii) $\widetilde{\boldsymbol{A}}$ has to be consistent with the original matrix, i.e., $\widetilde{\boldsymbol{A}}(\boldsymbol{U},\boldsymbol{U}) = \boldsymbol{A}(\boldsymbol{U})$ and (iii) $\widetilde{\boldsymbol{A}}$ has to be conservative across discontinuities, i.e., $\boldsymbol{F}(\boldsymbol{U_R}) - \boldsymbol{F}(\boldsymbol{U_L}) = \widetilde{\boldsymbol{A}}(\boldsymbol{U_R} - \boldsymbol{U_L})$.

The numerical fluxes at the cell boundaries $f_{i\pm1/2}$ are reconstructed from cell averages. After the flux reconstruction the fluxes $f_{i\pm1/2}$ are projected back onto the physical field. At sonic points a local switch to a Lax-Friedrichs flux is used as entropy fix, see, e.g., Toro (1999). It is important to note, that only $N-1$ species are projected onto the characteristic space as species N follows from the conservation of mass and the $N-1$ other species.

2.2.1. Flux reconstruction

The construction of high-order essentially non-oscillatory (ENO) shock-capturing schemes for hyperbolic conservation laws goes back to the work of Harten et al. (1987). The idea of choosing the most appropriate stencil from a set of candidate stencils yields high-order accuracy whenever the function to be approximated is smooth and avoids the Gibbs phenomenon at discontinuities. The ENO approach was later improved by Liu et al. (1994) who introduced the concept of weighted ENO (WENO) shock-capturing schemes, which uses a convex non-linear combination of a set of candidate stencils to reconstruct the fluxes. This approach, while preserving the essentially non-oscillatory property, improves the ENO methodology by an additional order of accuracy given the same stencil width. A comprehensive review on ENO as well as on WENO schemes and their efficient implementation is given in the lecture notes of Shu (1997).

Latini et al. (2007a) performed a systematic investigation of the effect of the WENO reconstruction order and the spatial resolution on the re-shocked two-dimensional RMI. While Latini et al. (2007a) investigated the general suitability of the WENO reconstruction methodology for RM unstable flows, they did not study the applicability of WENO schemes for viscous three-dimensional shock-driven turbulence. The classical WENO approach, albeit being formally high-order accurate, is very dissipative at discontinuities and in turbulent regions of the flow as the theoretical maximum order is never achieved in such regions.

In order to reduce the excessive dissipation of classical WENO schemes Hu et al. (2010) developed an adaptive central-upwind 6^{th}-order accurate WENO scheme (WENO-CU6). This scheme significantly reduces the numerical dissipation, while preserving the shock-capturing capabilities of classical WENO schemes and being only slightly computationally more complex than the standard 5^{th}-order WENO scheme. Additionally, Hu and Adams (2011) proposed a physically motivated scale-separation formulation of the original version which makes the WENO-CU6 scheme even less-dissipative and thus also applicable for under-resolved simulations.

The WENO-CU6 scheme reconstructs the flux at the cell boundary from a non-linear convex combination of a set of 3^{rd}-order candidate stencils

$$\hat{f}_{i+1/2} = \sum_{k=0}^{3} \omega_k \hat{f}_{k,i+1/2} \quad , \tag{2.26}$$

where ω_k is the weight assigned to the 3^{rd}-order stencil $\hat{f}_{k,i+1/2}$. The weights ω_k are constructed such that the method recovers a non-dissipative 6^{th}-order central stencil in smooth flow regions and preserves the non-oscillatory property at discontinuities

$$\omega_k = \frac{\alpha_k}{\sum_{k=0}^{3} \alpha_k} \quad , \quad \alpha_k = d_k \left(C + \frac{\tau_6}{\beta_k + \epsilon} \right)^q \quad , \tag{2.27}$$

where ϵ is a small positive number $\epsilon = 10^{-40}$ and d_k are the optimal weights, which give the 6^{th}-order central scheme, with $d_k = \{1/20,\ 9/20,\ 9/20,\ 1/20\}$. C and q are constant parameters, which are set to $C = 1000$ and $q = 4$, see Hu and Adams (2011). The reference smoothness indicator τ_6 is calculated from a linear combination of the other smoothness measures β_k with $\beta_3 = \beta_6$

$$\tau_6 = \beta_6 - \frac{1}{6}(\beta_0 + 4\beta_1 + \beta_2) \tag{2.28}$$

with

$$\beta_k = \sum_{j=1}^{2} \Delta x^{2j-1} \int_{x-1/2}^{x_{i+1/2}} \left(\frac{d^j}{dx^j} \hat{f}_k(x) \right)^2 dx \quad , \tag{2.29}$$

which gives

$$\beta_0 = \frac{1}{4} \left(f_{i-2} - 4f_{i-1} + 3f_i \right)^2 + \frac{13}{12} \left(f_{i-2} - 2f_{i-1} + f_i \right)^2 \quad , \tag{2.30}$$

$$\beta_1 = \frac{1}{4} \left(f_{i-1} - f_{i+1} \right)^2 + \frac{13}{12} \left(f_{i-1} - 2f_i + f_{i+1} \right)^2 \quad , \tag{2.31}$$

$$\beta_2 = \frac{1}{4} \left(3f_i - 4f_{i+1} + f_{i+2} \right)^2 + \frac{13}{12} \left(f_i - 2f_{i+1} + f_{i+2} \right)^2 \quad . \tag{2.32}$$

β_6 is also calculated from Eq. (2.29), but with the 5^{th}-degree polynomial approximation for the fluxes, which gives a 6-point stencil as smoothness indicator

$$\begin{aligned} \beta_6 = \frac{1}{10080} \big[& 271779 f_{i-2}^2 + 139633 f_{i+3}^2 \\ & + f_{i-2}(2380800 f_{i-1} + 4086352 f_i - 3462252 f_{i+1} + 1458762 f_{i+2} - 245620 f_{i+3}) \end{aligned} \tag{2.33}$$

$$
\begin{aligned}
&+f_{i-1}(5653317f_{i-1} - 20427884f_i + 17905032f_{i+1} - 7727988f_{i+2} + 1325006f_{i+3}) \\
&+f_i(19510972f_i - 35817664f_{i+1} + 15929912f_{i+2} - 2792660f_{i+3}) \\
&+f_{i+1}(17195652f_{i+1} - 15880404f_{i+2} + 2863984f_{i+3}) \\
&+f_{i+2}(3824847f_{i+2} - 1429976f_{i+3})] \quad .
\end{aligned}
$$

In a recent investigation Hu et al. (2014) introduced a dispersion-dissipation condition for finite-difference schemes. The condition is motivated by a wave-advection analogy which imposes a constraint on the dissipation and dispersion errors. The errors can be optimized independently in such a way that the overall performance of the scheme benefits from a balance between these errors by preventing backscatter of non-resolved scales into the resolved scale range. The dispersion-dissipation condition requires a modification of the optimal weights d_k of the WENO-CU6 scheme to guarantee a reasonable balance between dispersion and dissipation. The modified optimal weights are then $d_k = \{0.09045,\ 0.4441,\ 0.39227,\ 0.07318\}$. This modification significantly improves the implicit subgrid-scale modeling capabilities and the modified WENO-CU6 scheme can compete with other state-of-the-art subgrid scale models, like ALDM (Hickel et al., 2006; Hickel and Larsson, 2008) while preserving its shock-capturing properties.

For the scope of this work the WENO-CU6 scheme (Hu et al., 2009, 2010) is used for all under-resolved simulations (Tritschler et al., 2013a,b, 2014a,b), whereas the dispersion-dissipation optimized version Hu et al. (2014) is only used for the DNS (Tritschler et al., 2014c).

2.2.2. Time integration

The method of lines approximation of the Navier-Stokes equations yields a system of ordinary differential equations

$$\frac{d\phi}{dt} = \phi_t = \mathcal{L}(\phi) \quad , \tag{2.34}$$

with $\phi_0 = \phi(t = 0)$ and where $\mathcal{L}$ is a finite difference operator. For the purpose of time integration the 3^{rd}-order total variation diminishing Runge-Kutta scheme of Gottlieb and Shu (1998) is used in this thesis. The 3^{rd}-order scheme consists of three substeps to compute the new solution at the next time step $\phi^{(n+1)}$

$$\phi^{(1)} = \phi^{(n)} + \Delta t\mathcal{L}(\phi^{(n)}) \tag{2.35}$$

$$\phi^{(2)} = \frac{3}{4}\phi^{(n)} + \frac{1}{4}\phi^{(1)} + \frac{1}{4}\Delta t\mathcal{L}(\phi^{(1)}) \tag{2.36}$$

$$\phi^{(n+1)} = \frac{1}{3}\phi^{(n)} + \frac{2}{3}\phi^{(2)} + \frac{2}{3}\Delta t\mathcal{L}(\phi^{(2)}) \quad . \tag{2.37}$$

3. Accomplishments

In this chapter the contribution of each publication is summarized, including a short overview of the current state-of-the-art in research with special emphasis on the objectives of this thesis.

3.1. Numerical model uncertainties of the Richtmyer-Meshkov instability

Recent research has focused on the effect of different initial condition parameters on the evolution of RMI. Lombardini et al. (2011) have studied the effect of the Atwood number on the turbulent mixing. In a later work the effect of the shock Mach number on the mixing process was examined by the same authors (Lombardini et al., 2012). Other studies (Thornber et al., 2010; Grinstein et al., 2011; Schilling and Latini, 2010) for instance have evaluated the contribution of the specific initial interface perturbations on the mixing dynamics.

The general assumption of all these investigations is that the marginally and non-resolved scales have a negligible effect on the resolved scales, and therefore on the evolution of the instability. This assumption is based on standard arguments such as empirical resolution criteria and on a validation of the SGS models for simple flows. A shock induced mixing zone, however, has anisotropic and inhomogeneous decaying turbulence, such that it is not clear if these SGS models, validated for more simple flows, are directly applicable to RMI. Due to the numerical difficulties to capture discontinuities such as shock waves and

interfaces, model comparison to a reference solution with resolved SGS terms does not exist for RMI. Also, the effect of subgrid-scale regularizations and dispersive or dissipative truncation errors on the resolved scales and turbulent mixing measures have not been studied yet systematically.

In the numerical investigation of Thornber et al. (2011) the authors reported a Kolmogorov scaling $k^{-5/3}$ at early times that develops towards a $k^{-3/2}$ range for lower wavenumbers and a Kolmogorov scaling for high wavenumbers at late times. In contrast to this Hill et al. (2006) and Lombardini et al. (2012) identified a persistent $k^{-5/3}$ scaling and Cohen et al. (2002) and Grinstein et al. (2011) again found neither a $k^{-5/3}$ nor a $k^{-3/2}$ spectrum range. These discrepancies stress that a systematic investigation of numerical modeling uncertainties is needed and additionally that a deterministic and reproducible reference data set is desirable in order to improve the existing numerical models for the specific demands of RMI.

The following analysis serves as guidance in interpreting simulation results which are marginally or intentionally under-resolved. Given the state of research much can be learned with respect to physical interpretation of numerical results by comparing numerical models with entirely different subgrid-scale regularization strategies. The quantification of the dependence of fluctuating and small scale quantities on the numerical method and grid spacing is of great value for the validation of SGS models and for the development of lower fidelity closure models.

In the numerical study of Latini et al. (2007a), for instance, the authors emphasize that lower-order schemes and lower-resolution simulations have higher numerical dissipation and therefore preserve large-scale structures and flow symmetry for a non-physically long time. In contrast to this exhibit higher-order schemes and higher-resolution simulations increased mixing due to symmetry breaking events triggered by the truncation error of the underlying scheme. Latini et al. (2007a) compared their results to the experimental investigation of Collins and Jacobs (2002) which served as reference to evaluate the performance of the different *WENO* schemes, ranging form the 3^{rd}-order accurate *WENO-3* to the 9^{th}-order accurate *WENO-9*.

Besides subgrid-scale regularization and truncation error also the numerical model that accounts for multiple species in the flow may affect the flow evolution. Various multi-component models have been proposed during the past years. However, most of them lead to severe pressure oscillations (Karni, 1994, 1996; Abgrall, 1996; Abgrall and Smadar, 2001) at the material interface or introduce excessive dissipation, of which both are undesired properties. Particularly, because of the pressure oscillations single-component models have been widely used (Latini et al., 2007a,b; Schilling et al., 2007). Single-component models, however, give a mismatch in the post-shock quantities, which in consequence results in a wrong temporal prediction of the instability evolution.

V. K. Tritschler, X. Y. Hu, S. Hickel and N. A. Adams (2013)
Numerical simulation of a Richtmyer-Meshkov instability with an adaptive central-upwind 6th-order *WENO* scheme
Phys. Scr., **T155**, 014016

In this paper (Tritschler et al., 2013b) the adaptive central-upwind 6^{th}-order weighted essentially non-oscillatory (WENO) scheme of Hu et al. (2010) is used to study the single-mode RMI. For this purpose a general Roe average for ideal gas mixtures is proposed that suppresses spurious pressure oscillations at the material interface even when captured with a high-order scheme. The proposed Roe average is an extension for generalized equation of states while being simple and satisfying the U-property exactly in contrast to the works of Liou et al. (1990) and Shyue (2001). Moreover, the Roe average does not introduce artificial states as done by Glaister (1988) and predicts the averages directly from the adjacent states. The linear approximation between the average state and the adjacent states for a single phase interaction, as assumed by Hu et al. (2009), does not hold in the present study and had to be adapted accordingly. The proposed generalized Roe average together with the WENO-CU6 reconstruction scheme is tested and validated by two one-dimensional test cases, which show that spurious pressure oscillations at material interfaces are successfully suppressed without introducing undesirable amounts of numerical dissipation.

To study the single-mode RMI the WENO-CU6 and the standard WENO-5 method are used as reconstruction schemes and the results are compared to the experimental investigation of Jacobs and Krivets (2005). The more dissipative WENO-5 method preserves large-scale structures and symmetries for a non-physical long time while the WENO-CU6 better resolves small-scale structures, leading to earlier symmetry breaking and increased mixing, see also Latini et al. (2007a). The study also reveals that the global characteristics was neither matched by the WENO-CU6 nor by the WENO-5 method when a single-component model is used. This is due to the fact that a single-component model leads to a mismatching post-shock state and thus leads to a wrong prediction of the late-time evolution. The proposed multi-component model significantly improves the overall agreement between simulation and experiment.

The main contribution of this work is threefold: (i) a generalized Roe average is proposed which suppresses spurious pressure oscillations at material interfaces, (ii) it is shown that the recently developed WENO-CU6 scheme of Hu et al. (2010) together with the generalized Roe average introduces only very small numerical dissipation while preserving its good shock-capturing properties and therefore is very well suited for the investigation of shock-initiated mixing problems and (iii) the two-dimensional simulations of the single-mode RMI show that a considerable improvement of the results is obtained with the modified multi-component model of the present investigation and that the specific numerical model can have a significant effect on the late-time evolution of the instability.

My contribution to this work was the development of the concept of the study including its main objectives. I tested and validated the implementations of the proposed model in the in-house code INCA, performed the numerical simulations and wrote major parts of the manuscript for the publication.

V. K. Tritschler, B. J. Olson, S. K. Lele, S. Hickel, X. Y. Hu and N. A. Adams (2014)
On the Richtmyer-Meshkov instability evolving from a deterministic multi-mode planar interface
J. Fluid Mech., **755**, 429-462

In this paper (Tritschler et al., 2014b) the shock-induced turbulent mixing between a light and heavy gas initiated by a $Ma = 1.5$ shock wave is investigated by two independently developed numerical models. The initial interface perturbations between the gases is imposed spectrally exact by a deterministic function which allows a direct quantitative comparison between the two models. From this setup well-resolved large eddy simulation results are obtained for both numerical models with the objective of assessing turbulence structures in multi-component material mixing and prediction uncertainties due to differences in the subgrid-scale regularizations.

The focus of this study is the physical effect of numerical errors on the marginally resolved to non-resolved scale range. So far investigations in literature have assumed that the marginally and non-resolved scales have a negligible effect on the resolved scales, and therefore on the evolution of the instability. Uncertainties introduced by the numerical method, i.e., the subgrid-scale regularization and truncation errors, have not been investigated systematically, despite the fact that they actually can have physically meaningful interpretations. The present contribution clearly demonstrates that fine scales are captured differently between numerical methods. Spectral analysis shows that the subgrid-scale regularizations significantly change the small-scales close to the cut-off wavelength, which is dominantly dissipative for one model and dominantly dispersive for the other.

Whereas the small scales close to the cut-off wavelength are affected by the subgrid-scale regularization, the large scales of motion are in excellent agreement between the methods. The results conclusively show that before re-shock the main differences exist in the representation of the material interface. Due to shear and strain the interface steepens and eventually becomes under-resolved and the interface thickness becomes dependent on the resolution limit of the numerical scheme. Thus, the main numerical challenge prior to re-shock is to predict the large-scale non-linear entrainment and the associated interface sharpening when the instabilities are still regular.

The main contributions of this paper are: (i) spectral and temporal scalings that have been controversially discussed in literature are confirmed by demonstrating that they are recovered by different numerical methods, (ii) a systematic framework for spectral and scaling analysis for turbulence structures in the mixing zone is provided, (iii) the physical effects of SGS regularization on the resolved and non-resolved scale ranges is analyzed, (iv) a generic set of high-confidence initial data is presented with the purpose for establishing a benchmark data set for model improvement.

My contribution to this work was the development of the concept of the study including its main objectives for the collaboration with Stanford University. I tested and validated the implementations in the in-house code INCA, performed the numerical simulations and wrote major parts of the manuscript for the publication.

3.2. Parameter uncertainties of the Richtmyer-Meshkov instability

Jones and Jacobs (1997) established a new membrane-free technique which allows to create very accurately prescribed initial conditions in experimental investigations. This technique was employed by Tomkins et al. (2008) to study the shock-initiated material mixing between a heavy-gas cylinder and the surrounding air. Tomkins et al. (2008) did not only present very clear contour maps of the heavy-gas concentration to record the temporal evolution of the instability, but also provided, for the first time, the instantaneous scalar dissipation rate.

In the numerical investigation of Shankar et al. (2011) the authors presented, for the first time, fully-resolved two-dimensional simulation results with four species N_2, O_2, SF_6 and C_3H_6O (acetone) of the experiment of Tomkins et al. (2008). The temporal evolution of the instability, as predicted by the numerical simulation, however, differed characteristically from the experimental result. The authors hypothesized that deviations of the initial conditions from the nominal values may have a non-negligible effect on the instability evolution.

In order to perform a comprehensive and quantitative comparison between experimental measurements and numerical simulations the uncertainties on both sides need to be characterized. In the previous section the focus was on the uncertainties introduced by the numerical model. Here, the focus is on parameter uncertainties in the experiment such as the inflow conditions, the gas-cylinder composition and the gas-cylinder shape. These uncertainties, among others, lead to a characteristic difference in the prediction of the temporal evolution of the instability between experiment and simulation. This observation was the driving motivation for a rigorous quantification of initial-data uncertainties with the objective of assessing the effect of these uncertainties onto the output quantities of interest (QoI). A general framework is developed to quantify the initial-data uncertainties in shock-accelerated mixing problems by coupling a high-order numerical simulation model with a polynomial chaos expansion in order to propagate the initial-data uncertainties onto the output QoI.

V. K. Tritschler, A. Avdonin, S. Hickel, X. Y. Hu and N. A. Adams (2014)
Quantification of initial-data uncertainty on a shock-accelerated gas cylinder
Phys. Fluids, **26**, 026101

In this paper (Tritschler et al., 2014a) the observed discrepancies between grid-resolved numerical simulations of the shock-cylinder interaction and experiments are, for the first time, systematically addressed.

The initial-data uncertainties of a shock accelerated heavy-gas cylinder are investigated by two-dimensional fully-resolved simulations. The initial data are chosen such that the experimental investigation of Tomkins et al. (2008) is matched. The shock Mach number, the contamination of the heavy-gas region with acetone and the initial deviations of the heavy-gas region from a perfect cylindrical shape are identified as the main sources of uncertainty and as those with the main effect on the temporal evolution of the instability. To propagate the initial-data uncertainties of these three parameters onto the output QoI a polynomial chaos expansion is used. The polynomial chaos expansion is a general framework for the approximate representation of random response functions in terms of finite-dimensional series expansions in standardized random variables.

Mixing quantities like the total mixing rate (TMR) and the molecular mixing fraction (MMF) appear to be more sensitive with respect to uncertainties in the initial data compared to geometrical quantities like the position of the heavy-gas region and its cross section. The investigation suggests that TMR and MMF are highly sensitive to changes in the Mach number and acetone concentration. Due to the high sensitivity level of TMR it is the ideal objective function to find the exact initial conditions of the experiment. The TMR data presented by Tomkins et al. (2008), however, were given in arbitrary units which makes quantitative comparison to these data impossible. Thus, an alternative objective function is used in the present investigation which is the ratio of the downstream and upstream roll-up spiral width of the instability.

Within the investigated uncertainty domain a set of initial data is determined by solving an optimization problem with the downstream and upstream roll-up spiral width as the objective function. The numerical results for this parameter set are in excellent agreement with the experiment and suggest that the measured Mach number and the estimated contamination of the heavy-gas region with acetone are strongly biased. Thus, for an accurate numerical reproduction of the experiment it is crucial that the initial shock Mach number and the exact initial composition of the heavy-gas region are known.

The main contributions of this paper are: (i) the effect of initial-data uncertainties of the shock Mach number, the contamination of the heavy-gas cylinder with acetone and the initial deviation of the heavy-gas region from a perfect cylindrical shape on mixing processes is investigated, (ii) the relative importance of these parameters on the mixing dynamics is quantified, and (iii) the sources of the observed discrepancies between numerical simulations and experiments are identified and finally (iv) a general framework to quantify the initial-data uncertainties of shock-material interface interactions is provided.

My contribution to this work was the development of the concept of the study including its main objectives. I tested and validated the implementations in the in-house code INCA and wrote major parts of the manuscript for the publication.

3.3. Direct numerical simulations

The standard numerical approach to RMI are under-resolved direct numerical simulations or large eddy simulations (Lombardini et al., 2012; Bai et al., 2012; Grinstein et al., 2011; Thornber et al., 2011; Schilling and Latini, 2010). In many of these simulations it has been assumed that, due to the high Reynolds numbers, viscous effects can be neglected (Grinstein et al., 2011; Thornber et al., 2011; Schilling and Latini, 2010). However, recent investigations have demonstrated, that viscous effects as well as the employed subgrid-scale regularization (Tritschler et al., 2014b) play an important role for the evolution of the instability. Thus, it is very desirable to have fully-resolved data from direct numerical simulations (DNS) for model development, as reference benchmark data and to investigate the physics of the complex interaction of shock waves with perturbed three-dimensional interfaces.

Previous investigations have provided estimates for the Kolmogorov length scale in three-dimensional RMI. Weber et al. (2012) found the Kolmogorov length scale in a shock accelerated shear layer by fitting model spectra to their experimental kinetic energy spectra. Their estimate is in the range of $125\mu m \leq \eta \leq 214\mu m$ for a shock Mach number of $Ma = 1.5$. In a later study Weber et al. (2014) investigated the turbulent mixing transition of RMI and found $\mathcal{O}(100)\mu m$ for $Ma = 1.6$ and $Ma = 2.2$. Also, in the numerical investigations of Lombardini et al. (2012) and Tritschler et al. (2013a) it was shown that the Kolmogorov length scale for moderate strong shock waves is in the range $70\mu m \lesssim \eta \lesssim 330\mu m$, however, some time after the shock-interface interaction. Shortly after the interaction the Kolmogorov length scale is expected to be considerably smaller, i.e., $\eta \sim \mathcal{O}(1)\mu m$.

Given these estimates fully-resolved numerical results of experimental-sized setups with dimensions of $\mathcal{O}(10^{-1})m$ are beyond today's computational resources. A scaling of the shock tube, however, results in a proportional scaling of the integral scales and thus reduces the total amount of scales that need to be resolved. DNS in scaled shock tubes are feasible and allow to investigate the fundamentals of material mixing on the smallest scales.

V. K. Tritschler, M. Zubel, S. Hickel and N. A. Adams (2014)
Evolution of length scales and statistics of Richtmyer-Meshkov instability from direct numerical simulations
Phys. Rev. E, **90**, 063001

In this paper (Tritschler et al., 2014c) direct numerical simulation results of the Richtmyer-Meshkov instability evolving from a three-dimensional corrugated planar interface are presented. A set of three simulations is performed at three different shock Mach numbers $Ma = 1.05$, $Ma = 1.2$ and $Ma = 1.5$. For the purpose of obtaining fully-resolved results the shock tube is scaled down to a width of $1cm$. This reduces the effective Reynolds number and allows to resolve all relevant flow scales. Grid-convergence is demonstrated through a systematic convergence study of the Kolmogorov length scale and of the spectra of enstrophy. For the two lower shock Mach numbers the enstrophy spectra are fully resolved at the highest resolution $\Delta_{xyz} \approx 19.5\mu m$ and at all times. At the highest shock Mach number the peak enstrophy is resolved on the finest grid for $t \gtrsim 100\mu m$.

At the lowest shock Mach number the flow is below a critical Reynolds number and mixing between the fluids is dominated by viscous diffusion. However, when the critical Taylor-microscale Reynolds number $Re_\lambda \gtrsim 35 - 80$ is exceeded the flow transitions to turbulence accompanied by the emergence of a narrow but distinct Kolmogorov inertial subrange. For $Re_\lambda \gtrsim 35 - 80$ the Liepmann-Taylor scale exceeds the upper limit of the dissipative range, consistent with the existence of a Kolmogorov inertial subrange. The observed critical Taylor-microscale Reynolds number in the present investigation is smaller than the estimated minimum Taylor-microscale Reynolds number of $Re_\lambda \approx 100 - 140$ for mixing transition as proposed by Dimotakis (2000). Also, at this Reynolds number a clear separation of the scales of turbulent motion, i.e., Kolmogorov length scale, Taylor microscale and integral length scale is observed.

The paper clearly demonstrates that the decay rates of turbulence kinetic energy and viscous dissipation are in good agreement with values from isotropic turbulence. The presented probability density functions of velocity and the longitudinal and transverse derivatives collapse self-similarly, when scaled with their standard deviation. Also, the statistical moments, kurtosis and skewness, are in very good agreement with values known from isotropic turbulence. All this suggests that turbulence evolving from RMI at sufficiently high Reynolds numbers behaves similarly to generic decaying isotropic turbulence, while being non-homogeneous and anisotropic in the shock propagating direction.

The main contributions of this paper are: (i) for the first time direct numerical simulation results of RMI are presented, (ii) these results show that a clear separation of scales emerges as the Reynolds number exceeds a critical value and only then a Kolmogorov inertial subrange is observed, while the fluids mix mainly due to viscous diffusion below the critical Reynolds number and (iii) the DNS data provide first evidence that turbulence evolving from a shock-accelerated planar interface is not fundamentally different from decaying homogeneous isotropic turbulence.

My contribution to this work was the development of the concept of the study including its main objectives. I tested and validated the implementations in the in-house code INCA and wrote major parts of the manuscript for the publication.

4. Conclusion

The Richtmyer-Meshkov instability (RMI) plays an important role in many natural as well as in technical material mixing phenomena and applications. RMI arises on almost all scales ranging from the smallest in inertial confinement fusion (Lindl et al., 1992; Taccetti et al., 2005; Aglitskiy et al., 2010) to the largest in the formation of supernova remnants (Arnett, 2000; Almgren et al., 2006; Kane et al., 1999).

A particular focus of the present thesis was the quantification of numerical model uncertainties of RMI simulations. The subgrid-scale regularizations which are used for this purpose have been only validated against simple generic test cases such as the Taylor-Green vortex. Material mixing evolving from RMI, however, is a significantly more complex anisotropic and inhomogeneous phenomenon, where mixing mainly occurs close to the cut-off wavelength. Consequently, the employed numerical model can have an important effect on the evolution of such flows.

The present thesis provided a complete framework for the quantification of numerical model uncertainties in material mixing problems. The effect of the numerical model on the flow evolution was assessed by a detailed analysis of the effect of subgrid-scale regularization, truncation error and multi-component model. This will provide guidance in interpreting future numerical data as it allows to clearly separate between real physics and numerical errors with physical interpretation. Also, a high-confidence data set was provided by reproducing the instability evolution and the key physics with two independently developed numerical models. Thereby, spectral and temporal scalings that have been controversially discussed in the literature were confirmed. Furthermore, the presented analysis of turbulence structures in material mixing zones contributes to a better

understanding of shock-initiated material mixing phenomena on the small scales.

Initial-data uncertainties and their effect on output quantities of interest were quantified by coupling a polynomial chaos expansion with a high-order numerical simulation model. The polynomial chaos expansion was used to propagate the initial-data uncertainties onto the output quantities of interest. This framework was applied to the shock-cylinder interaction investigation of Tomkins et al. (2008). The investigation allows to better understand the connection between initial-data variations and the observed output quantities in experimental investigations. This analysis also helps to identify the role of parameter uncertainties in experimental investigations and how these uncertainties contribute to the observed discrepancy between numerical and experimental investigations.

Additionally, direct numerical simulation results of RMI initiated by a shock wave interacting with a perturbed planar interface were presented. These results showed that at the lowest investigated shock Mach number the heavy and light fluid mix mainly due to viscous diffusion, whereas at the highest shock Mach number, when a critical Reynolds number is exceeded, the mixing zone becomes fully turbulent with a Kolmogorov inertial subrange. The results conclusively showed a clear separation of flow scales (Kolmogorov length scale, Taylor microscale and integral length scale) at Reynolds numbers above the critical value. Furthermore, turbulence statistics available for the first time such as probability density functions of the velocity and its longitudinal and transverse derivatives indicate that turbulence evolving from RMI is not fundamentally different from decaying isotropic turbulence, while being virtually only homogeneous and isotropic in two dimensions.

The proposed systematic framework for parameter and numerical model uncertainty quantification together with high-confidence data provides a unique toolbox for the interpretation of existing and future results. Only now, a complete and unifying picture of shock-initiated material mixing phenomena is within reach.

A. Full list of peer-reviewed journal publications

- **V. K. Tritschler**, S. Hickel, X. Y. Hu and N. A. Adams (2013). On the Kolmogorov inertial subrange developing from Richtmyer-Meshkov instability. *Phys. Fluids*, 25, 071701

- **V. K. Tritschler**, X. Y. Hu, S. Hickel and N. A. Adams (2013). Numerical simulation of a Richtmyer-Meshkov instability with an adaptive central-upwind 6th-order WENO scheme. *Phys. Scr.*, T155, 014016

- **V. K. Tritschler**, A. Avdonin, S. Hickel, X. Y. Hu and N. A. Adams (2014). Quantification of initial-data uncertainty on a shock-accelerated gas cylinder. *Phys. Fluids*, 26, 026101

- **V. K. Tritschler**, B. J. Olson, S. K. Lele, S. Hickel, X. Y. Hu and N. A. Adams (2014). On the Richtmyer-Meshkov instability evolving from a deterministic multimode planar interface. *J. Fluid Mech.*, 755, 429-462

- **V. K. Tritschler**, M. Zubel, S. Hickel and N. A. Adams (2014). Evolution of length scales and statistics of Richtmyer-Meshkov instability from direct numerical simulations. *Phys. Rev. E*, 90, 063001

- X. Y. Hu, **V. K. Tritschler**, S. Pirozzoli and N. A. Adams (2015). Dispersion-dissipation condition for finite difference schemes. *J. Comput. Phys.*, under review

- F. R. Diegelmann, **V. K. Tritschler**, S. Hickel and N. A. Adams (2015). On the pressure dependence of ignition and mixing in reactive shock-bubble interaction. *Combust. Flame*, under review

B. Selected peer-reviewed journal publications

Here, the four main peer-reviewed journal publications are attached.

Phys. Scr. **T155** (2013) 014016 (8pp) doi:10.1088/0031-8949/2013/T155/014016

Numerical simulation of a Richtmyer–Meshkov instability with an adaptive central-upwind sixth-order WENO scheme

V K Tritschler, X Y Hu, S Hickel and N A Adams

Institute of Aerodynamics and Fluid Mechanics, Technische Universität München, 85748 München, Germany

E-mail: volker.tritschler@aer.mw.tum.de

Received 21 February 2012
Accepted for publication 12 May 2012
Published 16 July 2013
Online at stacks.iop.org/PhysScr/T155/014016

Abstract
Two-dimensional simulations of the single-mode Richtmyer–Meshkov instability (RMI) are conducted and compared to experimental results of Jacobs and Krivets (2005 *Phys. Fluids* **17** 034105). The employed adaptive central-upwind sixth-order weighted essentially non-oscillatory (WENO) scheme (Hu *et al* 2010 *J. Comput. Phys.* **229** 8952–65) introduces only very small numerical dissipation while preserving the good shock-capturing properties of other standard WENO schemes. Hence, it is well suited for simulations with both small-scale features and strong gradients. A generalized Roe average is proposed to make the multicomponent model of Shyue (1998 *J. Comput. Phys.* **142** 208–42) suitable for high-order accurate reconstruction schemes. A first sequence of single-fluid simulations is conducted and compared to the experiment. We find that the WENO-CU6 method better resolves small-scale structures, leading to earlier symmetry breaking and increased mixing. The first simulation, however, fails to correctly predict the global characteristic structures of the RMI. This is due to a mismatch of the post-shock parameters in single-fluid simulations when the pre-shock states are matched with the experiment. When the post-shock parameters are matched, much better agreement with the experimental data is achieved. In a sequence of multifluid simulations, the uncertainty in the density gradient associated with transition between the fluids is assessed. Thereby the multifluid simulations show a considerable improvement over the single-fluid simulations.

PACS numbers: 47.20.Lz, 47.20.Ma, 47.20.Cq, 47.51.+a

(Some figures may appear in colour only in the online journal)

1. Introduction

1.1. Richtmyer–Meshkov instability (RMI)

The RMI occurs when the perturbed interface of two fluids with different densities is accelerated impulsively, e.g. by a shock wave [4, 5]. Therefore it is considered as the impulsive limit of the Rayleigh–Taylor instability [6]. The misalignment of the pressure gradient ∇p (associated with the shock wave) and the density gradient $\nabla \rho$ between the two fluids causes baroclinic generation of vorticity on the interface. Baroclinic vorticity deposition is the initial driving force for the development of the primary instabilities. Following the shock passage the disturbances initially present on the interface will grow linearly in time. Nonlinear growth follows when the amplitude of the perturbation becomes important compared to its characteristic wavelength. The nonlinear growth of RMI is characterized by the development of asymmetric 'bubbles' and 'spikes'. Eventually, Kelvin–Helmholtz instability gives rise to the development of small scales. If the initial

energy input is sufficient, a turbulent mixing zone establishes between the fluids where the large-scale structures are progressively broken down into smaller scales. The broadband spectrum of motions present in RMI is one of the main reasons why numerical treatment is challenging. A fundamental understanding of the amplification of initial interface perturbations along with the associated mixing process is of crucial importance for both man-made and natural phenomena. According to Arnett [7], RMI is the reason for the lack of stratification of the supernova 1987a and needs to be taken into account in stellar evolution models. An engineering application of RMI is the strong enhancement of mixing processes, such as the mixing of fuel with an oxidizer in supersonic propulsion engines [8]. A comprehensive description of RMI is given by Brouillette [9] and Zabusky [10] in their reviews.

In recent decades, RMI has been widely studied analytically, numerically and experimentally. In the numerical investigation by Latini *et al* [11, 12], the authors emphasized the importance of high-order reconstruction methods for the simulation of RMI. They found that lower-order methods preserve large-scale structures and symmetry to late times, while higher-order methods could time efficiently resolve small-scale structures, leading to symmetry breaking and increased mixing. This finding that higher-order methods are more time efficient in resolving the broad range of wavelengths present in RMI was one of the motivations to apply the sixth-order adaptive central-upwind weighted essentially non-oscillatory scheme (WENO-CU6) of Hu *et al* [2] to RMI in the present study. Latini *et al* used the experimental study of Collins and Jacobs [13] as the reference. Collins and Jacobs made use of a new technique that allows the development of a defined gas–gas interface without the use of a membrane. This membrane-free technique was first employed by Jones and Jacobs [14]. In the shock-tube experiment of Collins and Jacobs a moderate shock wave interacts with a sinusoidally perturbed material interface of air–acetone. When the shock wave impacts on the interface, baroclinic vorticity production on the interface gives rise to a single-mode RMI. After the first impact the shock wave travels downstream before it is reflected at the end wall of the tube and hits the interface a second time. Later, Jacobs and Krivets [1] used the same experimental setup to redo the experiment at higher Mach numbers. As higher Mach numbers led to faster growth, they were able to obtain valuable information on the late-time development of the single-mode instability, leading to a turbulent mixing zone between the fluids. This experiment is used as the reference in our numerical study.

1.2. Numerical schemes for accelerated compressible multicomponent flows

The broad range of scales present in RMI makes numerical simulations difficult. The numerical discretization method needs to capture steep gradients such as shocks and contact surfaces and should be non-dissipative in smooth flow regions. The RMI is also a multicomponent flow and therefore needs a numerical treatment that is somewhat more complex than for single-component flows. The fluid dynamic properties of multicomponent flows are conventionally modeled by solving additional transport equations for 'information quantities' that account for the presence of different species in the flow. Attempts to attribute conservative properties to these 'information quantities' often suffered from strong unphysical oscillations across the material interface. The occurrence of these numerical inaccuracies led to several publications [15–19] employing non-conservative or quasi-conservative models. In the literature there are also other proposals to maintain pressure equilibrium across material interfaces in a conservative form [20, 21]. Except for Marquina and Pulet's [20] conservative flux-splitting algorithm (they use a conventional WENO-5 reconstruction) all published simulations used low-order reconstruction schemes and effectively fail when combined with a low-dissipation scheme such as WENO-CU6. Some of the proposed models could not properly suppress oscillations when a high-order scheme was applied and some introduced excessive dissipation around the material interface. However, we found the quasi-conservative volume fraction-based model of Abgrall [16], which was later extended from polytropic gases to stiffened gases by Shyue [3], most suitable for use in combination with WENO-CU6. Allaire *et al* [19] generalized the four-equation model of Shyue to a five-equation model that allows the simulation with general equations of state, including tabulated laws. The WENO-CU6 scheme [2] is an attempt to overcome the dissipative nature of other upwind biased WENO schemes; for a review see [22]. WENO-CU6 is based on a new smoothness measure that adapts the numerical stencil between a nonlinear convex combination of lower third-order upwind stencils in regions with steep gradients and a sixth-order central stencil in smooth flow regions. The WENO-CU6 method exhibits enough dissipation close to discontinuities to preserve stability, but allows the stencil to transform to a sixth-order central stencil in smooth flow regions. WENO-CU6 is therefore much less dissipative than other WENO methods. This makes the WENO-CU6 method better suited for direct numerical simulation of RMI with its characteristic broad wavenumber spectrum.

1.3. Scope of the present study

The Euler equations are solved on a two-dimensional (2D) grid. In the computational domain a shock wave first travels through air and then impacts a sinusoidally perturbed interface to SF_6. A single-fluid and a multifluid simulation are conducted and compared to the experiments of Jacobs and Krivets [1]. The aim of this paper is (i) to assess the performance of the WENO-CU6 method for accelerated compressible flows, (ii) to show the importance of using a multicomponent model for the RMI simulation instead of a single-component model, and (iii) to modify the multifluid model such that it ensures pressure equilibrium across the material interface also for high-order methods.

Section 2 presents the governing equations of the problem. Viscous terms are neglected. In section 3, the WENO-CU6 method used for space discretization is outlined together with modifications done to the generalized Roe average of Hu *et al* [23]. These modifications were necessary in order to make the multicomponent model suitable for

the sixth-order method. The initial conditions are discussed in section 5 along with a description of the computational domain in section 5.1 and the non-dimensionalization in section 5.2. The results of both single-component and multicomponent simulations are presented and compared to experiments in section 6, pointing out the importance of a multicomponent model and the use of a low dissipative discretization method for flows where molecular transport plays a weak role. The key findings of this study are then discussed and summarized in section 7.

2. Governing equations

The compressible Euler equations for an ideal binary gas mixture can be written as

$$\frac{\partial \rho}{\partial t} + \nabla \cdot (\rho \boldsymbol{u}) = 0, \tag{2.1}$$

$$\frac{\partial (\rho \boldsymbol{u})}{\partial t} + \nabla \cdot (\rho \boldsymbol{u}\boldsymbol{u} + p\underline{\boldsymbol{\delta}}) = 0, \tag{2.2}$$

$$\frac{\partial E}{\partial t} + \nabla \cdot [(E + p)\boldsymbol{u}] = 0, \tag{2.3}$$

$$\frac{\partial z_{\mathrm{SF_6}}}{\partial t} + \nabla \cdot (\boldsymbol{u} z_{\mathrm{SF_6}}) = z_{\mathrm{SF_6}} \nabla \cdot \boldsymbol{u}, \tag{2.4}$$

where ρ is the mixture density, $\boldsymbol{u}$ is the velocity, p is the pressure, E is the total energy, $z_{\mathrm{SF_6}}$ is the volume fraction of SF_6 gas and $\underline{\boldsymbol{\delta}}$ is the unit tensor. The volume fraction of air is easily obtained by $z_{\mathrm{air}} = 1 - z_{\mathrm{SF_6}}$. The equation of state (EOS) for an ideal gas mixture is used

$$p(\rho e, z) = (\overline{\gamma}(z) - 1)\rho e, \tag{2.5}$$

where $\overline{\gamma}$ is the ratio of specific heats of the gas mixture with [3]

$$\frac{1}{\overline{\gamma} - 1} = \sum_i \frac{z_i}{\gamma_i - 1}. \tag{2.6}$$

The internal energy of the system is denoted as e and is defined as

$$e = \frac{E}{\rho} - \frac{1}{2}\boldsymbol{u}^2. \tag{2.7}$$

3. Numerical scheme

In the 1D case, system (2.1)–(2.3) can be written in the conservative form as

$$\boldsymbol{U}_t + \boldsymbol{F}(\boldsymbol{U})_x = 0 \tag{3.1}$$

with $\boldsymbol{U} = (\rho, \rho u, E)^{\mathrm{T}}$ and $\boldsymbol{F}(\boldsymbol{U}) = (\rho u, p + \rho u^2, u(E + p))^{\mathrm{T}}$.

We solve (3.1) in characteristic form. The eigensystem of fluxes in (3.1) is obtained from the Roe-averaged Jacobian, which yields the left and right eigenvectors. The left eigenvectors project the fluxes onto the characteristic field, and the eigenvalues of the Jacobian are used to ensure upwinding.

To obtain high-order accurate numerical fluxes at the cell boundaries $\hat{f}_{i\pm1/2}$, the WENO-CU6 method is employed to reconstruct these values from cell averages. Finally, the reconstructed numerical fluxes at the cell face are projected back onto the physical field using the right eigenvectors. An entropy fix is implemented by the Lax–Friedrichs flux splitting. For more details of Riemann solvers, see [24]. The left-hand side of (3.1) is evolved in time using a third-order total variation diminishing Runge–Kutta scheme.

3.1. The adaptive central-upwind sixth-order WENO scheme

The motivation for Hu *et al* [2] to develop the WENO-CU6 discretization scheme was that standard WENO schemes exhibit excessive dissipation and accordingly overwhelm large amounts of the small-scale structure in a flow. The principle of the WENO-CU6 method is to use a non-dissipative sixth-order central method in smooth flow regions and a nonlinear convex combination of third-order approximation polynomials in regions with steep gradients. This new weighting strategy preserves the good shock capturing properties of other WENO methods, while it can achieve very low numerical dissipation in smooth flow regions.

The reconstructed numerical fluxes at the cell boundaries are computed from

$$\hat{f}_{i+1/2} = \sum_{k=0}^{3} \omega_k \hat{f}_{k,i+1/2}, \tag{3.2}$$

where ω_k is the weight assigned to stencil k with the second-degree reconstruction polynomial approximation $\hat{f}_{k,i+1/2}$. In the WENO-CU6 framework the weights ω_k are given by

$$\omega_k = \frac{\alpha_k}{\sum_{k=0}^{3} \alpha_k}, \quad \alpha_k = d_k \left(C + \frac{\tau_6}{\beta_k + \epsilon} \right). \tag{3.3}$$

The optimal weights d_k are chosen such that the method recovers the sixth-order central method. C is a constant with $C \gg 1$. A new smoothness measure τ_6 can be found from a linear combination of the other smoothness measures β_k with

$$\tau_6 = \beta_6 - \frac{1}{6}(\beta_0 + \beta_2 + 4\beta_1) \tag{3.4}$$

and

$$\beta_k = \sum_{j=0}^{2} \Delta x^{2j-1} \int_{x-1/2}^{x_{i+1/2}} \left(\frac{\mathrm{d}^j}{\mathrm{d}x^j} \hat{f}_k(x) \right)^2 \mathrm{d}x. \tag{3.5}$$

β_6 is also calculated from (3.5) but with the six-point stencil for the sixth-order interpolation. The full method is given in [2] and with modifications for scale separation in [25].

3.2. The modified general Roe average for an ideal gas mixture

The general Roe average used in the present study is an extension of the Roe average for generalized EOS, but unlike those of Liou *et al* [26] and Shyue [27], the method is simple and satisfies the U-property exactly. Moreover, it does not introduce artificial states like that of Glaister [28] and predicts the averages directly from the adjacent states.

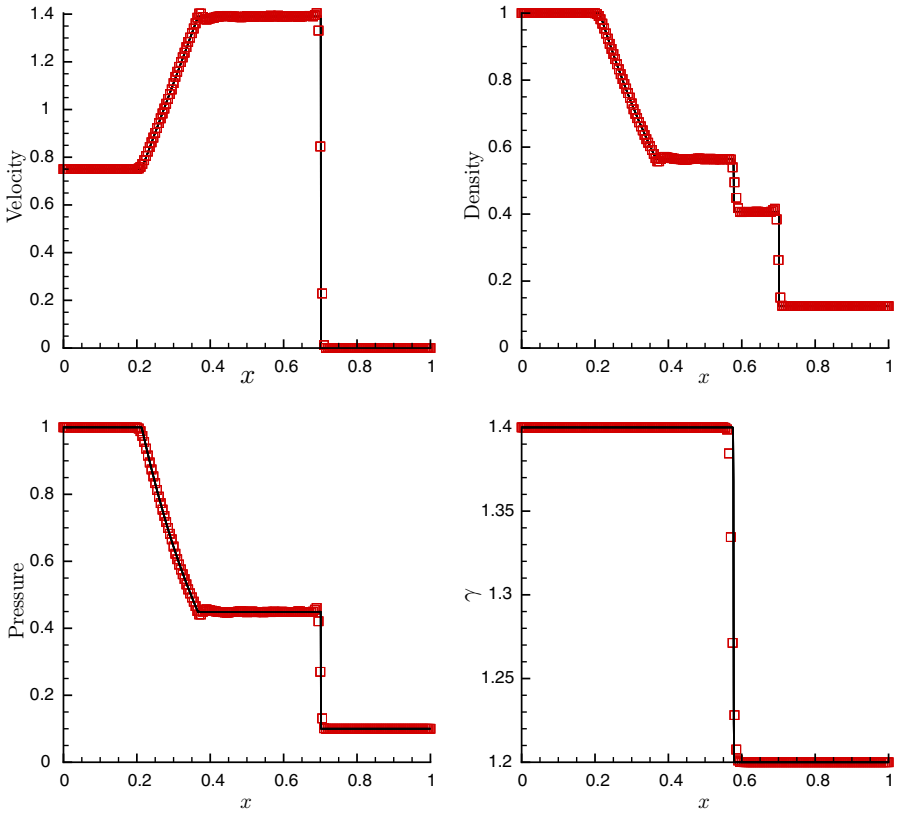

Figure 1. Results of Sod's two-material shock-tube problem for the WENO-CU6 scheme (□) on a 200-point grid compared to the reference solution (—) obtained with the WENO-5 scheme on a high-resolution 6000-point grid.

Here we apply this method with the Riemann solver of Roe. Additional challenges arise from the fact that the linear approximation between the average state and the adjacent state for a single-phase interaction, which has been assumed by Hu *et al* [23], does not hold in the present study.

According to Glaister [28], the averages of $\tilde{\rho}$, $\tilde{u}$ and $\tilde{H}$ can be obtained from

$$\tilde{\rho} = \sqrt{\rho_\mathrm{l}\rho_\mathrm{r}}, \quad \tilde{f} = \mu(f) = \frac{\sqrt{\rho_\mathrm{l}} f_\mathrm{l} + \sqrt{\rho_\mathrm{r}} f_\mathrm{r}}{\sqrt{\rho_\mathrm{l}} + \sqrt{\rho_\mathrm{r}}}, \quad f = u, H \tag{3.6}$$

and

$$\left(\frac{\tilde{p}}{\rho}\right) = \mu\left(\frac{p}{\rho}\right) + \frac{\tilde{\rho}}{2}\left(\frac{u_\mathrm{r} - u_\mathrm{l}}{\sqrt{\rho_\mathrm{l}} + \sqrt{\rho_\mathrm{r}}}\right)^2. \tag{3.7}$$

The average pressure can be evaluated from (3.7) as $\tilde{p} = \tilde{\rho}(\frac{\tilde{p}}{\rho})$. For a general EOS $p = p(\rho, e)$, the speed of sound c is given by

$$c^2 = \left.\frac{\partial p}{\partial \rho}\right|_e + \frac{p}{\rho^2}\left.\frac{\partial p}{\partial e}\right|_\rho = \Psi + \Gamma\frac{p}{\rho}, \tag{3.8}$$

where Ψ is the Grüneisen coefficient and Γ defines the material properties. Following Roe [29] and Glaister's [28] approach, one obtains the condition for the pressure difference between two adjacent states as

$$\Delta p = \tilde{\Psi}\Delta\rho + \tilde{\Gamma}[\Delta(\rho e) - \tilde{e}\Delta\rho] \tag{3.9}$$

with appropriately defined average states for the Grüneisen coefficient $\tilde{\Psi}$ and the parameter defining the material properties $\tilde{\Gamma}$.

Unlike Hu *et al* [23], we cannot assume a linear approximation between the average and the adjacent states, which would reduce the equation for the pressure difference (3.9) to

$$\Delta p = \tilde{\Psi}\Delta\rho + \tilde{\Gamma}\tilde{\rho}\Delta e, \tag{3.10}$$

but we need to find the averages $\tilde{\Psi}$ and $\tilde{\Gamma}$ based on (3.9).

One way to calculate $\tilde{\Psi}$ and $\tilde{\Gamma}$ is to assume that one of them obeys the same averaging as $\tilde{f}$ in (3.6) and calculate the other one from (3.9). This would lead to

$$\tilde{\Gamma}_{\Delta e} = \frac{\Delta p - \mu(\Psi)\Delta\rho}{\Delta(\rho e) - \tilde{e}\Delta\rho} \tag{3.11}$$

and

$$\tilde{\Psi}_{\Delta\rho} = \frac{\Delta p - \mu(\Gamma)[\Delta(\rho e) - \tilde{e}\Delta\rho]}{\Delta\rho}, \tag{3.12}$$

respectively. The averaged internal energy for an ideal gas can be found as

$$\tilde{e} = \frac{\mu(\Psi)}{\mu(\Gamma)}. \tag{3.13}$$

However, (3.11) and (3.12) are undefined if $\Delta(\rho e) - \tilde{e}\Delta\rho = 0$ or $\Delta\rho = 0$. The singularities can be removed if it is assumed that $\tilde{\Gamma} = \mu(\Gamma)$ when $\Delta(\rho e) - \tilde{e}\Delta\rho = 0$ and $\tilde{\Psi} = \mu(\Psi)$ when $\Delta\rho = 0$. Thus the modified generalized definitions of $\tilde{\Gamma}$ and $\tilde{\Psi}$ can be expressed as

$$\tilde{\Gamma} = \frac{\mu(\Psi)(w_e + \epsilon) + \tilde{\Psi}_{\Delta\rho} w_\rho}{w_e + w_\rho + \epsilon}, \quad \tilde{\Psi} = \frac{\mu(\Gamma)(w_\rho + \epsilon) + \tilde{\Gamma}_{\Delta e} w_e}{w_e + w_\rho + \epsilon} \tag{3.14}$$

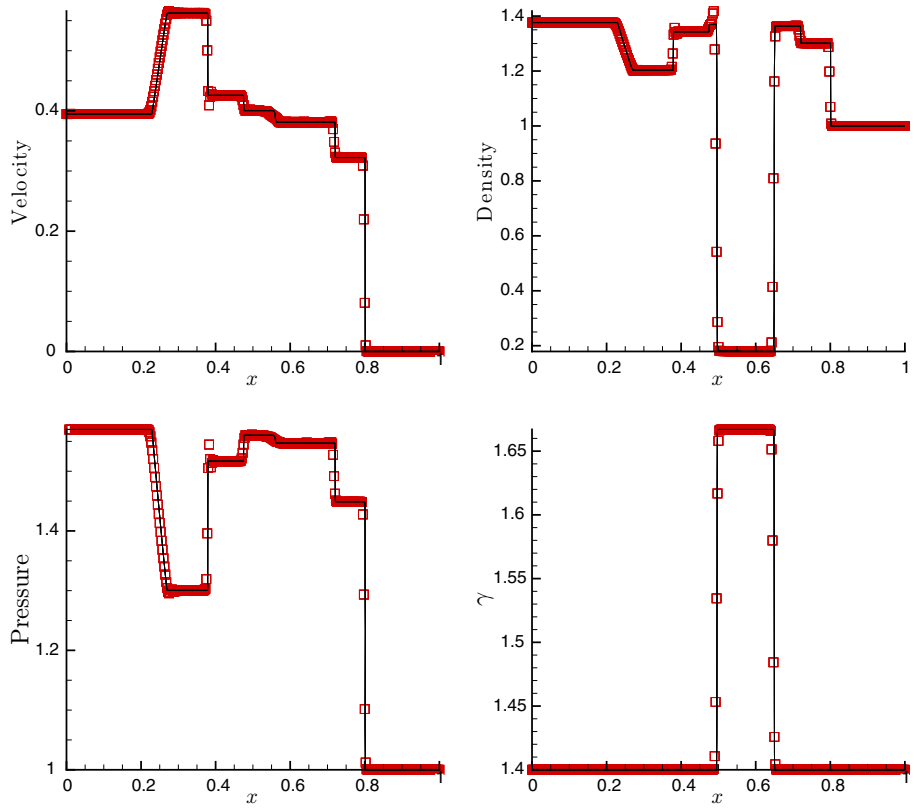

Figure 2. Results of the 1D shock–bubble interaction test case of Quirk and Karni. The WENO-CU6 solution (□) is obtained on a 400-point grid and compared to the reference solution (—) produced with the standard WENO-5 method on a high-resolution grid with 6000 grid points.

with $w_\rho = (\frac{\Delta\rho}{\tilde{\rho}})^2$ and $w_e = (\frac{\Delta(\rho e) - \tilde{e}\Delta\rho}{\tilde{\rho}\tilde{e}})^2$, where ϵ is a small number. Then the speed of sound is given by

$$c^2 = \tilde{\Psi} + \frac{\tilde{p}}{\tilde{\rho}}\tilde{\Gamma}. \tag{3.15}$$

4. Validation of the numerical scheme

As a first validation test case, Sod's two-material shock-tube problem is used to show the correct and consistent implementation of the WENO-CU6 scheme and the multicomponent model with its modified generalized Roe average. The initial condition is

$$(\rho, u, p, \gamma) = \begin{cases} (1.0, 0.75, 1.0, 1.4) & \text{if} \quad 0.0 < x < 0.3, \\ (0.125, 0.0, 0.1, 1.2) & \text{if} \quad 0.3 < x < 1.0. \end{cases} \tag{4.1}$$

Results are shown for the final time $t = 0.2$.

The solution in figure 1 obtained with the WENO-CU6 scheme on a 200-point grid agrees very well with the reference solution. The reference solution is produced with a standard WENO-5 scheme on a high-resolution grid with 6000 points. The results of the WENO-CU6 method slightly oscillate because of the non-dissipative properties of the method. A more dissipative scheme would damp such disturbances at each time step and hence smooth out the solution. In a non-dissipative scheme (as the WENO-CU6 scheme is in smooth flow regions) the oscillations show a dispersive character as they travel both up- and downstream.

The second test case is the 1D shock–bubble interaction case of Quirk and Karni (cited by Abgrall [16]). It consists of a shock wave that is traveling in air to the right. In the pre-shock state a bubble of helium is located between $0.4 < x < 0.6$. The shock wave is initially at $x = 0.25$ and the initial conditions are

$$(\rho, u, p, \gamma) = \begin{cases} (1.3765, 0.3948, 1.57, 1.4) & \text{if} \quad 0.0 < x < 0.25, \\ (1.0, 0.0, 1.0, 1.4) & \text{if} \quad 0.25 < x < 0.4 \\ & \text{or} \quad 0.6 < x < 1.0, \\ (0.138, 0.0, 1.0, 1.67) & \text{if} \quad 0.4 < x < 0.6. \end{cases} \tag{4.2}$$

The results of the WENO-CU6 method are given in figure 2 and compared to the reference solution that was obtained by using a conventional WENO-5 approach. The solution of the WENO-CU6 method was sampled on a 400-point grid. The reference solution was sampled on a high-resolution 6000-point grid. Although the WENO-CU6 results were obtained on a grid that is 15 coarser than the grid of the reference solution, they are both in very good agreement. A quantitative comparison of the present results with those of Wang [21] showed a clear improvement. Also a qualitative comparison with the results of Marquina and Pulet [20] corroborated this conclusion.

5. Initial conditions for RMI

The experiments of Jacobs and Krivets [1] provide the initial conditions for our 2D investigation of the RMI in an inviscid

regime. The vertical shock tube used in the experiment has a driver section that is filled with air at ambient pressure and temperature. In the test section an interface of air–SF_6 is formed as the heavier SF_6 flows upwards and collides with air flowing from top to down. Both gases exit through horizontal slots in the test section. A sinusoidal interface between the two gases is formed by oscillating the entire shock tube in the horizontal direction. This membrane-less technique was first proposed by Jones and Jacobs [14].

The initial conditions of the experimental setup considered in the present numerical study are as follows: The shock wave has a strength of $M_s = 1.3$ in air. The sinusoidal interface of air–SF_6 has a pre-shock amplitude of $a_0^- = 2.9\,\text{mm}$ and a wavelength of $\lambda = 59\,\text{mm}$. The location of the material interface is then calculated from $\eta = x_i + a_0^- \cos(2\pi y)$. The diffusion layer between the fluids is given by [30]

$$f(\delta) = f_1(1-\delta) + f_r\delta,$$
$$\delta = \frac{(1+\tanh(\frac{\Delta R}{\epsilon}))}{2}, \qquad (5.1)$$
$$\epsilon = D\sqrt{\Delta x_i \Delta y_i}$$

and $f = \rho, z_{SF_6}$. ΔR is the distance from the material interface. The densities of air and SF_6 in ambient conditions led to a pre-shock Atwood number of $A^- = 0.605$. The interface is initialized at $x_I = 30\,\text{mm}$ and the shock at $x_s = 10\,\text{mm}$. The time is initialized to zero ($t = 0$) when the shock first impacts the SF_6 gas.

5.1. Computational domain

The 2D computational domain is discretized by a Cartesian grid. We use for all simulations a mesh size of 256 cells per initial wavelength λ. The 'numerical test section' is surrounded by layers of coarser grids in order to avoid shock reflections at the inlet and outlet.

5.2. Non-dimensionalization

The reference scales to non-dimensionalize the governing equations are defined here. The reference density is set to the pre-shock density of air $\rho_{ref} = \rho_{air} = 1.351\,\text{kg m}^{-3}$. Accordingly, the reference pressure is chosen to be the pre-shock pressure $p_{ref} = 0.956$ bar. The reference length scale is the initial wavelength of the sinusoidal interface $L_{ref} = \lambda = 59\,\text{mm}$ and the reference time scale is $t_{ref} = \sqrt{\frac{\rho_{ref}}{p_{ref}}} L_{ref}$.

6. Numerical results

6.1. Single-fluid algorithm

In this subsection, the ratio of specific heats $\overline{\gamma}$ in (2.5) is assumed to be constant with the same value of $\overline{\gamma} = 1.276$ for both air and SF_6 and hence is referred to as single-fluid algorithm. Figure 3 shows the experimental results of Jacobs and Krivets [1] along with our numerical results obtained with the standard WENO-5 and the WENO-CU6 method at three different times $t = 3.06\,\text{ms}$, $t = 4.16\,\text{ms}$ and $t = 6.06\,\text{ms}$.

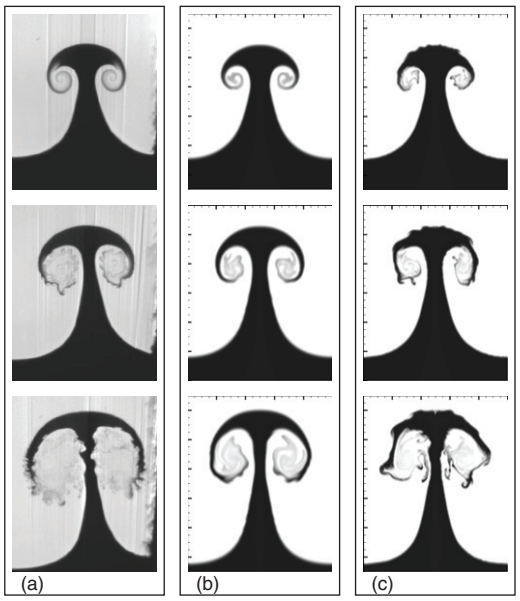

Figure 3. Experimental results of Jacobs and Krivets [1] (a) compared to the single-fluid results obtained with the standard WENO-5 method (b) and the WENO-CU6 method (c) at three different times $t = 3.06\,\text{ms}$, $t = 4.16\,\text{ms}$ and $t = 6.06\,\text{ms}$.

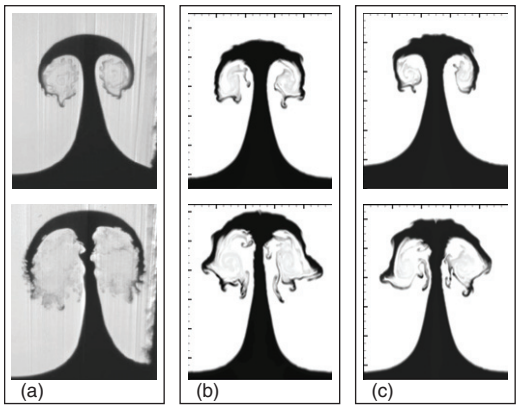

Figure 4. In (b) the post-shock conditions of the experiment are matched, whereas in (c) the pre-shock conditions are matched and compared to the experiment (a) at times $t = 4.16\,\text{ms}$ and $t = 6.06\,\text{ms}$.

The comparison shows that the lower-order WENO-5 method preserves large-scale structures and symmetry to later times, while WENO-CU6 better resolves small-scale structures, leading to symmetry breaking and increased mixing. This better behavior is in agreement with the findings of Latini *et al* [11].

WENO-5 cannot reproduce the secondary instabilities on the mushroom stem, whereas WENO-CU6 clearly shows the same typical stem disturbances as the experiment at $t = 6.06\,\text{ms}$. On the other hand, it also shows instabilities on top of the mushroom which are not observed in the experiment. We believe that the origin of these numerical instabilities could be because of neglecting viscous effects, which makes the WENO-CU6 scheme less dissipative than the real physical mechanisms. On the other hand, other numerical schemes apparently are too dissipative. Both discretization schemes are unable to predict correctly the large-scale structure such

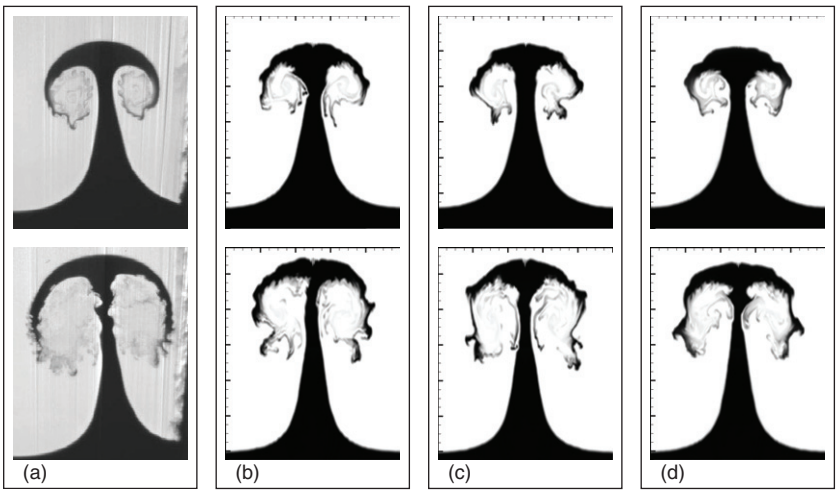

Figure 5. Investigation of the impact of the diffusion layer on the late-time Richtmyer–Meshkov development with increasing the diffusion layer thickness from (b) $D = 4$ to (c) $D = 8$ to (d) $D = 16$ at times $t = 4.16$ ms and $t = 6.06$ ms.

as the mushroom head diameter and stem diameter of the RMI experiment.

Richtmyer described the early linear growth rate of the instability as a function of the post-shock parameters, a_0^+ the post-shock amplitude, A^+ the post-shock Atwood number, the velocity jump ΔU_0 associated with the shock passage and k the initial perturbation wavelength

$$ka(t) = ka_0^+ + k^2 a_0^+ A^+ \Delta U_0 t. \tag{6.1}$$

From (6.1) it immediately follows that in order to match the correct initial growth rate and accordingly the later development, one needs to reproduce the correct post-shock parameters. As the single-fluid method assumes constant $\overline{\gamma}$, it is not possible to have matching pre- and post-shock states. Thus, it is preferable to match the post-shock state in order to improve the agreement in the large-scale structures between experiments and numerics at late times.

Figure 4(b) shows the result when the post-shock conditions of the experiment are matched. The pre-shock conditions are matched in figure 4(c). Comparing figures 4(b) and (c) to the experiment given in figure 4(a), a clear improvement of the large-scale structure is observed in figure 4(b). It shows a wider mushroom head and a thinner stem, which captures better the global characteristics of the RMI experiments.

6.2. Multifluid algorithm

In this subsection, $\overline{\gamma}$ is not assumed to be constant but computed from (2.6) with $\gamma_{\text{air}} = 1.276$ and $\gamma_{\text{SF}_6} = 1.093$. A transport equation is solved for the volume fraction (2.4) to account for the variable ratio of specific heats. By means of (2.4) and the modified general Roe average of section 3.2 we are able to simulate the material interface without the appearance of spurious pressure oscillations.

As the initial driving force of RMI is the vorticity deposition on the material interface caused by the misaligned pressure and density gradient, it is of crucial importance to properly match the pressure gradient and the density gradient. The pressure gradient is associated with the Mach number of the incident shock wave and therefore is much better quantifiable than the density gradient.

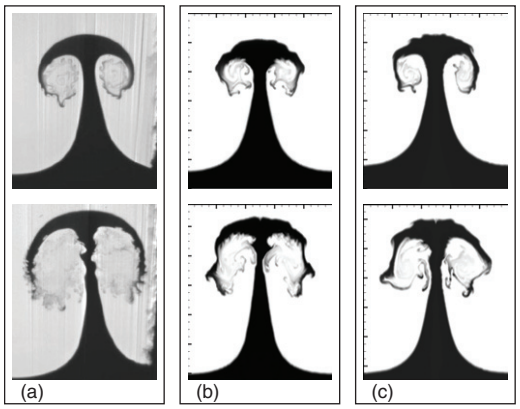

Figure 6. Comparison of the multifluid (b) and single-fluid (c) algorithms to the experiments (a) at times $t = 4.16$ ms and $t = 6.06$ ms.

In order to quantify the uncertainty of the density distribution across the interface, three different diffusion layer thicknesses are considered. Figure 5 shows a sequence of simulations with increasing diffusion layer thicknesses $D = 4$, $D = 8$ and $D = 16$, see (5.1). The vorticity deposited on the interface decreases as the density gradient is reduced from the left, figure 5(b), to the right, figure 5(d). Although the mushroom stem in figure 5(d) shows a non-sinusoidal perturbation the overall shape agrees best with the experiment. $D = 16$ is therefore used for making a comparison to the results obtained using WENO-CU6 and a constant ratio of specific heats in figure 6.

Figure 6 reveals a clear improvement of the multifluid algorithm over the single-fluid algorithm. The global characteristics are captured much better in figure 6(b) than in figure 6(c). When the late-time development of the RMI is of interest the correct compressibility of the fluids involved needs to be captured, which requires a multifluid simulation with variable material properties.

7. Concluding remarks

The 2D simulations of the single-mode RMI using the recently developed WENO-CU6 reconstruction method of Hu *et al* [2]

were conducted and compared with the experiments of Jacobs and Krivets [1]. The multicomponent model for stiffened gases by Shyue [3] was used to account for multiple species. However, the high-order method employed made it necessary to modify the general Roe average of Hu *et al* [23] in order to capture material interfaces without the occurrence of spurious pressure oscillations. In two 1D test cases it was shown that the WENO-CU6 method together with the modified general Roe average was capable of capturing accurately material interfaces without introducing undesirable amounts of numerical dissipation.

In a first sequence of simulations the ratio of specific heats $\overline{\gamma}$ was assumed to be constant for both fluids. The fluxes were reconstructed with the WENO-CU6 and the standard WENO-5 method and compared to the experiments. It was concluded that the lower-order WENO-5 method preserves large-scale structures and symmetry to later times, while the WENO-CU6 better resolves small-scale structures, leading to earlier symmetry breaking and increased mixing. This better behavior is in agreement with the findings of Latini *et al* [11]. However, the global characteristic structures of RMI were matched neither by the WENO-CU6 method nor by the WENO-5 method. This is due to the fact that the linear growth rate of RMI essentially depends on the post-shock state of the instability. A mismatch of the post-shock state essentially leads to wrong prediction of the late-time development. Thus, in terms of accuracy, it is much more preferable to match the post-shock state than the pre-shock state in single-fluid simulations.

The initial driving force of RMI is the vorticity deposition on the material interface caused by the non-parallel pressure and density gradient. However, unlike the pressure gradient, the density gradient associated with the material interface is not easy to quantify in experiments. Therefore, a sequence of multifluid simulations with different diffusion layer thicknesses were conducted to assess the uncertainty in the density gradient. The multifluid simulations showed a considerable improvement over the single-fluid simulations where the pre-shock state is matched.

Acknowledgments

VKT is a member of the TUM Graduate School and acknowledges the support he received.

References

[1] Jacobs J W and Krivets V V 2005 Experiments on the late-time development of single-mode Richtmyer–Meshkov instability *Phys. Fluids* **17** 034105
[2] Hu X Y, Wang Q and Adams N A 2010 An adaptive central-upwind weighted essentially non-oscillatory scheme *J. Comput. Phys.* **229** 8952–65
[3] Shyue K-M 1998 An efficient shock-capturing algorithm for compressible multicomponent problems *J. Comput. Phys.* **142** 208–42
[4] Richtmyer R D 1960 Taylor instability in shock acceleration of compressible fluids *Commun. Pure Appl. Math.* **XIII** 297–319
[5] Meshkov E E 1969 Instability of the interface of two gases accelerated by a shock wave *Fluid Dyn.* **4** 101–4
[6] Taylor G I 1950 The instability of liquid surfaces when accelerated in a direction perpendicular to their planes *Proc. R. Soc.* A **201** 192
[7] Arnett D 2000 The role of mixing in astrophysics *Appl. J. Suppl.* **127** 213–17
[8] Yang J, Kubota T and Zukoski E E 1993 Applications of shock-induced mixing to supersonic combustion *AIAA J.* **31** 854–62
[9] Brouillette M 2002 The Richtmyer-Meshkov instability *Annu. Rev. Fluid Mech.* **34** 445–68
[10] Zabusky N 1999 Vortex paradigm for accelerated inhomogenous flows: visiometrics for the Rayleigh–Taylor and Richtmyer–Meshkov environments *Annu. Rev. Fluid Mech.* **31** 495
[11] Latini M, Schilling O and Don W S 2007 Effects of WENO flux reconstruction order and spatial resolution on reshocked two-dimensional Richtmyer–Meshkov instability *J. Comput. Phys.* **221** 805–36
[12] Latini M, Schilling O and Don W S 2007 High-resolution simulations and modeling of reshocked single-mode Richtmyer–Meshkov instability: comparison to experimental data and to amplitude growth model predictions *Phys. Fluids* **19** 024104
[13] Collins B D and Jacobs J W 2002 PLIF flow visualization and measurements of the Richtmyer–Meshkov instability of an air/SF_6 interface *J. Fluid Mech.* **464** 113–36
[14] Jones M A and Jacobs J W 1997 A membraneless experiment for the study of Richtmyer–Meshkov instability of a shock-accelerated gas interface *Phys. Fluids* **9** 3078–85
[15] Karni S 1994 Multicomponent flow calculations by a consistent primitive algorithm *J. Comput. Phys.* **112** 31–43
[16] Abgrall R 1996 How to prevent pressure oscillations in multicomponent flow calculations: a quasi conservative approach *J. Comput. Phys.* **125** 150–60
[17] Karni S 1996 Hybrid multifluid algorithms *SIAM J. Sci. Comput.* **17** 1019
[18] Abgrall R 2001 Computations of compressible multifluids *J. Comput. Phys.* **169** 594–623
[19] Allaire G, Clerc S and Kokh S 2002 A five equation model for the simulation of the interface between compressible fluids *J. Comput. Phys.* **181** 577–616
[20] Marquina A and Pulet P 2003 A flux-split algorithm applied to conservative models for multicomponent compressible flows *J. Comput. Phys.* **185** 120–38
[21] Wang S 2004 A thermodynamically consistent and fully conservative treatment of contact discontinuities for compressible multicomponent flows *J. Comput. Phys.* **195** 528–59
[22] Shu C-W 1997 Essentially non-oscillatory and weighted essentially non-oscillatory schemes for hyperbolic conservation laws *ICASE Report* no. 97-65
[23] Hu X Y, Adams N A and Iaccarino G 2009 On the HLLC Riemann solver for interface interaction in compressible multi-fluid flow *J. Comput. Phys.* **228** 6572–89
[24] Toro E F 1999 *Riemann Solvers and Numerical Methods for Fluid Dynamics* (Berlin: Springer)
[25] Hu X Y and Adams N A 2011 Scale separation for implicit large eddy simulation *J. Comput. Phys.* **230** 7240–9
[26] Liou M S, B van Leer and Shuen J S 1990 Splitting for inviscid fluces for real gas *J. Comput. Phys.* **87** 1–24
[27] Shyue K M 2001 A fluid-mixture type algorithm for compressible multicomponent flow with Mie–Gruneisen equation of state *J. Comput. Phys.* **171** 678–707
[28] Glaister P 1988 An approximate linearised Riemann solver for the Euler equations for real gases *J. Comput. Phys.* **74** 382–408
[29] Roe P L 1981 Approximate Riemann solvers, parameter and difference schemes *J. Comput. Phys.* **43** 357–72
[30] Shankar S K, Kawai S and Lele S K 2010 Numerical simulation of multicomponent shock accelerated flows and mixing using localized artificial diffusivity method *4th AIAA Aerospace Science Meeting*

PHYSICS OF FLUIDS **26**, 026101 (2014)

Quantification of initial-data uncertainty on a shock-accelerated gas cylinder

V. K. Tritschler,[a] A. Avdonin, S. Hickel, X. Y. Hu, and N. A. Adams
Institute of Aerodynamics and Fluid Mechanics, Technische Universität München, 85747 Garching, Germany

(Received 21 August 2013; accepted 29 January 2014; published online 18 February 2014)

We quantify initial-data uncertainties on a shock accelerated heavy-gas cylinder by two-dimensional well-resolved direct numerical simulations. A high-resolution compressible multicomponent flow simulation model is coupled with a polynomial chaos expansion to propagate the initial-data uncertainties to the output quantities of interest. The initial flow configuration follows previous experimental and numerical works of the shock accelerated heavy-gas cylinder. We investigate three main initial-data uncertainties, (i) shock Mach number, (ii) contamination of SF_6 with acetone, and (iii) initial deviations of the heavy-gas region from a perfect cylindrical shape. The impact of initial-data uncertainties on the mixing process is examined. The results suggest that the mixing process is highly sensitive to input variations of shock Mach number and acetone contamination. Additionally, our results indicate that the measured shock Mach number in the experiment of Tomkins *et al.* ["An experimental investigation of mixing mechanisms in shock-accelerated flow," J. Fluid. Mech. **611**, 131 (2008)] and the estimated contamination of the SF_6 region with acetone [S. K. Shankar, S. Kawai, and S. K. Lele, "Two-dimensional viscous flow simulation of a shock accelerated heavy gas cylinder," Phys. Fluids **23**, 024102 (2011)] exhibit deviations from those that lead to best agreement between our simulations and the experiment in terms of overall flow evolution. © *2014 AIP Publishing LLC*. [http://dx.doi.org/10.1063/1.4865756]

I. INTRODUCTION

The impulsive acceleration of a density inhomogeneity and the subsequent high-speed fluid mixing was first studied by Richtmyer,[1] both analytically and numerically. Later, Meshkov[2] confirmed Richtmyer's predictions experimentally. The Richtmyer-Meshkov instability (RMI) is driven by baroclinic vorticity production at the fluid interface. The vorticity production results from a misalignment of the pressure gradient ∇p associated with the shock wave and the density gradient $\nabla \rho$ of the material interface. At intermediate and late times the initial RMI is followed by Kelvin-Helmholtz instabilities as a result of the velocity shear across the deformed material interface. If the initial energy deposition due to the shock wave is sufficient, the flow evolves into a turbulent mixing zone.

Accurate numerical prediction of high-speed multicomponent mixing problems is of great importance for technical applications and natural phenomena.[3–5] In the past decade, RMI in shock-bubble interactions has been widely studied analytically, experimentally, and numerically. Haas and Sturtevant[6] pioneered the experimental approach and produced accurate experimental images of the bubble evolution. Later, Jones and Jacobs[7] established a membrane-free technique that allows experimental investigation with much better defined initial conditions. In a recent experimental investigation, Tomkins *et al.*[8] investigated the interaction of a shock wave with a heavy-gas cylinder. By using the membrane-free technique of Jones and Jacobs[7] they were able to record very clear

[a] volker.tritschler@aer.mw.tum.de

high-quality images not only of the heavy-gas concentration of the cylinder but also of the mixing rates.

Shankar *et al.*[9] employed the experimental initial conditions of Tomkins *et al.*[8] in their numerical simulations. They reported, for the first time, simulation results with four species N_2, O_2, SF_6, and C_3H_6O (acetone) at finite Reynolds numbers. Despite the fact that the authors produced grid-converged results with a high-order numerical method, they were not able to reproduce correctly the global characteristics seen in the experiment, partially due to three-dimensional effects, but also due to unknown uncertainties in the initial data of the experiment. This motivates a rigorous quantification of typical initial-data uncertainty on a shock-accelerated heavy-gas cylinder and how these uncertainties may affect the output quantities of interest (QoI).

Three main sources of uncertainty are investigated; (i) shock Mach number, (ii) contamination of SF_6 with acetone that serves as a tracer species in the experiment, and (iii) initial deviations of the SF_6 region from a perfect cylindrical shape, cf. Shankar *et al.*[9] and Tomkins *et al.*[8] The impact of these main sources of initial-data uncertainty on the time evolution of the heavy-gas region is quantified by performing a simulation-based uncertainty quantification.

Specifically, the focus of this paper is (i) to investigate the effect of the shock Mach number, the contamination of the SF_6 cylinder with acetone and the initial deviation of the heavy-gas region from a perfect cylindrical shape on mixing processes in the flow field, (ii) to classify the relative significance of the uncertainty parameters with respect to their impact on flow dynamics, (iii) to quantify the cross-correlation between the uncertainty parameters and finally, (iv) to identify and investigate the source of typical differences between numerical simulations and experiment reported in the literature. Note that the main objective of this study is not to reproduce the experiment of Tomkins *et al.*,[8] but rather to clarify the general effect of initial-data uncertainties on the mixing process and the unsteady flow dynamics of a shock-accelerated heavy-gas cylinder.

This paper is structured as follows: Sec. II summarizes the experimental setup of Tomkins *et al.*[8] and defines the three initial-data uncertainty parameters under investigation. Sec. III outlines the governing equations, the employed multicomponent model, the uncertainty quantification method, and gives a detailed description of the numerical setup. In Sec. IV, we define the output QoI, and finally, in Sec. V, we present and discuss the results of the uncertainty quantification. Here, we also provide a best fit result to the experiment of Tomkins *et al.*[8] We conclude with a summary in Sec. VI.

II. SHOCK-CYLINDER INTERACTION

A. Experimental setup

The present numerical investigation follows the experiment of Tomkins *et al.*[8] where a heavy-gas cylinder embedded in air is impacted by a $M = 1.2$ shock wave. The heavy gas consists of SF_6 and is seeded with acetone, which serves as a tracer for laser-induced fluorescence visualization. The shock wave is generated in air by puncturing a membrane between a pressurized driver section and a driven section. In the test section, the shock wave hits the heavy-gas cylinder, which was generated using the membraneless approach of Jones and Jacobs.[7] The maximum mass fraction of heavy gas in the circular region was estimated in the experiment to $Y_{HG}^{max} = 0.83$ with $Y_{HG}^{max} = Y_{Ac}^{max} + Y_{SF_6}^{max}$.

B. Sources of input uncertainty

In this study, the heavy-gas region geometry, heavy-gas concentration and contamination, and the strength of the shock wave are considered as the three main sources of initial-data uncertainty.

1. Mach number

The Mach number M of a shock wave determines the pressure jump across the shock and thus affects baroclinic vorticity production at the fluid interface. The domain of the Mach number

uncertainty is estimated as

$$M \in [1.18, 1.22], \tag{1}$$

based on uncertainty domains found in similar configurations.[10,11]

2. Presence of a tracer species

The contamination of the cylinder with the tracer acetone changes the density of the heavy-gas cylinder and hence also affects baroclinic vorticity production. The maximum mass fraction of acetone Y_{Ac}^{max} is introduced as an additional uncertainty parameter. Experimental data on the amount of acetone in the cylinder are not available and accordingly need to be estimated. We assume Y_{Ac}^{max} to be

$$Y_{Ac}^{max} \in [0.05, 0.25], \tag{2}$$

as a similar domain for the acetone concentration were considered in the numerical investigation of Shankar *et al.*[9] and the experimental work of Balasubramanian *et al.*[12]

3. Initial imperfections of the heavy-gas region

The initial deviation of the heavy-gas region from a cylindrical shape affects the baroclinic vorticity production. The definition of this uncertainty parameter is motivated by Fig. 2 in Tomkins *et al.*[8] which shows that the cross-section of the heavy-gas cylinder in the experiment is not perfectly circular. We approximate the heavy-gas region cross-section as an ellipse with eccentricity e as uncertainty parameter

$$e \in [-0.5, 0.5]. \tag{3}$$

When $e > 0$ the semi-major axis is aligned with the streamwise direction, $e < 0$ has the opposite effect, and $e = 0$ corresponds to a perfect circular cylinder. The cross-sections of the heavy-gas region with $e = -0.5$, $e = 0.0$, and $e = 0.5$ are shown in Fig. 2.

III. NUMERICAL MODEL

A. Governing equations

We solve numerically the two-dimensional multicomponent Navier-Stokes equations

$$\frac{\partial \rho}{\partial t} + \nabla \cdot (\rho \boldsymbol{u}) = 0, \tag{4}$$

$$\frac{\partial (\rho \boldsymbol{u})}{\partial t} + \nabla \cdot (\rho \boldsymbol{u}\boldsymbol{u} + p\underline{\boldsymbol{\delta}} - \underline{\boldsymbol{\tau}}) = 0, \tag{5}$$

$$\frac{\partial E}{\partial t} + \nabla \cdot [(E + p)\boldsymbol{u}] - \nabla \cdot (\underline{\boldsymbol{\tau}} \cdot \boldsymbol{u} - \boldsymbol{q_c} - \boldsymbol{q_d}) = 0, \tag{6}$$

$$\frac{\partial \rho Y_i}{\partial t} + \nabla \cdot (\rho \boldsymbol{u} Y_i) - \nabla \cdot (\rho D_i \nabla Y_i) = 0. \tag{7}$$

In system (4)–(7), ρ is the mixture density, $\boldsymbol{u}$ is the velocity, p is the pressure, E is the total energy, Y_i is the mass fraction of species $i = 1, 2, ...K$, K is the number of species, and $\underline{\boldsymbol{\delta}}$ is the unit tensor. The viscous stress tensor $\underline{\boldsymbol{\tau}}$ is defined for a Newtonian fluid with the mixture viscosity $\overline{\mu}$. D_i is the effective binary diffusion coefficient of species i. The heat conduction and the interspecies diffusional heat flux[13] are given by

$$\begin{aligned} \boldsymbol{q}_c &= -\overline{\kappa} \nabla T, \\ \boldsymbol{q}_d &= \sum_{i=1}^{K} h_i \boldsymbol{J_i} \end{aligned} \tag{8}$$

with

$$\boldsymbol{J_i} \approx -\rho \left(D_i \nabla Y_i - Y_i \sum_{j=1}^{K} D_j \nabla Y_j \right). \tag{9}$$

The mixture heat conductivity coefficient $\overline{\kappa}$, the mixture viscosity $\overline{\mu}$, and the effective binary diffusion coefficient D_i are given in Appendixes A and B.

The equations are closed with the equation of state (EOS) for an ideal gas

$$p(\rho e, Y_1, Y_2, ..., Y_K) = (\overline{\gamma} - 1)\, \rho e, \tag{10}$$

where $\overline{\gamma}$ is the ratio of specific heats and e is the internal energy of the system defined as

$$\rho e = E - \frac{\rho}{2} \boldsymbol{u}^2. \tag{11}$$

B. Numerical scheme

The hyperbolic part of the Navier-Stokes equations in one spatial dimension can be written as a quasi-linear system

$$\boldsymbol{U_t} + \boldsymbol{A}\boldsymbol{U_x} = 0, \tag{12}$$

where $\boldsymbol{A} = \boldsymbol{A}(\boldsymbol{U}) = \frac{\partial \boldsymbol{F}}{\partial \boldsymbol{U}}$ is the Jacobian matrix with N real eigenvalues $\lambda_i(\boldsymbol{U})$ corresponding to N eigenvectors $R_i(\boldsymbol{U})$.

For a multicomponent system with K species the Jacobian $\boldsymbol{A}$ is[14,15]

$$\boldsymbol{A} = \begin{pmatrix} 0 & 1 & 0 & 0 & 0 & 0 & \cdots & 0 \\ -u^2 + \frac{1}{2}(\overline{\gamma}-1)q^2 + X & (3-\overline{\gamma})u & (1-\overline{\gamma})v & (1-\overline{\gamma})w & \overline{\gamma}-1 & X_1 & \cdots & X_{K-1} \\ -uv & v & u & 0 & 0 & 0 & \cdots & 0 \\ -uw & w & 0 & u & 0 & 0 & \cdots & 0 \\ u[\frac{1}{2}(\overline{\gamma}-1)q^2 - H] + uX & H - (\overline{\gamma}-1)u^2 & (1-\overline{\gamma})uv & (1-\overline{\gamma})uw & \overline{\gamma}u & uX_1 & \cdots & uX_{K-1} \\ -uY_1 & Y_1 & 0 & 0 & 0 & u & \cdots & 0 \\ \vdots & \vdots & \vdots & \vdots & \vdots & & \ddots & \\ -uY_{K-1} & Y_{K-1} & 0 & 0 & 0 & 0 & \cdots & u \end{pmatrix}, \tag{13}$$

where X and X_i are given by

$$X = \frac{\partial \overline{\gamma}}{\partial \rho} \rho e, \tag{14}$$

$$X_i = \frac{\partial \overline{\gamma}}{\partial \rho Y_i} \rho e \quad \text{for} \quad i \in [1, K-1]. \tag{15}$$

H is the enthalpy and $q = \|\boldsymbol{u}\|^2$. The numerical solution of Eq. (12) thus requires a flux projection on local characteristics. For this purpose the corresponding Roe-averaged matrix $\widetilde{\boldsymbol{A}}$ needs to be calculated, along with its right and left eigenvectors.[16] The numerical fluxes at the cell boundaries $f_{i\pm1/2}$ are reconstructed from cell averaged values with the low-dissipation central-upwind 6th-order weighted essentially non-oscillatory scheme (WENO-CU6) of Hu *et al.*[17] After reconstruction of the numerical fluxes at the cell boundaries the fluxes are projected back onto the physical field using the right eigenvectors. A local switch to a Lax-Friedrichs flux is used as entropy fix, see, e.g., Toro.[18] Equation (12) is evolved in time using a third-order total variation diminishing Runge-Kutta scheme.[19] It is important to note, that only $K-1$ species are projected onto the characteristic space. Species K follows from the conservation of mass and the $K-1$ other species. The numerical scheme has been tested extensively and validated for similar flows.[20,21]

C. Uncertainty quantification methodology

The goal of the uncertainty quantification method is to determine the uncertainty of the output QoI (response functions) for a given uncertainty of input parameters. The uncertainty quantification analysis is performed with a polynomial chaos expansion (PCE) provided by the Dakota software package.[22] PCE is a general framework for the approximate representation of random response functions R in terms of finite-dimensional truncated series expansions in standardized (centered and normalized) random variables $\boldsymbol{\xi} = [\xi_1, \xi_2, ...]$,

$$R \cong \sum_{i=0}^{P} \alpha_i \Psi_i(\boldsymbol{\xi}). \tag{16}$$

Here $\Psi_i(\boldsymbol{\xi})$ are multivariate polynomials, which involve products of the one-dimensional orthogonal basis polynomials. There is an optimal polynomial family for typical probability distributions of an uncertain input parameter.[22] Since the individual probability distributions of the input parameters are unknown, for simplicity we assume a uniform distribution for all input parameters. In the case of a uniform distribution suitable PCE polynomials are tensor-products of one-dimensional Legendre polynomials for $\Psi(\boldsymbol{\xi})$. An explicit representation of a Legendre polynomial of degree n is given by

$$\psi_n(\xi_i) = 2^n \sum_{k=0}^{n} \xi_i^k \binom{n}{k} \binom{(n+k-1)/2}{n}. \tag{17}$$

To transform a parameter x_i into a standardized parameter ξ_i, the following linear transformation is applied

$$\xi_i = \frac{x_i - \mu_i}{\sigma_i}, \tag{18}$$

where μ_i is the mean value and σ_i is the standard deviation of x_i. For continuous, independent, uniformly distributed parameters it is $\mu_i = (x_{i,\,max} + x_{i,\,min})/2$ and $\sigma_i = \left(x_{i,max} - x_{i,min}\right)/\sqrt{12}$. A tensor-product expansion is used to construct multivariate polynomials. The total number of terms N_t in an expansion with polynomials of order p_i involving n random variables is given by

$$N_t = \prod_{i=1}^{n} (p_i + 1). \tag{19}$$

Since the basis polynomials are orthogonal one can compute α_j by projection from Eq. (16),

$$\alpha_j = \frac{\langle R, \Psi_j \rangle}{\langle \Psi_j^2 \rangle} = \frac{1}{\langle \Psi_j^2 \rangle} \int_{\Omega} R \Psi_j \rho(\boldsymbol{\xi}) d\boldsymbol{\xi}, \tag{20}$$

where $\rho(\boldsymbol{\xi}) = \prod_{i=1}^{n} \rho_i(\xi)$ is a joint probability density function. The probability density function of a single random variable in the case of a uniform distribution is $\rho_i^{uniform} = 1/2$. Ω is a domain spanned by ξ_i. Since only discrete values of R and ξ_i are available, integration of Eq. (20) has to be performed numerically. In the case of tensor-product expansion and uniform distribution Dakota performs integration with the Gauss-Legendre quadrature rule. This quadrature rule with j integration points yields an exact result for polynomials of degree $2j - 1$. The highest order of the integrand in Eq. (20) is $2p = 2\sum_{i=1}^{n} p_i$ (Ψ_j is of order p and R is modeled to be of order p). Therefore, $p_i + 1$ integration points in each dimension are needed to obtain good accuracy in α_j. The denominator of Eq. (20) is computed analytically. One can perform nested quadrature with Gauss-Patterson quadrature rules. The advantage is that previous integration points can be reused for higher order PCE. Nevertheless, nested integration requires $p_i + 2$ integration points for the same accuracy as in the non-nested case. For three dimensions the nested grid becomes too expensive. Therefore, non-nested quadrature of 4th-order accuracy in each dimension with 125 integration points is chosen in the present investigation. Mean and variance can be computed directly from Eq. (16) with

known α_j,

$$\mu = \langle R \rangle \cong \sum_{k=0}^{P} \alpha_k \langle \Psi_k(\boldsymbol{\xi}) \rangle, \tag{21}$$

$$\Sigma = \langle (R-\mu)^2 \rangle \cong \sum_{k=0}^{P} \sum_{l=0}^{P} \langle \alpha_k \alpha_l \Psi_k(\boldsymbol{\xi}) \Psi_l(\boldsymbol{\xi}) \rangle = \sum_{k=0}^{P} \alpha_k^2 \langle \Psi_k(\boldsymbol{\xi})^2 \rangle, \tag{22}$$

where $\langle \Psi_k(\boldsymbol{\xi}) \rangle$ and $\langle \Psi_k(\boldsymbol{\xi})^2 \rangle$ are integrated analytically. Besides the computation of these moments PCE is used to perform local sensitivity analysis, i.e., to compute derivatives of a response function with respect to an expansion variable

$$\left. \frac{\partial R}{\partial \xi_i} \right|_{<\boldsymbol{\xi}>} = \sum_{j=0}^{P} \alpha_j \frac{\partial \Psi_j(\boldsymbol{\xi})}{\partial \xi_i}, \tag{23}$$

where differentiation of Ψ_j is performed analytically. Dakota computes local sensitivities for each response function R evaluated at uncertain variable means $\langle \boldsymbol{\xi} \rangle$.

D. Numerical setup

The shock-cylinder interaction is studied as a two-dimensional problem with an assumed symmetry plane at the center axis of the cylinder. The simulation domain is shown in Fig. 1.

A convective boundary condition is imposed at the left boundary, at the bottom boundary a symmetry condition is imposed and outflow conditions are used at the right and top boundaries. For reduced computational cost, the fine-grid domain around the region of interest is embedded into a coarser outer domain. The fine-grid domain is discretized by an homogeneous Cartesian grid with 960 cells per cylinder diameter ($D = 0.006$ m) resulting in quadratic cells of size $\Delta_{xy} = 6.25\ \mu$m. This discretization is verified to be sufficient for direct numerical simulations through a grid convergence study in Sec. V. In the coarse-grid domain, hyperbolic grid stretching is applied towards the boundaries. In order to further reduce the computational overhead, a moving reference frame is introduced. The reference frame velocity is chosen such that the cylinder remains within the fine-grid domain during the simulation time of 640 μs. We note that the proper speed of the reference frame requires adjustment for each initial condition and hence varies from sample point to sample point.

The pre-shock quantities are matched to the experiment of Tomkins *et al.*[8] $p_1 = 81060Pa$, $T_1 = 298\,K$ and the post-shock quantities are calculated using the Rankine-Hugoniot conditions. The cylinder is initialized with the upstream face set at the origin, see Fig. 1, and the shock wave is initialized such that it hits the moving cylinder 12 μs after the initialization. The heavy-gas

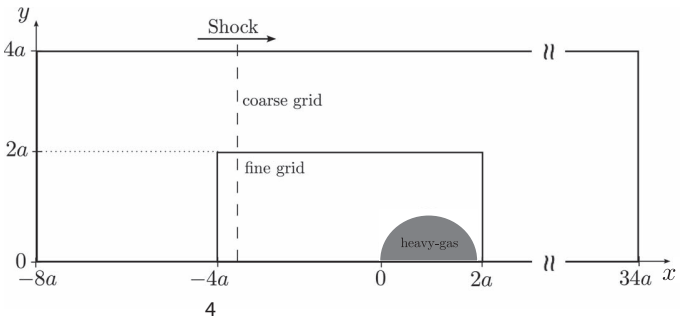

FIG. 1. Schematic of the computational domain for the shock-cylinder interaction simulation. The maximum semi-major axis a equals 3.2 mm.

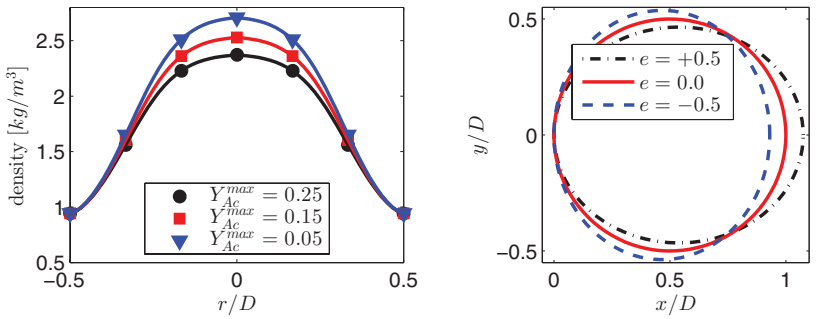

FIG. 2. The density of the cylinder with different acetone concentrations (left). Cross section of the cylinder with different eccentricities e (right). The upstream face of the cylinder is set at the origin for all e.

distribution of the cylinder is matched to the experiment as proposed by Shankar *et al.*,[9]

$$Y_{HG}(r) = \begin{cases} Y_{HG}^{max}\left(1 - \exp\left(\frac{-\left|\left(\frac{|r|}{R_d}-1\right)\pi\right|^{1.54}}{1.0082}\right)\right) & \text{if} |r| \le R_d \\ 0 & \text{else,} \end{cases} \tag{24}$$

where R_d is the radius of the cylinder, $r = \sqrt{(x-x_0)^2 + (y-y_0)^2}$ is the distance to a point (x, y) from the cylinder origin (x_0, y_0), Y_{HG}^{max} is kept constant and equals 0.83. Thus $Y_{Air}(r) = 1 - Y_{HG}(r)$, $Y_{Ac}(r) = Y_{Ac}^{max} Y_{HG}(r)$, and $Y_{SF_6}(r) = (1 - Y_{Ac}^{max}) Y_{HG}(r)$. To take the cylinder deformation into account, R_d in Eq. (24) has to be modified. It is constant and equal to $D/2$ in the case of a circular cylinder, but if the cylinder has an elliptical cross section the radius becomes

$$R_d = \frac{b}{\sqrt{1 - e^2 \cos^2 \phi}}, \tag{25}$$

where a is the semi-major axis, b is the semi-minor axis, and ϕ is the polar angle. Stretching of the cylinder in the x or y direction depends on the sign of the eccentricity e, which is defined as

$$e = \pm \frac{\sqrt{a^2 - b^2}}{a}. \tag{26}$$

The deformed cylinder should have the same volume as the circular cylinder with $D = 0.006$ m, thus $b = \frac{D}{2}\left(1 - e^2\right)^{1/4}$. If $e > 0$ the major axis coincides with the x-axis and

$$\cos^2 \phi = \frac{(x - x_0)^2}{(x - x_0)^2 + (y - y_0)^2}, \tag{27}$$

where x_0 and y_0 are the coordinates of the cylinder origin. If $e < 0$ the major axis is parallel to the y-axis and

$$\cos^2 \phi = \frac{(y - y_0)^2}{(x - x_0)^2 + (y - y_0)^2}. \tag{28}$$

The cross sections of the cylinder for $e = 0.5$, $e = 0.0$, and $e = -0.5$ are shown in Fig. 2.

IV. DEFINITION OF OUTPUT QUANTITIES OF INTEREST

In the following, we define the output quantities of interest:

(i) Geometrical quantities such as the downstream point x_d, the upstream point x_u, the mixing layer length in streamwise direction l_x with $l_x = x_d - x_u$, and the spanwise direction l_y with $l_y = 2y_{max}$, the downstream and the upstream width of the spiral d_d, d_u and the centroid x_c of the deformed cylinder are shown in Fig. 3. The quantities x_d, x_u, and y_{max} are calculated as the extremal points that satisfy $Y_{SF_6} \ge 0.01 \max\{Y_{SF_6}(t)\}$. The ratio of the downstream and the

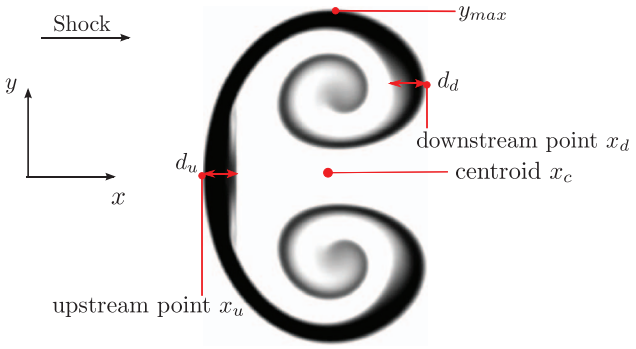

FIG. 3. Geometrical quantities.

upstream roll-up spiral width d_d/d_u can easily be compared to the value found in the experiment of Tomkins *et al.*[8] The experimental quantity is identified by visual inspection of the contour plots of the heavy gas concentration. In the present numerical investigation the ratio d_d/d_u is computed by choosing a threshold for the SF_6 concentration as $Y_{SF_6} \geq 0.1 \max\{Y_{SF_6}(t)\}$. Note that this quantity is well-defined only as long as the heavy-gas region is geometrically similar to Fig. 3. Therefore, this quantity is evaluated only in the time interval 220 μs $\leq t \leq$ 560 μs. The centroid of the heavy-gas region x_c is

$$x_c = \frac{\int x Y_{SF_6} dxdy}{\int Y_{SF_6} dxdy}. \tag{29}$$

(ii) The circulation Γ is defined as the absolute value of the integral of the vorticity

$$\Gamma = \left| \int \omega_z dxdy \right| = \left| \int \left(\frac{\partial v}{\partial x} - \frac{\partial u}{\partial y} \right) dxdy \right|. \tag{30}$$

Note that, due to symmetry, Γ is only computed for the upper half of the heavy-gas region.

(iii) The total mixing rate (TMR) is calculated from the gradient of the mass fraction of SF_6. TMR is defined as the area integral of the scalar mixing rate of SF_6,

$$\text{TMR} = \int D_{SF_6} \nabla Y_{SF_6} \cdot \nabla Y_{SF_6} dxdy, \tag{31}$$

where D_{SF_6} is the effective diffusion coefficient of SF_6, see Appendixes A and B.

(iv) The total molecular mixing fraction (MMF) is defined as

$$\text{MMF} = \frac{\int \langle X_{Air} X_{HG} \rangle \, dx}{\int \langle X_{Air} \rangle \langle X_{HG} \rangle \, dx}. \tag{32}$$

$\langle \cdot \rangle$ indicates spatial averaging in the spanwise direction of the volume fractions X_i. When MMF $= 0$, the four species are completely segregated and when MMF $= 1$, they are completely mixed.

To reduce the computational cost all integral quantities such as Γ, TMR, and MMF are only computed in the mixing region that is defined by $[x_u, x_d] \times [0, y_{max}]$. The time is initialized to zero $t_0 = 0$ μs when the shock first impacts the cylinder. Geometrical quantities that depend on the moving reference frame, e.g., x_u, x_c, x_d, are transformed back to a non-moving frame.

V. RESULTS

A. Grid convergence study

A grid convergence study is performed for $M = 1.2$, $Y_{Ac}^{max} = 0.15$, and $e = 0.0$ on three different grid resolutions with 480, 960, and 1920 cells per cylinder diameter, corresponding to a

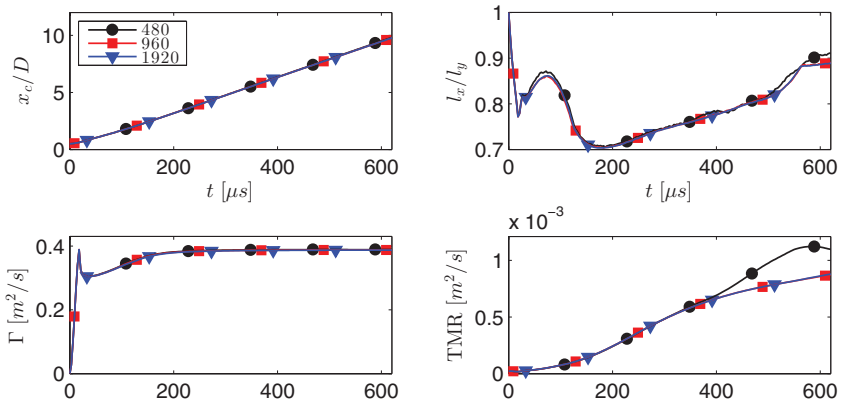

FIG. 4. Grid convergence study for $M = 1.2$, $e = 0.0$, $Y_{Ac} = 0.15$ on three different grid resolutions with 480, 960, and 1920 cells per cylinder diameter.

cell size of 12.5 μm, 6.25 μm, and 3.125 μm in the region of interest. All integral quantities shown in Fig. 4 indicate grid convergence. Results for the medium and the fine grid are indistinguishable. TMR appears to be the most sensitive quantity in terms of grid convergence. On the coarse grid TMR is overpredicted after $t \approx 400$ μs as secondary instabilities are artificially triggered by the reconstruction scheme, see Fig. 5. These secondary instabilities disappear for the two finer grids that resolve the dissipative scales. The normalized position of the heavy-gas-region centroid x_c/D as well as the circulation Γ are unaffected by grid refinement. Fig. 5 shows contour plots of the SF_6 mass fraction, which confirm a grid convergence between the medium and the high-resolution grid. From this observation we conclude that results obtained on the medium-resolution grid with 960 cells per D ($\Delta_{xy} = 6.25$ μm) are converged and therefore, qualify as direct numerical simulation results. Shankar *et al.*[9] also observed a trend towards a grid converged solution on grids with 480 cells per D and 960 cells per D with small differences only in the predicted values of TMR at times beyond $t = 600\,\mu$s when small-scale flow features are clearly developed. Thus, the medium-resolution grid is used for the 125 simulations needed for the uncertainty quantification.

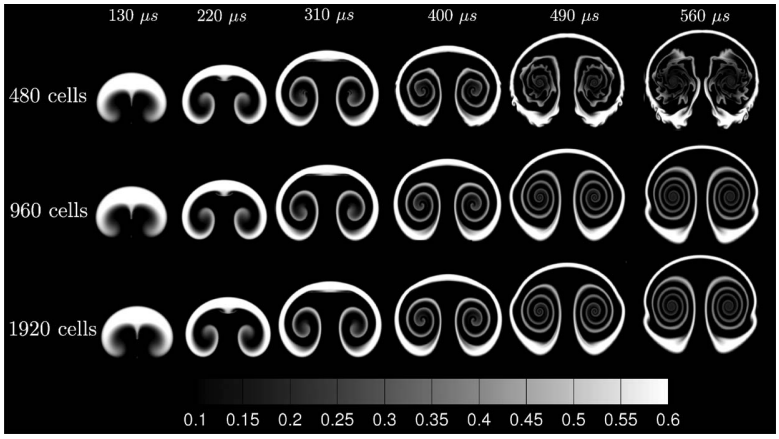

FIG. 5. Contour plots of SF_6 mass fraction Y_{SF_6} for $M = 1.2$, $Y_{Ac}^{max} = 0.15$, and $e = 0.0$ on three different grid resolutions with 480, 960, and 1920 cells per cylinder diameter.

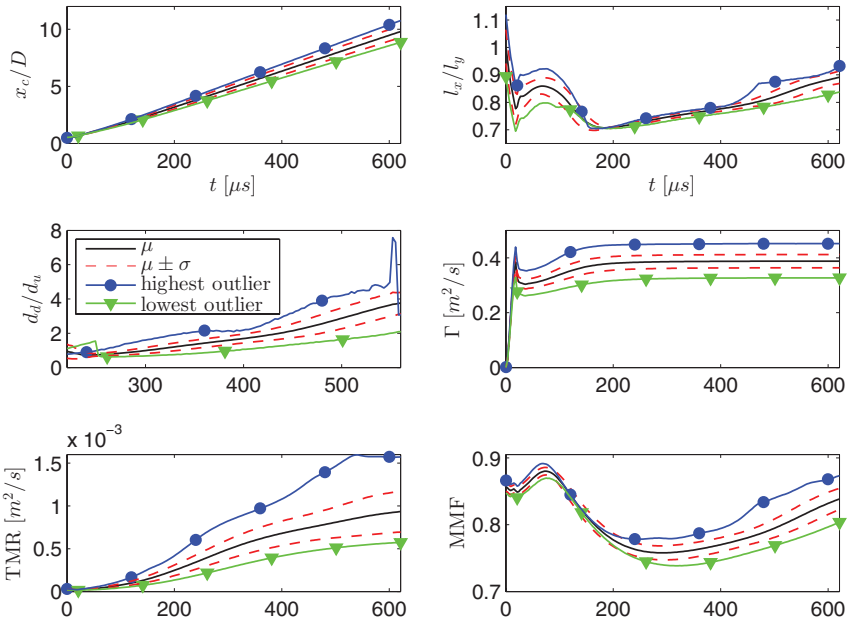

FIG. 6. Time evolution of the output uncertainties in terms of mean value, standard deviation, and outliers.

B. Time evolution of the output uncertainty

1. Mean value, standard deviation, and outliers

The mean values of the output QoI and their corresponding standard deviations are shown in Fig. 6. Additionally, the minimum and maximum outliers of each output quantity are recorded and shown in Fig. 6. The outliers are simulations that maximize the deviation from the mean value averaged over the entire simulation time and are found by

$$\langle Z_i \rangle = \frac{1}{n-s} \sum_{j=s}^{n} \frac{R_i(t_j) - \mu_i(t_j)}{\mu_i(t_j)}, \tag{33}$$

where R_i is the output quantity, μ_i is its mean value, t_j is the time at the time step j, n is the overall number of time steps, and s is the offset ($\approx 15\ \mu$s) from time $t = 0$ to avoid zero values in the denominator of Eq. (33). The simulation with a maximum $\langle Z_i \rangle$ is the highest outlier and the simulation with a minimum $\langle Z_i \rangle$ is the lowest outlier. Note that the outliers do not have to be either larger or smaller than the mean value throughout the entire simulation time. The standard deviation of the location of the centroid x_c/D of the cylinder grows approximately linearly in time. It is about $1.5D$ at the final time $t = 640\ \mu$s. The minimum and maximum outliers have the same deviation from the mean value, suggesting a linear dependence between input and output uncertainty.

The mixing region l_x contracts in streamwise direction until the shock reaches the downstream point of the cylinder, whereas l_y remains nearly constant, i.e., l_x/l_y decreases. After the shock has left the mixing region both l_x and l_y grow, see Fig. 9. At late times l_x grows faster than l_y and l_x/l_y increases. l_x/l_y reaches its global minimum of 0.71 at $t \approx 200\ \mu$s. At this time also the outliers collapse and the standard deviation reduces to zero. Therefore, with respect to these QoI the numerical results are independent of the initial conditions within the uncertainty bounds of the input parameters. In the time interval between 200 and 500 μs the ratio l_x/l_y depends only weakly on the initial uncertainty parameters. Note that the initial standard deviation is not zero since e affects the initial shape of the cylinder before shock impact.

The ratio d_d/d_u can be measured by visual inspection of the experimental contour plots, see Figures 3 and 9. In the experiment, it is $d_d/d_u < 1$ and reaches its global maximum $d_d/d_u \approx 1$ at $t = 560\ \mu$s. In the present numerical investigation it starts to be larger than unity for $t > 390\ \mu$s,

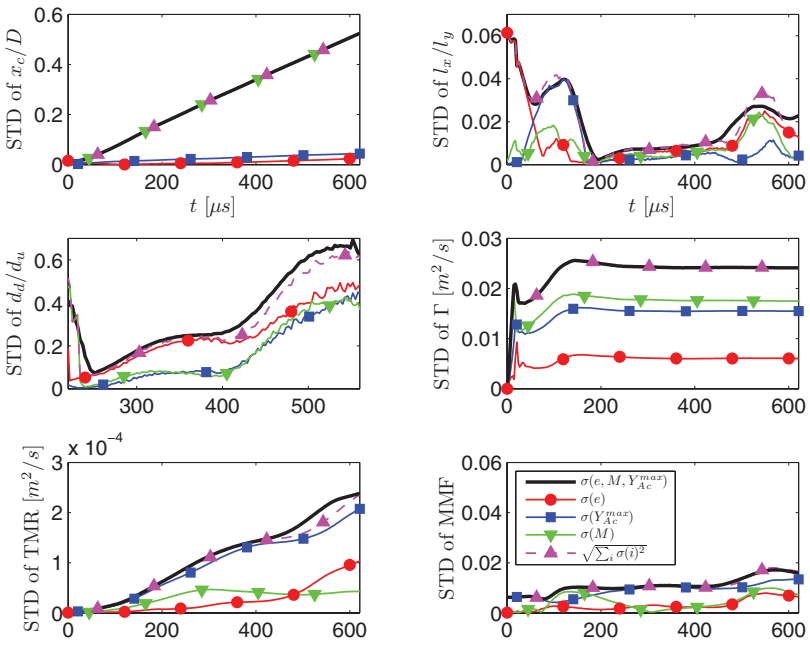

FIG. 7. The individual standard deviations $\sigma(e)$, $\sigma(M)$, and $\sigma(Y_{Ac}^{max})$, the multivariate standard deviation $\sigma(e, Y_{Ac}^{max}, M)$ and the multivariate standard deviation for uncorrelated random variables $\sqrt{\sum_i \sigma(i)^2}$.

independently of the initial conditions. Even the outlier shows a value of $d_d/d_u \approx 1.8$ at $t \approx 540$ μs. At earlier times $t = 220$ μs we estimate the experimental ratio as 0.67, see Fig. 9, whereas the mean value in the present simulation is $d_d/d_u = 0.69$. The standard deviation shows a local minimum at $t = 255$ μs where σ is almost zero. Therefore, d_d/d_u is independent of the input parameters at this time.

The total circulation Γ grows linearly as long as the shock wave propagates within the heavy-gas region. Γ decreases as the shock wave reaches the downstream face of the heavy-gas region due to reflected rarefaction waves and then levels out to a mean value of 0.39 m^2/s for the rest of the simulation time. The same value was obtained for the total circulation in Shankar *et al.*[23] The standard deviation of Γ is almost zero as long as the shock is within the heavy-gas region but then grows up to a constant value 0.024 m^2/s.

TMR seems to be the quantity that is the most sensitive to changes in the initial conditions. The uncertainty range of the TMR defined by the outliers spreads over more than 120% of the mean value at the final time. The standard deviation increases considerably with time and reaches more than 20% of the TMR mean value at the end of the simulation time. Accordingly, material mixing is very sensitive to initial condition variations and a quantitative match with the experimental data is very challenging.

Another mixing measure is the MMF. It grows after the shock has left the cylinder, but then starts to drop again at around $t = 80$ μs. This drop is caused by the growth of the mixing-layer width that is used as averaging region for the MMF calculation. After $t = 300$ μs material mixing in the mixing layer dominates over the growth of the mixing layer and thus MMF increases again. The standard deviation of MMF slightly grows in time and reaches its global maximum of 0.017 at the end of the simulation, see Fig. 7.

The input parameters for the outliers are given in Table I. Because of the numerical integration of Eq. (20) for the uncertainty analysis, the numerical domain of the input parameters differ slightly from the analytical domain

$$M_{min}^{num} = 1.1819, \quad M_{max}^{num} = 1.2181 \tag{34}$$

TABLE I. The input parameters of the outliers.

Output parameter	Maximum	Minimum
x_c/D	$e = -0.4531$ $Y_{Ac}^{max} = 0.2406$ $M = 1.2181$	$e = 0.4531$ $Y_{Ac}^{max} = 0.0594$ $M = 1.1819$
l_x/l_y	$e = 0.4531$ $Y_{Ac}^{max} = 0.2406$ $M = 1.2181$	$e = -0.4531$ $Y_{Ac}^{max} = 0.0962$ $M = 1.1819$
d_d/d_u, Γ[m^2/s], TMR [m^2/s], MMF	$e = 0.4531$ $Y_{Ac}^{max} = 0.0594$ $M = 1.2181$	$e = -0.4531$ $Y_{Ac}^{max} = 0.2406$ $M = 1.1819$

$$e_{min}^{num} = -0.4531, \quad e_{max}^{num} = 0.4531 \tag{35}$$

$$\left(Y_{Ac}^{max}\right)_{min}^{num} = 0.0594, \quad \left(Y_{Ac}^{max}\right)_{max}^{num} = 0.2406. \tag{36}$$

2. Standard deviation and single uncertain-parameter variation

It is useful to study the effect of the input uncertainties separately to assess which one has a dominant effect on a particular output quantity. Fig. 7 gives the computed standard deviations for $\sigma(e)$, $\sigma(M)$, and $\sigma(Y_{Ac}^{max})$. Furthermore, it shows the multivariate standard deviation $\sigma(e, M, Y_{Ac}^{max})$ and $\sqrt{\sum_i \sigma(i)^2}$. The latter is the exact multivariate standard deviation for uncorrelated random variables characterized by vanishing covariance. The weak correlation of the three uncertainty parameters is reflected by the fact $\sqrt{\sum_i \sigma(i)^2} \approx \sigma(e, M, Y_{Ac}^{max})$ during the entire simulation time $0\,\mu\text{s} \le t \le 640\,\mu\text{s}$.

The standard deviation of x_c/D is largely dominated by the variation of the Mach number, i.e., $\sigma(e, M, Y_{Ac}^{max}) \approx \sigma(M)$. Shankar *et al.*[9] reported the potential influence of a contamination of the heavy-gas region with acetone on the location of the centroid. However, compared to the Mach number, Y_{Ac} has only a marginal effect on the cylinder location.

The eccentricity e defines the initial cylinder shape and thus strongly affects the standard deviation of l_x/l_y in the beginning. At later times the influence of e on the standard deviation is weaker. Between 200 μs and 500 μs, l_x/l_y is mostly unaffected by the variation of the input uncertain parameters. However, at later times the effect of eccentricity e and Mach number M again dominate the time evolution of the l_x/l_y uncertainty.

The ratio d_d/d_u is only affected at later times by a variation of the input parameters and the three uncertainty parameters then seem to have a comparable influence.

The standard deviation of Γ is equally affected by M and Y_{Ac}^{max}, whereas e has only minor effects. Because M and Y_{Ac}^{max} directly affect $|\nabla p|$ and $|\nabla \rho|$, they dominate the baroclinic vorticity production $D\omega/Dt \approx (\nabla\rho \times \nabla p)/\rho^2$ and thus the time evolution of Γ. Changes in the misalignment of ∇p and $\nabla \rho$ due to the eccentricity, however, only weakly affect the standard deviation of the circulation.

The mixing measures TMR and MMF are mostly affected by variations in Y_{Ac}^{max}. An uncertainty in Y_{Ac}^{max} directly changes ∇Y_{SF_6}, which is used for the computation of the TMR, see Eq. (31). On the other hand, it also changes $\nabla\rho$ leading to a decreased baroclinic vorticity deposition as Y_{Ac} is increased, $\nabla\rho \propto 1/Y_{Ac}^{max}$. For the same reason, Y_{Ac}^{max} is responsible for a large portion of the uncertainty in MMF. This is consistent with the findings of Shankar *et al.*[9] who observed a decrease of TMR as Y_{Ac}^{max} increases.

3. Local sensitivities

Local sensitivities $\partial R/\partial \xi_j\big|_{\langle \boldsymbol{\xi} \rangle}$ for each response function R are evaluated at uncertainty variable means $\langle \boldsymbol{\xi} \rangle$. The local sensitivities are shown in Fig. 8. Interpretation of $\partial R/\partial \xi_j\big|_{\langle \boldsymbol{\xi} \rangle}$ should be

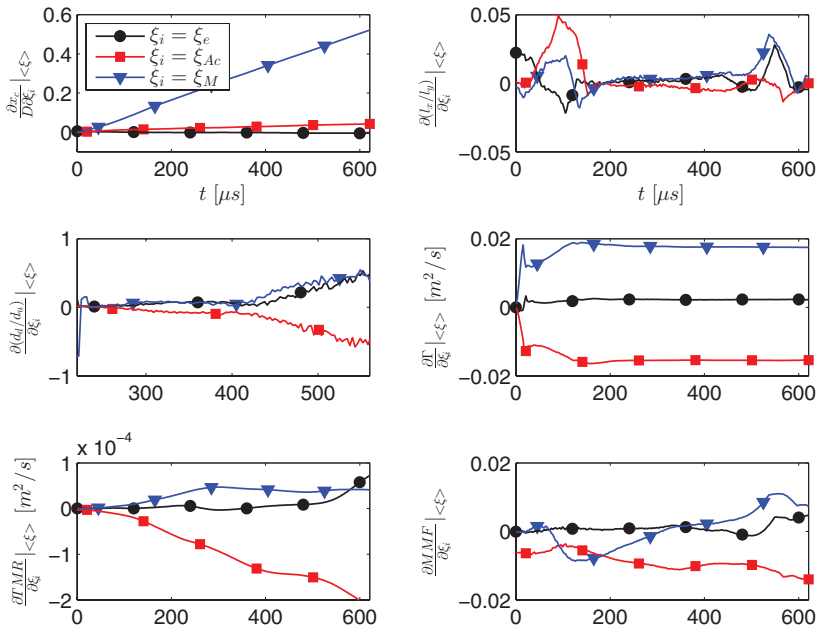

FIG. 8. The local sensitivities of the output quantities evaluated at the uncertain variable means.

done with caution, because it is a local quantity and does not reflect the global system behavior, unlike σ. Therefore, the local sensitivity yields only a tendency (increasing or decreasing) of the response function (output uncertainty). Note that, in order to avoid different dimensions of the derivatives, standardized random variables ξ_e, ξ_{Ac}, and ξ_M are used for the computation of the local sensitivities.

An increase of M causes an increase of x_c/D, whereas an increase of e and Y_{Ac}^{max} does not considerably affect the location of the centroid. It is remarkable that the derivative $\partial\left(l_x/l_y\right)/\partial\xi_i|_{\langle\boldsymbol{\xi}\rangle}$ changes sign throughout the simulation. At early times the uncertainty parameters ξ_i cause the output parameter to grow, whereas at later times the same ξ_i can have the inverse effect on the output parameters.

Between $220\,\mu$s and $400\,\mu$s the derivatives of the mean values $\partial\left(l_x/l_y\right)/\partial\xi_i|_{\langle\boldsymbol{\xi}\rangle}$ and $\partial\left(d_d/d_u\right)/\partial\xi_i|_{\langle\boldsymbol{\xi}\rangle}$ are close to zero, which means that small changes in the input parameters will not result in a significant change of l_x/l_y and d_d/d_u. Nevertheless, their standard deviation is not equal to zero, which means that larger changes in the input parameters indeed affect l_x/l_y and d_d/d_u. The circulation is most sensitive to the Mach number and the acetone concentration because of $\nabla p \propto M$ and $\nabla\rho \propto 1/Y_{Ac}^{max}$. Stretching the cylinder in the streamwise direction only slightly contributes to a growing Γ.

The Mach number and the acetone concentration also dominate the material mixing as can be seen from the local sensitivities of TMR and MMF. The mixing process is enhanced by larger M, but damped as the acetone concentration increases. The effect of the Mach number on the MMF, however, drastically changes with time and reverses its sign at late times. Changes of the cylinder shape appear to be more important for the local sensitivities of TMR and MMF at very late times.

C. Best fit to experiment

In addition to the previous uncertainty analysis a numerical best fit to the experiment of Tomkins *et al.*[8] is determined by solving an optimization problem with the ratio of the downstream and upstream roll-up spiral width d_d/d_u as objective function. This leads to an optimal parameter set $M \approx 1.18$, $Y_{Ac}^{max} \approx 0.25$, and $e \approx -0.5$ that minimizes the difference between numerical and

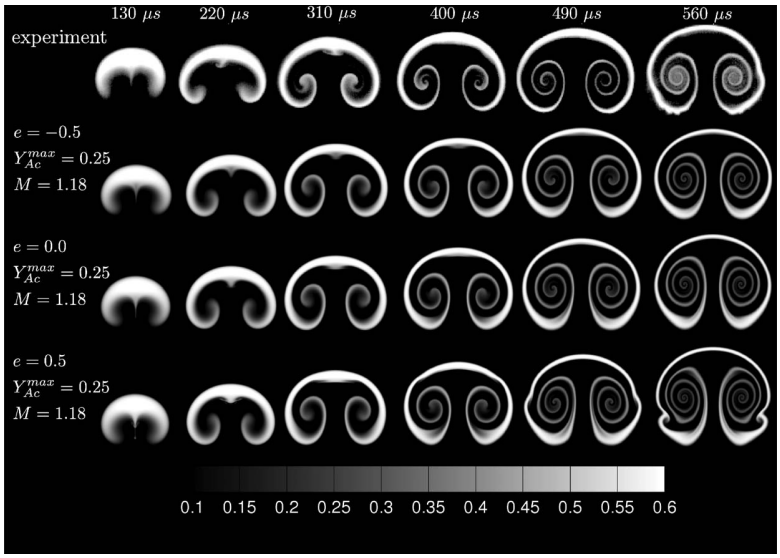

FIG. 9. Contour plots of SF_6 mass fraction Y_{SF_6} with $M = 1.18$, $Y_{Ac}^{max} = 0.25$, and $e = -0.5$ (second row) compared to the experimental results (first row) by Tomkins *et al.*[8] The numerical results for $e = 0.0$ (third row) and $e = 0.5$ (fourth row) are also shown.

experimental results. The minimal value of d_d/d_u that we found in our simulations, however, is larger than the experimental value and thus the optimal parameters are found on the uncertainty-domain boundaries.

The contour plots of Y_{SF_6} are shown in Fig. 9 for six consecutive time instants. The present numerical results (second row) are in excellent agreement with the experimental data (first row). This suggests that the true Mach number slightly deviates from the nominal value and that the experimental contamination of the heavy gas cylinder with acetone was in fact larger than the estimated 20% by Shankar *et al.*[9] A negative eccentricity implies stretching of the cylinder in the spanwise direction, however, given the experimental initial condition of Tomkins *et al.*, a streamwise stretching of the cylinder could be expected. Fig. 9 shows therefore also the contour plots for $e = 0$ and $e = 0.5$. Note the occurrence of small kinks on the outer part of the distorted heavy-gas region as the eccentricity is increased. Even though similar kinks are seen in the experiment, the time evolution of the instability seems to be less well captured than in the case of $e = -0.5$.

From Sec. V B, it can be concluded that the TMR is the most sensitive quantity with respect to the variation of the uncertainty parameters. Unfortunately, the experimental data of Tomkins *et al.*[8] are given in arbitrary units.[24] Shankar *et al.*[9] had to use a scaling factor[24] in order to reproduce the experimental TMR value quantitatively. Rather than using an arbitrary scaling factor we resolve the scaling discrepancy by determining the optimum scaling factor ζ by least-squares minimization from the best fit simulation. The optimum scaling factor is calculated to $\zeta = 0.7875 \times 10^6$ leading to the scaled numerical TMR value

$$\mathrm{TMR}_{scaled} = \zeta \frac{2}{Y_{HG}^{max\,2}} \int D_{SF_6} \nabla Y_{SF_6} \cdot \nabla Y_{SF_6} dx dy. \tag{37}$$

Note, due to symmetry, TMR is only computed for the upper half of the heavy-gas region and therefore has to be multiplied by a factor of 2.

The temporal evolution of the experimental and the scaled numerical TMR is shown in Fig. 10. Both are in good qualitative agreement, which is consistent with the findings of Shankar *et al.*[9]

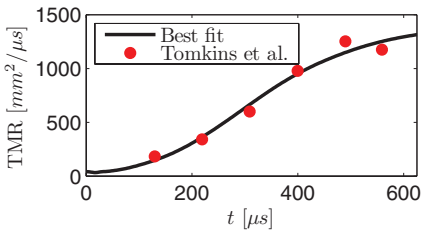

FIG. 10. Temporal evolution of scaled numerical and experimental TMR values.

VI. CONCLUSION

Initial-data uncertainties of a shock accelerated heavy-gas cylinder have been investigated by a set of 125 two-dimensional well-resolved direct numerical simulations. The initial data of our investigation were matched to previous experimental and numerical investigations. Three different main sources of initial-data uncertainties were investigated, (i) shock Mach number M, (ii) contamination of the SF_6 region with acetone Y_{Ac}^{max}, and (iii) initial deviations of the heavy-gas region from a perfect cylindrical shape e. A polynomial chaos expansion was used to propagate the initial-data uncertainties to the output QoI. The numerical simulations were performed with a high-resolution compressible multicomponent flow simulation model involving four species.

The geometrical quantities, i.e., the heavy-gas region position and the cross section, appear to be less affected by the variation of the initial data than the mixing quantities TMR and molecular mixing fraction. For the evolution of the heavy-gas region, all three uncertainty parameters are equally important. However, the effect of the eccentricity appears to be limited to the mixing layer width ratio l_x/l_y and d_d/d_u.

The calculation of the local sensitivities of the output QoI reveals that the effect of the input quantities on certain output quantities may change over time. Our investigation suggests that the mixing quantities, especially TMR, are highly sensitive to changes in the Mach number and acetone concentration. The fact that the experimental acetone contamination of the cylinder is largely unknown along with a given uncertainty in the Mach number renders quantitative comparisons of the TMR with experimental data very challenging.

Within the uncertainty domain a set of M, Y_{Ac}^{max}, and e was determined by solving an optimization problem with the downstream and upstream roll-up spiral width d_d/d_u as the objective function. The numerical results for this parameter set are in excellent agreement with the experiment and suggest that the measured Mach number and the estimated contamination of SF_6 with acetone are strongly biased. For an accurate numerical reproduction of the experiment it is crucial that the Mach number and the acetone concentration in the heavy-gas region are known precisely. Finally, we note that the present investigation is limited to two-dimensional simulations. Certainly relevant three-dimensional effects are not within the scope of the current investigation, but will be addressed in subsequent work.

ACKNOWLEDGMENTS

We want to thank Sebastian Eberhardt, TUM for his enduring commitment for the development of the multicomponent flow solver INCA. The authors gratefully acknowledge the Gauss Centre for Supercomputing e.V. (www.gauss-centre.eu) for providing computing time on the GCS Supercomputer SuperMUC at Leibniz Supercomputing Centre (LRZ, www.lrz.de). V.K.T. gratefully acknowledges the support of the TUM Graduate School.

APPENDIX A: MULTICOMPONENT MIXING RULES

The specific gas constant of species i is found by

$$R_i = \frac{R_{univ}}{M_i} \tag{A1}$$

with the corresponding specific heat coefficients

$$c_{p,i} = \frac{\gamma_i}{\gamma_i - 1} R_i, \quad c_{v,i} = \frac{1}{\gamma_i - 1} R_i. \tag{A2}$$

Here γ_i is the ratio of specific heats of species i. The ratio of specific heats of the mixture $\overline{\gamma}$ is then

$$\overline{\gamma} = \frac{\overline{c_p}}{\overline{c_p} - \overline{R}} \tag{A3}$$

with

$$\overline{c_p} = \sum_i^N Y_i c_{p,i}. \tag{A4}$$

Y_i is the mass fraction of species i and $\overline{R}$ is the specific gas constant of the mixture with $\overline{R} = \frac{R_{univ}}{\overline{M}}$. The molar mass of the mixture is given by

$$\overline{M} = \left(\sum_i^N \frac{Y_i}{M_i} \right)^{-1}. \tag{A5}$$

For the gas mixture Dalton's law $p = \sum_i p_i$ shall be valid with $p_i = \rho R_i T$. The viscosity $\overline{\mu}$ and the heat conductivity coefficient $\overline{\kappa}$ of the mixture is calculated from[25]

$$\overline{\mu} = \frac{\sum_{i=1}^N \mu_i Y_i / M_i^{1/2}}{\sum_{i=1}^N Y_i / M_i^{1/2}}, \quad \overline{\kappa} = \frac{\sum_{i=1}^N \kappa_i Y_i / M_i^{1/2}}{\sum_{i=1}^N Y_i / M_i^{1/2}}. \tag{A6}$$

The effective binary diffusion coefficients (diffusion of species i into all other species) are approximated as[26]

$$D_i = (1 - X_i) \left(\sum_{i \neq j}^N \frac{X_j}{D_{ij}} \right)^{-1}, \tag{A7}$$

where X_i is the mole fraction of species i. Equation (A7) ensures that the inter-species diffusion fluxes balance to zero.

APPENDIX B: MOLECULAR MIXING RULES

The viscosity coefficient of a pure gas is given by[27]

$$\mu = 2.6693 \times 10^{-6} \frac{\sqrt{MT}}{\Omega_\mu \sigma^2}, \tag{B1}$$

where σ is the collision diameter and Ω_μ is the collision integral

$$\Omega_\mu = A(T^*)^B + C \exp\{DT^*\} + E \exp\{FT^*\}, \tag{B2}$$

where $T_{ij}^* = T / T_{\epsilon_{ij}}$ and $A = 1.16145$, $B = -0.14874$, $C = 0.52487$, $D = -0.7732$, $E = 2.16178$, and $F = -2.43787$. $T_\epsilon = \epsilon / k$ is the effective temperature characteristic of the force potential function and k is the Boltzmann constant. The mass diffusion coefficient of a binary mixture can be calculated from the empirical law[25]

$$D_{ij} = \frac{0.0266}{\Omega_D} \frac{T^{3/2}}{p \sqrt{M_{ij}} \sigma_{ij}^2} \tag{B3}$$

with the collision integral for diffusion

$$\Omega_D = A(T_{ij}^*)^B + C \exp\{DT_{ij}^*\} + E \exp\{FT_{ij}^*\} + G \exp\{HT_{ij}^*\}, \tag{B4}$$

TABLE II. Molecular properties of nitrogen, oxygen, SF_6, and acetone.

Property	Nitrogen	Oxygen	SF_6	Acetone
$(\epsilon/k)_i$	82.0	102.6	212.0	458.0
σ_i	3.738	3.48	5.199	4.599
M_i[g/mol]	28.0140	31.9990	146.0570	58.0805
γ_i	1.4	1.4	1.1	1.1

where $T^*_{ij} = T/T_{\epsilon_{ij}}$ and $A = 1.06036$, $B = -0.1561$, $C = 0.19300$, $D = -0.47635$, $E = 1.03587$, $F = -1.52996$, $G = 1.76474$, $H = -3.89411$, and

$$\begin{aligned} M_{ij} &= \frac{2}{\frac{1}{M_i} + \frac{1}{M_j}} \\ \sigma_{ij} &= \frac{\sigma_i + \sigma_j}{2} \\ T_{\epsilon_{ij}} &= \sqrt{\left(\frac{\epsilon}{k}\right)_i \left(\frac{\epsilon}{k}\right)_j}. \end{aligned} \tag{B5}$$

The molecular properties of all species in the present study are given in Table II.

[1] R. D. Richtmyer, "Taylor instability in shock acceleration of compressible fluids," Commun. Pure Appl. Math. **13**, 297 (1960).
[2] E. E. Meshkov, "Instability of the interface of two gases accelerated by a shock wave," Fluid Dyn. **4**, 101 (1969).
[3] D. Arnett, "The role of mixing in astrophysics," Appl. J. Suppl. **127**, 213 (2000).
[4] P. Amendt, J. D. Colvin, R. E. Tipton, D. E. Hinkel, and M. J. Edwards, "Indirect-drive noncryogenic double-shell ignition targets for the National Ignition Facility: Design and analysis," Phys. Plasmas **9**, 2221 (2002).
[5] J. Yang, T. Kubota, and E. E. Zukoski, "Applications of shock-induced mixing to supersonic combustion," AIAA J. **31**, 854 (1993).
[6] J.-F. Haas and B. Sturtevant, "Interaction of weak shock waves with cylindrical and spherical gas inhomogeneities," J. Fluid Mech. **181**, 41 (1987).
[7] M. A. Jones and J. W. Jacobs, "A membraneless experiment for the study of Richtmyer-Meshkov instability of a shock-accelerated gas interface," Phys. Fluids **9**, 3078 (1997).
[8] C. Tomkins, S. Kumar, G. Orlicz, and K. Prestridge, "An experimental investigation of mixing mechanisms in shock-accelerated flow," J. Fluid Mech. **611**, 131 (2008).
[9] S. K. Shankar, S. Kawai, and S. K. Lele, "Two-dimensional viscous flow simulation of a shock accelerated heavy gas cylinder," Phys. Fluids **23**, 024102 (2011).
[10] B. D. Collins and J. W. Jacobs, "PLIF flow visualization and measurements of the Richtmyer–Meshkov instability of an air/SF6 interface," J. Fluid Mech. **464**, 113 (2002).
[11] S. Balasubramanian, private communication (2012).
[12] S. Balasubramanian, G. C. Orlicz, K. P. Prestridge, and B. J. Balakumar, "Experimental study of initial condition dependence on Richtmyer-Meshkov instability in the presence of reshock," Phys. Fluids **24**, 034103 (2012).
[13] A. W. Cook, "Enthalpy diffusion in multicomponent flows," Phys. Fluids **21**, 055109 (2009).
[14] B. Larrouturou and L. Fezoui, "On the equations of multi-component perfect or real gas inviscid flow," Lect. Notes Math. **1402**, 69 (1989).
[15] R. P. Fedkiw, B. Merriman, and S. Osher, "High accuracy numerical methods for thermally perfect gas flows with chemistry," J. Comput. Phys. **132**, 175 (1997).
[16] P. L. Roe, "Approximate Riemann solvers, parameter, and difference schemes," J. Comput. Phys. **43**, 357 (1981).
[17] X. Y. Hu, Q. Wang, and N. A. Adams, "An adaptive central-upwind weighted essentially non-oscillatory scheme," J. Comput. Phys. **229**, 8952 (2010).
[18] E. F. Toro, *Riemann Solvers and Numerical Methods for Fluid Dynamics* (Springer, Berlin, 1999).
[19] S. Gottlieb and C.-W. Shu, "Total variation diminishing Runge-Kutta schemes," Math. Comput. **67**, 73 (1998).
[20] V. K. Tritschler, X. Y. Hu, S. Hickel, and N. A. Adams, "Numerical simulation of a Richtmyer-Meshkov instability with an adaptive central-upwind 6th-order WENO scheme," Phys. Scr. **T155**, 014016 (2013).
[21] V. K. Tritschler, S. Hickel, X. Y. Hu, and N. A. Adams, "On the Kolmogorov inertial subrange developing from Richtmyer-Meshkov instability," Phys. Fluids **25**, 071701 (2013).
[22] B. M. Adams, M. S. Ebeida, M. S. Eldred, J. D. Jakeman, L. P. Swiler, W. J. Bohnhoff, K. R. Dalbey, J. P. Eddy, K. T. Hu, and D. M. Vigil, "DAKOTA a multilevel parallel object-oriented framework for design optimization, parameter estimation, uncertainty quantification, and sensitivity analysis," Technical Report SAND2011-9106 (Sandia National Laboratories, 2011), see http://dakota.sandia.gov/docs/dakota/3.0/Users3.0.pdf.
[23] S. K. Shankar, S. Kawai, and S. K. Lele, "Numerical simulation of multicomponent shock accelerated flows and mixing using localized artificial diffusivity method," AIAA Paper No. 2010-352, 2010.

[24] S. K. Shankar, private communication (2013).
[25] R. C. Reid, J. M. Pransuitz, and B. E. Poling, *The Properties of Gases and Liquids* (McGraw-Hill, New York, 1987).
[26] J. D. Ramshaw, "Self-consistent effective binary diffusion in multicomponent gas mixtures," J. Non-Equilib. Thermodyn. **15**, 295 (1990).
[27] S. Chapman and T. G. Cowling, *The Mathematical Theory of Non- Uniform Gases: An Account of the Kinetic Theory of Viscosity* (Cambridge University Press, Cambridge, 1990).

J. Fluid Mech. (2014), *vol.* 755, *pp.* 429–462.
doi:10.1017/jfm.2014.436

On the Richtmyer–Meshkov instability evolving from a deterministic multimode planar interface

V. K. Tritschler[1,2,†], B. J. Olson[3], S. K. Lele[2], S. Hickel[1], X. Y. Hu[1] and N. A. Adams[1]

[1]Institute of Aerodynamics and Fluid Mechanics, Technische Universität München, 85747 Garching, Germany

[2]Department of Aeronautics and Astronautics, Stanford University, Stanford, CA 94305, USA

[3]Lawrence Livermore National Laboratory, Livermore, CA 94550, USA

(Received 6 February 2014; revised 21 July 2014; accepted 23 July 2014)

We investigate the shock-induced turbulent mixing between a light and a heavy gas, where a Richtmyer–Meshkov instability (RMI) is initiated by a shock wave with Mach number $Ma = 1.5$. The prescribed initial conditions define a deterministic multimode interface perturbation between the gases, which can be imposed exactly for different simulation codes and resolutions to allow for quantitative comparison. Well-resolved large-eddy simulations are performed using two different and independently developed numerical methods with the objective of assessing turbulence structures, prediction uncertainties and convergence behaviour. The two numerical methods differ fundamentally with respect to the employed subgrid-scale regularisation, each representing state-of-the-art approaches to RMI. Unlike previous studies, the focus of the present investigation is to quantify the uncertainties introduced by the numerical method, as there is strong evidence that subgrid-scale regularisation and truncation errors may have a significant effect on the linear and nonlinear stages of the RMI evolution. Fourier diagnostics reveal that the larger energy-containing scales converge rapidly with increasing mesh resolution and thus are in excellent agreement for the two numerical methods. Spectra of gradient-dependent quantities, such as enstrophy and scalar dissipation rate, show stronger dependences on the small-scale flow field structures as a consequence of truncation error effects, which for one numerical method are dominantly dissipative and for the other dominantly dispersive. Additionally, the study reveals details of various stages of RMI, as the flow transitions from large-scale nonlinear entrainment to fully developed turbulent mixing. The growth rates of the mixing zone widths as obtained by the two numerical methods are $\sim t^{7/12}$ before re-shock and $\sim(t - t_0)^{2/7}$ long after re-shock. The decay rate of turbulence kinetic energy is consistently $\sim(t - t_0)^{-10/7}$ at late times, where the molecular mixing fraction approaches an asymptotic limit $\Theta \approx 0.85$. The anisotropy measure $\langle a \rangle_{xyz}$ approaches an asymptotic limit of $\approx$0.04, implying that no full recovery of isotropy within the mixing zone is obtained, even after re-shock. Spectra of density, turbulence kinetic energy, scalar dissipation rate and enstrophy are presented and show excellent agreement for the resolved scales. The probability density function of the heavy-gas mass fraction and vorticity reveal that the light–heavy gas composition within the mixing zone is accurately predicted, whereas it is more difficult to capture the long-term behaviour of the vorticity.

Key words: shock waves, turbulent mixing

† Email address for correspondence: volker.tritschler@aer.mw.tum.de

1. Introduction

The Richtmyer–Meshkov instability (Richtmyer 1960; Meshkov 1969) is a hydrodynamic instability that occurs at the interface separating two fluids of different densities. It shows similarities with the Rayleigh–Taylor instability (Rayleigh 1883; Taylor 1950), where initial perturbations at the interface grow and eventually evolve into a turbulent flow field through the transfer of potential to kinetic energy. In the limit of an impulsive acceleration of the interface, e.g. by a shock wave, the instability is referred to as a Richtmyer–Meshkov instability (RMI). In RMI, baroclinic vorticity production at the interface is caused by the misalignment of the pressure gradient (∇p) associated with the shock wave and the density gradient ($\nabla \rho$) of the material interface. The baroclinic vorticity production term $(\nabla \rho \times \nabla p)/\rho^2$ is the initial driving force of RMI. See Zabusky (1999) and Brouillette (2002) for comprehensive reviews.

RMI occurs on enormous scales in astrophysics (Arnett *et al.* 1989; Arnett 2000; Almgren *et al.* 2006), on intermediate scales in combustion (Yang, Kubota & Zukoski 1993; Khokhlov, Oran & Thomas 1999) and on very small scales in inertial confinement fusion (Lindl, McCrory & Campbell 1992; Taccetti *et al.* 2005; Aglitskiy *et al.* 2010). Owing to the fast time scales associated with RMI, laboratory experimental measurements have difficulties in characterising quantitatively initial perturbations of the material interface and capturing the evolution of the mixing zone. General insight into the flow physics of RMI relies to a considerable extent on numerical investigations, where large-eddy simulations (LES) have become an accepted tool during the past decade.

Hill, Pantano & Pullin (2006) performed a rigorous numerical investigation of RMI with re-shock. The authors used an improved version of the tuned centred difference–weighted essentially non-oscillatory (TCD-WENO) hybrid method of Hill & Pullin (2004). The method employs a switch to blend explicitly between a TCD stencil in smooth flow regions and a WENO shock-capturing stencil at discontinuities. The TCD-WENO hybrid method is used together with the stretched-vortex model (Pullin 2000; Kosović, Pullin & Samtaney 2002) for explicitly modelling the subgrid interaction terms. This approach was also used by Lombardini *et al.* (2011) to study systematically the impact of the Atwood number for a canonical three-dimensional numerical set-up, and for LES of single-shock (i.e. without re-shock) RMI (Lombardini, Pullin & Meiron 2012).

Thornber *et al.* (2010) studied the influence of different three-dimensional broad- and narrow-band multimode initial conditions on the growth rate of a turbulent multicomponent mixing zone developing from RMI. In a later study (Thornber *et al.* 2011), the same authors presented a numerical study of a re-shocked turbulent mixing zone, and extended the theory of Mikaelian and Youngs to predict the behaviour of a multicomponent mixing zone before and after re-shock (cf. Mikaelian 1989; Thornber *et al.* 2010). They used an implicit LES (Drikakis 2003; Thornber *et al.* 2008; Drikakis *et al.* 2009) approach based on a finite-volume Godunov-type method to solve the Euler equations with the same specific heat ratio for both fluids.

In a recent investigation, Weber, Cook & Bonazza (2013) derived a growth-rate model for the single-shock RMI based on the net mass flux through the centre plane of the mixing zone. Here, the compressible Navier–Stokes equations were solved by a tenth-order compact difference scheme for spatial differentiation. Artificial grid-dependent fluid properties, proposed by Cook (2007), were used for shock and material-interface capturing as well as for subgrid-scale modelling.

Grid-resolution-independent statistical quantities of the single-shock RMI were presented by Tritschler *et al.* (2013*a*). The kinetic energy spectra exhibit a Kolmogorov

inertial range with $k^{-5/3}$ scaling. The spatial flux discretisation was performed in characteristic space by an adaptive central-upwind sixth-order-accurate WENO scheme (Hu, Wang & Adams 2010) in the low-dissipation version of Hu & Adams (2011).

LES relies on scale separation, where the energy-containing large scales are resolved and the effect of non-resolved scales is modelled either explicitly or implicitly. However, turbulent mixing initiated by RMI for typical LES mainly occurs at the marginally resolved or non-resolved scales. The interaction of non-resolved small scales with the resolved scales as well as the effect of the interaction of non-resolved scales with themselves is modelled by the employed subgrid-scale model. Moreover, discontinuities such as shock waves and material interfaces need to be captured by the numerical scheme. Owing to the broad range of scales, coarse-grained numerical simulations of RMI strongly rely on the resolution capabilities for the different types of subgrid scales (turbulent small scales, shocks, interfaces) of the underlying numerical scheme.

So far, research has mainly focused on the identification and quantification of parameters that affect the evolution of Richtmyer–Meshkov unstable flows. The influence of the Atwood number (Lombardini *et al.* 2011), the Mach number (Lombardini *et al.* 2012) as well as the specific initial interface perturbations (Schilling & Latini 2010; Thornber *et al.* 2010; Grinstein, Gowardhan & Wachtor 2011) on the temporal evolution of the instability have been investigated. Results from numerical simulations have been compared to experiments (Hill *et al.* 2006; Schilling & Latini 2010; Tritschler *et al.* 2013*b*) and theoretical models have been derived (Thornber *et al.* 2011; Weber *et al.* 2013). These investigations have assumed, based on standard arguments such as empirical resolution criteria, that the marginally and non-resolved scales have a negligible effect on the resolved scales, and therefore on the evolution of the instability. Uncertainties introduced by the numerical method, i.e. the subgrid-scale regularisation and truncation errors, have not yet been investigated systematically. There is, however, strong evidence that numerical model uncertainty can significantly affect the linear and nonlinear stages of evolution, and in particular the mixing measures. In fact, it is unclear how subgrid-scale regularisation and dispersive or dissipative truncation errors can affect the resolved scales and turbulent mixing measures.

In the present investigation, two independently developed and essentially different numerical methods are employed to study the prediction uncertainties of RMI simulations. The first method has a dominantly dissipative truncation error at the non-resolved scales, whereas the second one exhibits a more dispersive behaviour. At the marginally resolved scales, the numerical truncation error is not small and the particular character of the truncation error is essential for the implicit modelling capabilities of the method, and thus also affects the resolved scale solution. For the purpose of investigating this effect, integral and spectral mixing metrics as well as probability density functions are analysed on four computational grids with resolutions ranging from 1562 to 195 μm. The simulations employing two different numerical methods on a very fine grid resolution of 195 μm provide a data set with high confidence in the results.

We emphasise that the purpose of this study is (i) to present RMI results with a clear identification of the resolved scale range by systematic grid refinement, and (ii) to assess the physical effects of numerical subgrid-scale regularisations on the marginally resolved and on the non-resolved scale range. We do not intend to propose or improve a certain subgrid-scale model or regularisation scheme.

The paper is structured as follows. The governing equations along with the employed numerical models are described in § 2. Details about the computational

domain and the exact generic initial conditions are given in § 3. Results are presented in § 4, and the key findings of the present study are discussed in § 5.

2. Numerical model

2.1. *Governing equations*

We solve the three-dimensional multicomponent Navier–Stokes equations:

$$\frac{\partial \rho}{\partial t} + \nabla \cdot (\rho \boldsymbol{u}) = 0, \tag{2.1a}$$

$$\frac{\partial (\rho \boldsymbol{u})}{\partial t} + \nabla \cdot (\rho \boldsymbol{u}\boldsymbol{u} + p\boldsymbol{\delta} - \boldsymbol{\tau}) = 0, \tag{2.1b}$$

$$\frac{\partial E}{\partial t} + \nabla \cdot [(E + p)\boldsymbol{u}] - \nabla \cdot (\boldsymbol{\tau} \cdot \boldsymbol{u} - \boldsymbol{q}_c - \boldsymbol{q}_d) = 0, \tag{2.1c}$$

$$\frac{\partial \rho Y_i}{\partial t} + \nabla \cdot (\rho \boldsymbol{u} Y_i) + \nabla \cdot \boldsymbol{J}_i = 0. \tag{2.1d}$$

In (2.1*a*), $\boldsymbol{u}$ is the velocity vector, p is the pressure, E is the total energy, ρ is the mixture density, Y_i is the mass fraction and $\boldsymbol{J}_i$ is the diffusive mass flux of species $i = 1, 2, \ldots, K$, with K the total number of species. The identity matrix is $\boldsymbol{\delta}$.

The viscous stress tensor $\boldsymbol{\tau}$ for a Newtonian fluid is

$$\boldsymbol{\tau} = 2\bar{\mu}\boldsymbol{S} + (\beta - \tfrac{2}{3}\bar{\mu})\boldsymbol{\delta}(\nabla \cdot \boldsymbol{u}), \tag{2.2}$$

with the mixture viscosity $\bar{\mu}$ and the strain-rate tensor $\boldsymbol{S}$. According to Fourier's law, we define the heat flux as

$$\boldsymbol{q}_c = -\bar{\kappa}\nabla T \tag{2.3}$$

and the inter-species diffusional heat flux (Cook 2009) as

$$\boldsymbol{q}_d = \sum_{i=1}^{K} h_i \boldsymbol{J}_i, \tag{2.4}$$

with

$$\boldsymbol{J}_i \approx -\rho \left(D_i \nabla Y_i - Y_i \sum_{j=1}^{K} D_j \nabla Y_j \right). \tag{2.5}$$

Here D_i indicates the effective binary diffusion coefficient of species i, and h_i is the individual species enthalpy. The equations are closed with the equation of state for an ideal gas,

$$p(\rho e, Y_1, Y_2, \ldots, Y_K) = (\bar{\gamma} - 1)\rho e, \tag{2.6}$$

where $\bar{\gamma}$ is the ratio of specific heats of the mixture and e is the internal energy,

$$\rho e = E - \tfrac{1}{2}\rho \boldsymbol{u}^2. \tag{2.7}$$

The multicomponent as well as the molecular mixing rules for $\bar{\gamma}$, $\bar{\mu}$, D_i and $\bar{\kappa}$ are given in appendices A and B.

2.2. *Numerical methods*

2.2.1. *The Miranda simulation code*

The Miranda simulation code has been used extensively for simulating turbulent flows with high Reynolds numbers and multi-species mixing (Cook, Cabot & Miller 2004; Cabot & Cook 2006; Olson & Cook 2007; Olson *et al.* 2011; Weber *et al.* 2013). Miranda employs a tenth-order compact difference scheme (Lele 1992) for

spatial differentiation and a five-stage fourth-order Runge–Kutta scheme (Kennedy, Carpenter & Lewis 2000) for temporal integration of the compressible multicomponent Navier–Stokes equations. Full details of the numerical method are given by Cook (2007), which includes an eighth-order compact filter that is applied to the conserved variables at each time step and smoothly removes the top 10 % of wavenumbers to ensure numerical stability. For numerical regularisation of non-resolved steep flow gradients, artificial fluid properties are used to damp locally structures that exist on the length scales of the computational mesh. In this approach, artificial diffusion terms are added to the physical ones that appear in equations (2.2), (2.3) and (2.5) as

$$\mu = \mu_f + \mu^*, \tag{2.8}$$
$$\beta = \beta_f + \beta^*, \tag{2.9}$$
$$\kappa = \kappa_f + \kappa^*, \tag{2.10}$$
$$D_i = D_{f,i} + D_i^*. \tag{2.11}$$

This LES method employing artificial fluid properties was originally proposed by Cook (2007), but has been altered by replacing the S (magnitude of the strain rate tensor), with $\boldsymbol{\nabla \cdot u}$ in the equation for β^*. Mani, Larsson & Moin (2009) showed that this modification substantially decreases the dissipation error of the method. Here we give the explicit formulation of the artificial terms on a Cartesian grid,

$$\mu^* = C_\mu \overline{\rho |\nabla^r S|} \Delta^{(r+2)}, \tag{2.12}$$
$$\beta^* = C_\beta \overline{\rho |\nabla^r (\boldsymbol{\nabla \cdot u})|} \Delta^{(r+2)}, \tag{2.13}$$
$$\kappa^* = C_\kappa \overline{\frac{\rho c_s}{T} |\nabla^r e|} \Delta^{(r+1)}, \tag{2.14}$$
$$D_i^* = C_D \overline{|\nabla^r Y_i|} \frac{\Delta^{(r+2)}}{\Delta t} + C_Y \overline{(|Y_i| + |1 - Y_i| - 1)} \frac{\Delta^2}{2\Delta t}, \tag{2.15}$$

where $S = (\boldsymbol{S}:\boldsymbol{S})^{1/2}$ is the magnitude of the strain-rate tensor, $\Delta = (\Delta x \Delta y \Delta z)^{1/3}$ is the local grid spacing, c_s is the sound speed and Δt is the time step size. The polyharmonic operator, ∇^r, denotes a series of Laplacians, e.g. $r = 4$ corresponds to the biharmonic operator, $\nabla^4 = \nabla^2 \nabla^2$. The overbar ($\bar{f}$) denotes a truncated-Gaussian filter applied along each grid direction as in Cook (2007) to smooth out sharp cusps introduced by the absolute value operator. In LES of RMI, β^* acts as the shock-capturing scheme. The μ^* is primarily used as a numerical stabilisation mechanism rather than as a subgrid-scale model. The artificial shear viscosity is found not to be needed to maintain numerical stability in the current calculations and its inclusion has a small impact on the solution. The dissipation of the vortical motion primarily depends on the eighth-order compact filter.

2.2.2. *The INCA simulation code*

The INCA simulation code is a multi-physics simulation method for single- and multicomponent turbulent flows. With respect to the objective in this paper, it has been tested and validated for shock-induced turbulent multi-species mixing problems at finite Reynolds numbers (Tritschler *et al.* 2013*a*,*b*, 2014).

For all the simulations presented in this paper, we use a discretisation scheme that employs for the hyperbolic part in (2.1*a*) a flux projection on local characteristics. The Roe-averaged matrix required for the projection is calculated for the full multi-species

system (Roe 1981; Larouturou & Fezoui 1989; Fedkiw, Merriman & Osher 1997). The numerical fluxes at the cell faces are reconstructed from cell averages by the adaptive central-upwind sixth-order weighted essentially non-oscillatory (WENO-CU6) scheme (Hu *et al.* 2010) in its scale separation formulation by Hu & Adams (2011).

The fundamental idea of the WENO-CU6 scheme is to use a non-dissipative sixth-order central stencil in smooth flow regions and a nonlinear convex combination of third-order stencils in regions with steep gradients. The reconstructed numerical flux at the cell boundaries is computed from

$$\hat{f}_{i+1/2} = \sum_{k=0}^{3} \omega_k \hat{f}_{k,i+1/2}, \tag{2.16}$$

where ω_k is the weight assigned to stencil k with the second-degree reconstruction polynomial approximation for $\hat{f}_{k,i+1/2}$. In the WENO-CU6 framework the weights ω_k are given by

$$\omega_k = \frac{\alpha_k}{\sum_{k=0}^{3} \alpha_k}, \quad \alpha_k = d_k \left(C + \frac{\tau_6}{\beta_k + \epsilon} \right)^q, \tag{2.17}$$

with ϵ being a small positive number $\epsilon = 10^{-40}$. The optimal weights d_k are defined such that the method recovers the sixth-order central scheme in smooth flow regions. The constant parameters in (2.17) are set to $C = 1000$ and $q = 4$ (see Hu & Adams 2011), τ_6 is a reference smoothness indicator that is calculated from a linear combination of the other smoothness measures β_k with

$$\tau_6 = \beta_6 - \tfrac{1}{6}(\beta_0 + \beta_2 + 4\beta_1) \tag{2.18}$$

and

$$\beta_k = \sum_{j=1}^{2} \Delta x^{2j-1} \int_{x-1/2}^{x_{i+1/2}} \left(\frac{\mathrm{d}^j}{\mathrm{d}x^j} \hat{f}_k(x) \right)^2 \mathrm{d}x, \tag{2.19}$$

and β_6 is also calculated from (2.19) but with the fifth-degree reconstruction polynomial approximation of the flux, which gives the six-point stencil for the sixth-order interpolation.

After reconstruction of the numerical fluxes at the cell boundaries, the fluxes are projected back onto the physical field. A local switch to a Lax–Friedrichs flux is used as entropy fix (see e.g. Toro 1999). A positivity-preserving flux limiter (Hu, Adams & Shu 2013) is employed in regions with low pressure or density, maintaining the overall accuracy of the sixth-order WENO scheme. It has been verified that the flux limiter has negligible effect on the results, and avoids excessively small time step sizes. Temporal integration is performed by a third-order total variation-diminishing Runge–Kutta scheme (Gottlieb & Shu 1998).

3. Numerical set-up

3.1. *Computational domain*

We consider a shock tube with constant square cross-section. The fine-grid domain extends in the y and z directions symmetrically from $-L_{yz}/2$ to $L_{yz}/2$ and in the x direction from $-L_x/4$ to L_x. An inflow boundary condition is imposed far away from

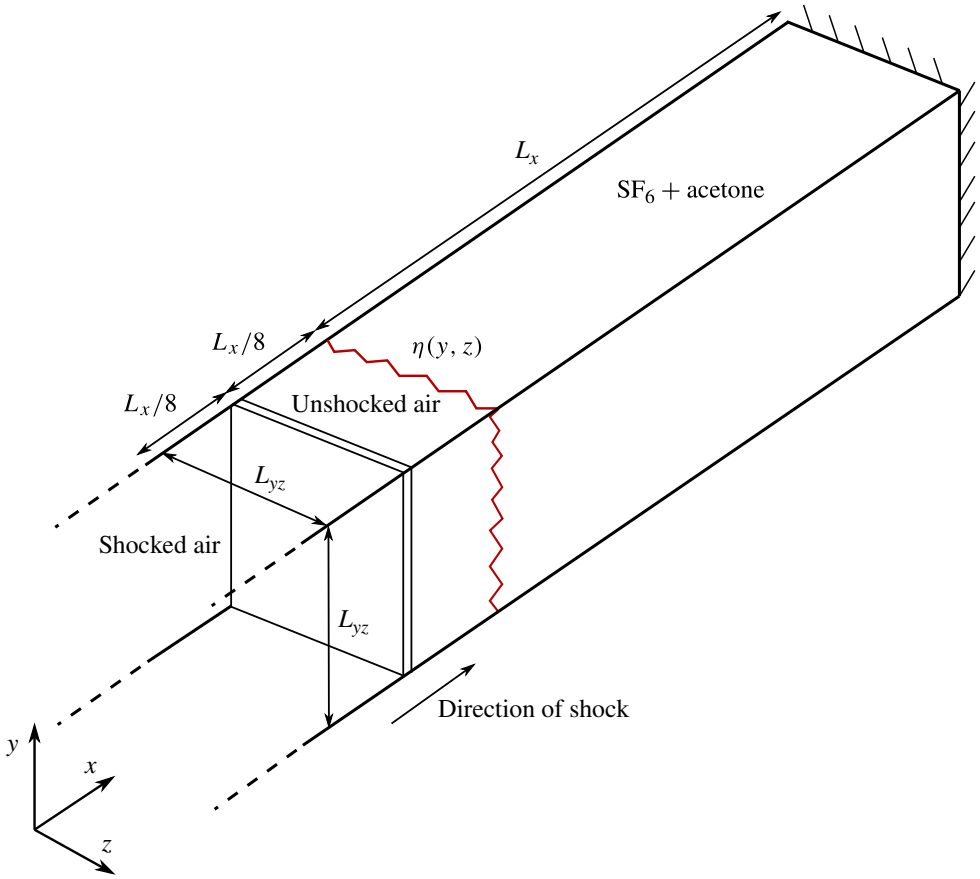

FIGURE 1. (Colour online) Schematic of the square shock tube and dimensions of the computational domain for the simulations.

the fine-grid domain in order to avoid shock reflections. To reduce computational costs, a hyperbolic mesh stretching is applied between the inflow boundary and $-L_x/4$; L_x is set to 0.4 m, and $L_{yz} = L_x/4$. At the boundaries normal to the y and z directions, periodic boundary conditions are imposed and an adiabatic wall boundary at the end of the shock tube at $x = L_x$ is used. A schematic of the computational domain is shown in figure 1.

The fine-grid domain is discretised by four different homogeneous Cartesian grids with 64, 128, 256 and 512 cells in the y and z directions and 320, 640, 1280 and 2560 cells in the x direction, resulting in cubic cells of size $1562\ \mu\text{m} \lesssim \Delta_{xyz} \lesssim 195\ \mu\text{m}$. The total number of cells in the fine-grid domain amounts to $\approx 1.3 \times 10^6$ for the coarsest resolution and to $\approx 670 \times 10^6$ for the finest resolution.

3.2. *Initial conditions*

We consider air as a mixture of nitrogen (N_2) and oxygen (O_2) with (in terms of volume fraction) $X_{N_2} = 0.79$ and $X_{O_2} = 0.21$. The equivalent mass fractions on the air side give $Y_{N_2} = 0.767$ and $Y_{O_2} = 0.233$, i.e. $Y_{air} = Y_{N_2} + Y_{O_2}$. The heavy gas is modelled as a mixture of SF_6 and acetone (Ac) with mass fractions $Y_{SF_6} = 0.8$ and $Y_{Ac} = 0.2$, i.e. $Y_{HG} = Y_{SF_6} + Y_{Ac}$. The material interface between light (air) and heavy gas is accelerated by a shock wave with Mach number $Ma = 1.5$ that is initialised at $x = -L_x/8$ propagating in the positive x direction. The pre-shock state is defined by the stagnation condition $p_0 = 23\,000$ Pa and $T_0 = 298$ K. The corresponding post-shock

Quantity	Post-shock	Pre-shock light-gas side	Pre-shock heavy-gas side
ρ (kg m^{-3})	0.498 69	0.267 84	1.040 57
U (m s^{-1})	240.795	0	0
p (Pa)	56 541.7	23 000	23 000
T (K)	393.424	298	298
D_{N_2} (m^2 s^{-1})	5.919×10^{-5}	8.981×10^{-5}	—
D_{O_2} (m^2 s^{-1})	5.919×10^{-5}	8.981×10^{-5}	—
D_{SF_6} (m^2 s^{-1})	—	—	1.846×10^{-5}
D_{Ac} (m^2 s^{-1})	—	—	1.846×10^{-5}
$\bar{\mu}$ (Pa s)	2.234×10^{-5}	1.826×10^{-5}	1.328×10^{-5}
$\overline{c_p}$ (J kg^{-1} K^{-1})	1008.35	1008.35	815.89

TABLE 1. Initial values of the post-shock state and the pre-shock states of the light- and heavy-gas sides.

thermodynamic state is obtained from the Rankine–Hugoniot conditions,

$$\rho'_{air} = \rho_{air} \frac{(\gamma_{air}+1)Ma^2}{2+(\gamma_{air}-1)Ma^2}, \tag{3.1a}$$

$$u'_{air} = Ma\, c_{air} \left(1 - \frac{\rho_{air}}{\rho'_{air}}\right), \tag{3.1b}$$

$$p'_{air} = p_0 \left(1 + 2\frac{\gamma_{air}}{\gamma_{air}+1}(Ma^2-1)\right), \tag{3.1c}$$

with $c_{air} = \sqrt{\gamma_{air} p_0/\rho_{air}}$. The initial data of the post-shock state of the light gas as well as the pre-shock state of the light and heavy gases are given in table 1.

Tritschler *et al.* (2013*a*) introduced a generic initial perturbation of the material interface that resembles a stochastic random perturbation but being, however, deterministic and thus exactly reproducible for different simulation runs. This multimode perturbation is given by the function

$$\eta(y,z) = a_1 \sin(k_0 y)\sin(k_0 z) + a_2 \sum_{n=1}^{13}\sum_{m=3}^{15} a_{n,m} \sin(k_n y + \phi_n)\sin(k_m z + \chi_m) \tag{3.2}$$

with the constant amplitudes $a_1 = -0.0025$ m and $a_2 = 0.000\,25$ m and wavenumbers $k_0 = 10\pi/L_{yz}$, $k_n = 2\pi n/L_{yz}$ and $k_m = 2\pi m/L_{yz}$. The amplitudes $a_{n,m}$ and the phase shifts ϕ_n and χ_m are given by

$$a_{n,m} = \sin(nm)/2, \tag{3.3a}$$

$$\phi_n = \tan(n), \tag{3.3b}$$

$$\chi_m = \tan(m). \tag{3.3c}$$

To facilitate a grid sensitivity study, we impose an initial length scale by prescribing a finite initial interface thickness in the mass fraction field as

$$\psi(x,y,z) = \frac{1}{2}\left(1 + \tanh\left(\frac{x-\eta(y,z)}{L_\rho}\right)\right) \tag{3.4}$$

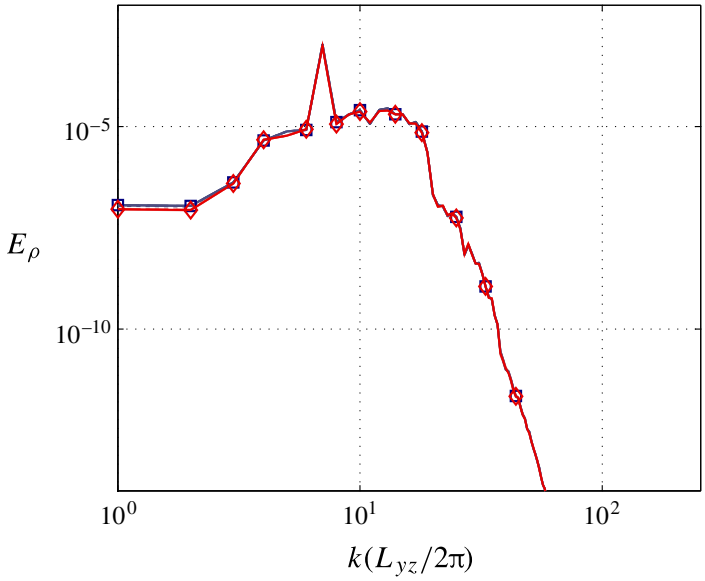

FIGURE 2. (Colour online) Initial power spectra of density from Miranda (dark grey; blue online) and INCA (light grey; red online). The different resolutions are represented as dotted line (64), dashed line (128), solid line (256) and solid line with open squares for Miranda and open diamonds for INCA (512).

with $L_\rho = 0.01$ m being the characteristic initial thickness. The individual species mass fractions are set as

$$Y_{SF_6} = 0.8\psi, \quad Y_{Ac} = 0.2\psi, \tag{3.5a,b}$$

$$Y_{N_2} = 0.767(1-\psi), \quad Y_{O_2} = 0.233(1-\psi). \tag{3.6a,b}$$

The material interface is initialised at $x - \eta(y, z) = 0$ m. Combined with the multicomponent and molecular mixing rules given in appendices A and B, the flow field is fully defined at $t = 0$.

Figure 2 shows the initial condition in terms of the power spectrum of density for Miranda and INCA at all grid resolutions. The initial perturbation given in (3.2) and shown in figure 2 has been designed with the objective to obtain a reproducible and representative data set. Nevertheless, we cannot exclude the possibility that some of the observations presented in this paper do not apply to very different initial perturbations.

4. Results

To explore the effect of the finite truncation error arising from grid resolution and numerical method, four meshes were used to compute the temporal evolution of RMI with both Miranda and INCA. The simulation reaches $t = 6.0$ ms, which is well beyond the occurrence of re-shock at $t \approx 2$ ms. At this stage, the effects of reflected shock waves and expansion waves on the shock location have become small, as the shock wave is attenuated with each subsequent reflection. The space–time (x–t) diagram shown in figure 3 depicts the propagation of the shock wave and interface during the simulation.

The initial conditions described in the previous section are entirely deterministic and, owing to their band-limited representations, are identically imposed at the different grid resolutions and for the two numerical methods. Therefore, the obtained results

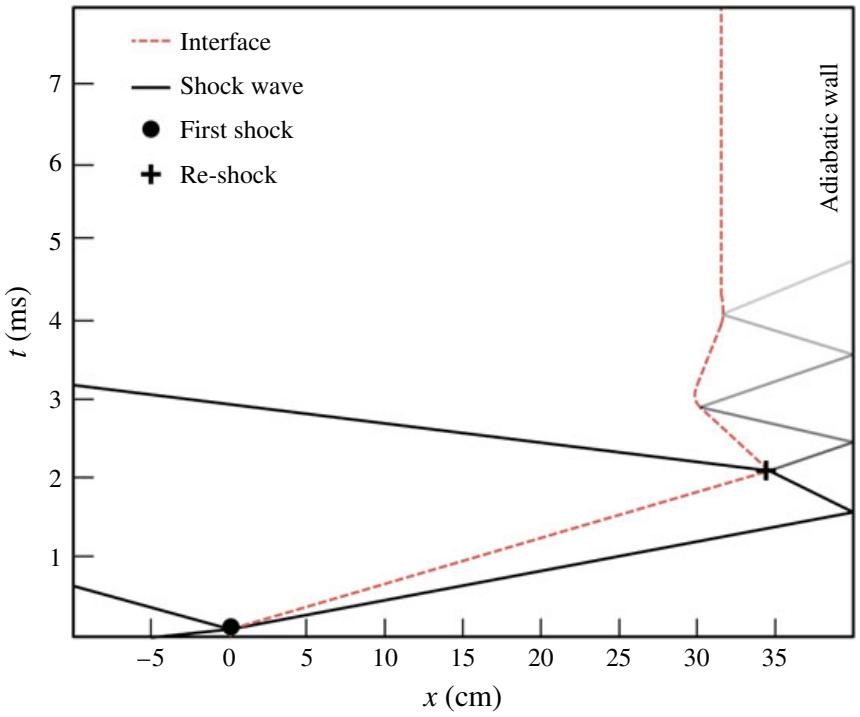

FIGURE 3. (Colour online) Space–time (x–t) diagram depicting the propagation of the shock wave and interface during the simulation. The effect of the shock wave on the interface location is attenuated with each subsequent reflection.

exhibit uncertainties due only to the numerical method and to grid resolution, but exclude initial-data uncertainties.

For illustration we show the three-dimensional contour plots of species mass fraction of the heavy gas Y_{HG} obtained with Miranda and INCA, respectively, in figure 4. Similarities at the large scales are clearly visible after re-shock, but also differences exist at the fine scales, more clearly visible from the inset.

4.1. *Integral quantities*

Integral measures of the mixing zone are presented here for both numerical models and all resolutions. Often, these time-dependent integral measures are the only metrics available for comparison with experiment and are therefore of primary importance for validation.

Figure 5 shows the transition process predicted by the reference grid with a resolution of 512 cells in the transverse directions. The numerical challenge, prior to re-shock, is to predict the large-scale nonlinear entrainment and the associated interface steepening. The interface eventually becomes under-resolved when its thickness reaches the resolution limit of the numerical scheme and further steepening is prevented by numerical diffusion. The equilibrium between interface steepening and numerical diffusion occurs later in time as the grid is refined. The accurate prediction of the interface steepening phenomenon is one of the main challenges in modelling pre-transitional RMI where large-scale flow structures are still regular. This is because the numerical model largely determines the time when mixing transition occurs. In nature, mixing transition is due to the presence of small-scale perturbations, whereas in numerical simulation, the transition is triggered by backscatter from the under-resolved scales as predicted by the particular numerical model. Hence, details of mixing transition of the material interface evolve differently for the two codes.

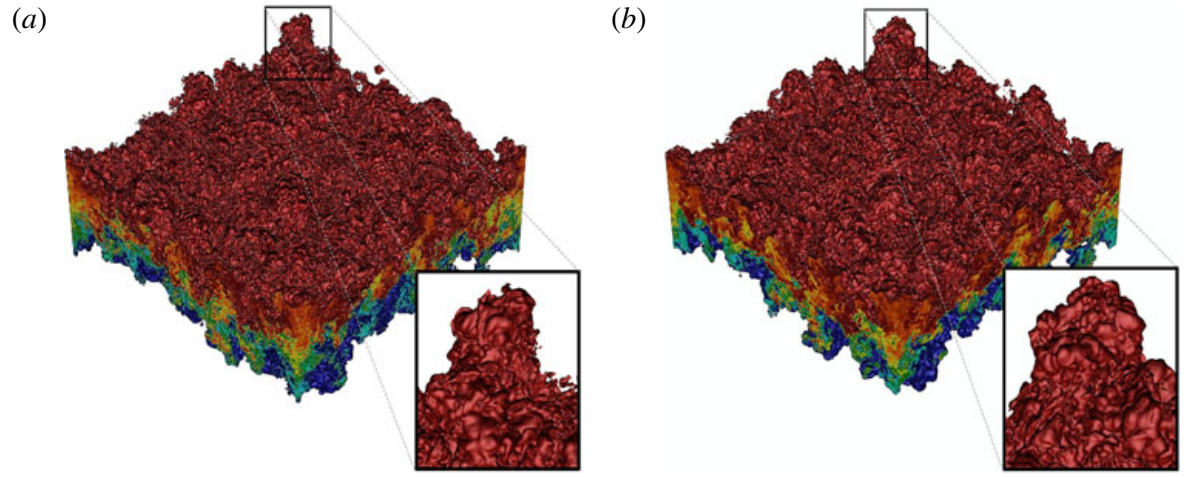

FIGURE 4. (Colour online) Three-dimensional contour plots of species mass fraction of the heavy gas from (*a*) Miranda and (*b*) INCA data. Data are from the finest grid at $t = 2.5$ ms that show contours of the heavy-gas mass fraction Y_{HG} from 0.1 (at the bottom; blue online) to 0.9 (at the top; red online). Note that, although some large-scale features remain consistent between codes, small and intermediate scales are quite different at this stage.

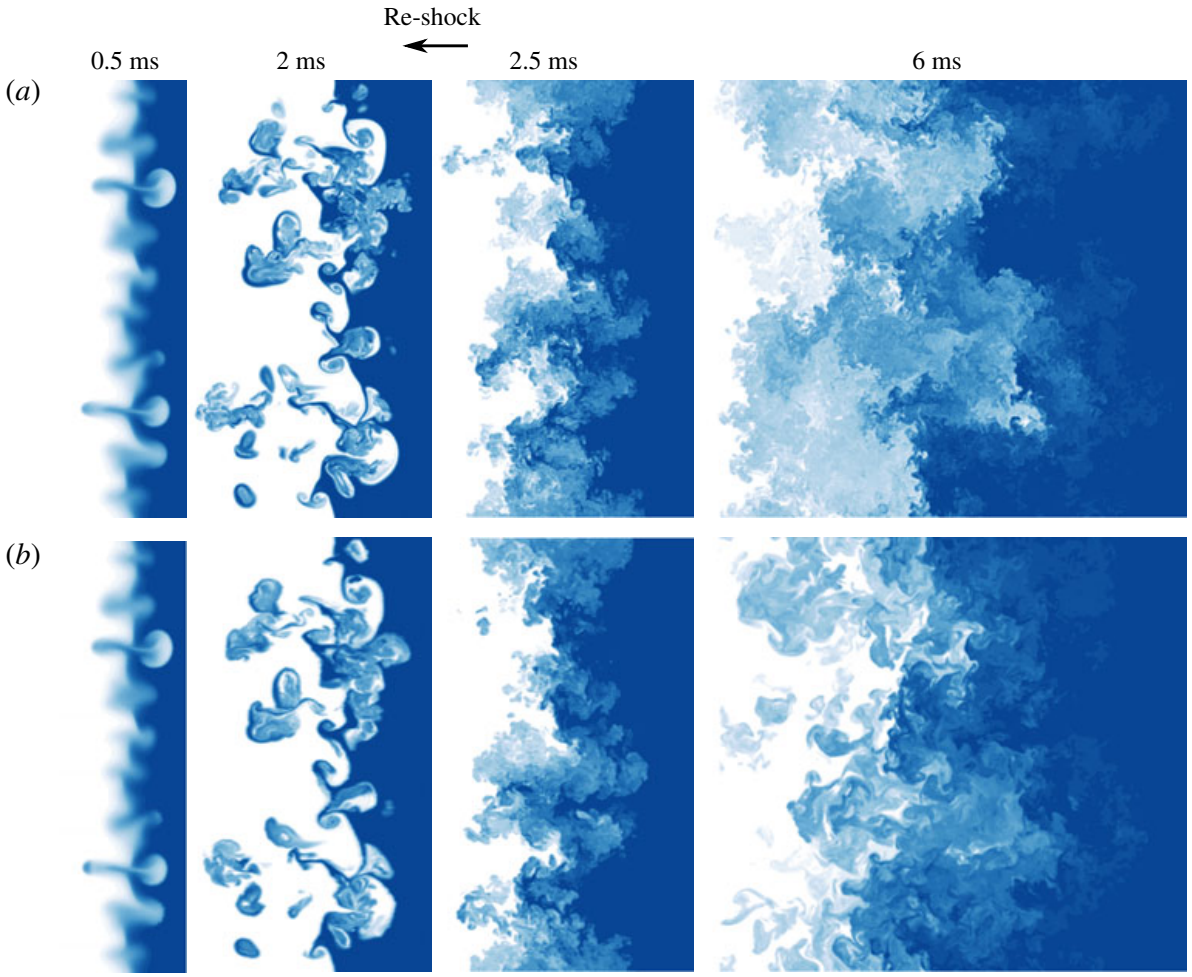

FIGURE 5. (Colour online) Colour-coded plots of species mass fraction of SF_6 gas from (*a*) Miranda and (*b*) INCA at various times where data are taken from the finest grid. The contours range from 0.05 (white) to 0.75 (dark grey; blue online).

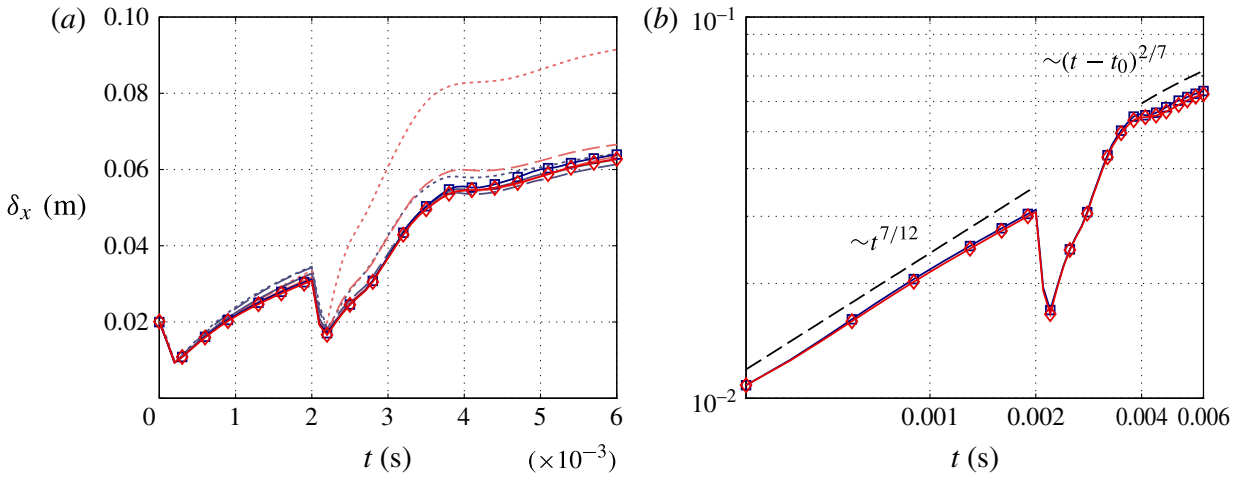

FIGURE 6. (Colour online) Time evolution of the mixing zone width from Miranda (dark grey; blue online) and INCA (light grey; red online). The different resolutions are represented as dotted line (64), dashed line (128), solid line (256) and solid line with open squares for Miranda and open diamonds for INCA (512).

Nevertheless, similarities before re-shock are striking and large-scale similarities in the resolved wavenumber range even persist throughout the entire simulation time. Following re-shock, the large interfacial scales break down into smaller scales and develop a turbulent mixing zone as can be seen in figures 4 and 5. By visual inspection of figure 5, one finds that the post-re-shock turbulent structures are very similar, whereas the long-term evolution of the small scales appears to be different between the codes. Differences in the observed flow field at $t = 6$ ms may indicate slightly different effective Reynolds numbers for the two numerical methods and therefore they also exhibit different decay rates of enstrophy (Dimotakis 2000; Lombardini *et al.* 2012), as can be seen in figure 8 after re-shock.

The mixing width δ_x is a length scale that approximates the large-scale temporal evolution of the turbulent mixing zone. It is defined as an integral measure by

$$\delta_x(t) = \int_{-\infty}^{\infty} 4\phi(1-\phi)\mathrm{d}x, \quad \text{with } \phi(x,t) = \langle Y_{\mathrm{SF}_6} + Y_{\mathrm{Ac}} \rangle_{yz}, \tag{4.1}$$

where $\langle\cdot\rangle_{yz}$ denotes the ensemble average in the cross-stream yz plane. For a quantity φ it is defined by

$$\langle\varphi\rangle_{yz}(x,t) = \frac{1}{\mathscr{A}} \iint \varphi(x,y,z,t)\,\mathrm{d}y\,\mathrm{d}z, \quad \text{with } \mathscr{A} = \iint \mathrm{d}y\,\mathrm{d}z. \tag{4.2}$$

The mixing width plotted in figure 6(*a*) shows that data from both numerical methods converge to a single solution throughout the entire simulation time. Furthermore, it is observed that even with very-high-order models a minimum resolution of $\sim$400 μm appears to be necessary for an accurate prediction of the mixing zone width. As will be shown later, coarser grids tend to overpredict not only the growth of the mixing zone but also molecular mixing.

Figure 6(*b*) shows the mixing zone width time evolution on a log–log scale. The (bubble) growth-rate model of Zhou (2001) predicts accurately the pre-re-shock mixing zone growth rate that is consistently recovered by both numerical methods as $\sim t^{7/12}$. However, this is, according to Zhou (2001), the growth rate that is associated with turbulence of Batchelor type (Batchelor & Proudman 1956) with $E(k) \sim k^4$

as $k \to 0$. The kinetic energy spectra in the present investigation are of Saffman type (Saffman 1967*a*,*b*) with $E(k) \sim k^2$ as $k \to 0$ (Tritschler *et al.* 2013*a*), for which Zhou (2001) predicts a growth that scales with $\sim t^{5/8}$. The present growth rates are also in good agreement with the experimental and numerical results of Dimonte, Frerking & Schneider (1995) with $\sim t^{\beta}$ and $\beta = 0.6 \pm 0.1$ and their model predictions $\sim (t - t_i)^{1/2}$, where t_i accounts for the time the shock needs to traverse the interface. As the mixing zone has not yet reached self-similar evolution, the initial growth rate depends on the specific initial conditions.

Llor (2006) found that the self-similar growth rate of the energy-containing eddies, i.e. the integral length scale, for incompressible RMI at vanishing Atwood number, should scale as $\delta_x \sim t^{1-n/2}$ with $2/7 \leqslant 1 - n/2 \leqslant 1/3$, if the turbulence kinetic energy (TKE) decays as $\sim t^{-n}$. These growth rates slightly differ from the growth-rate prediction for homogeneous isotropic turbulence, $1/3 \leqslant 1 - n/2 \leqslant 2/5$, by the same author. The predictions of Llor (2006), however, are at odds with Kolmogorov's classical decay law (Kolmogorov 1941) for TKE $\sim t^{-10/7}$ and more recent investigations of decaying isotropic turbulence by Ishida, Davidson & Kaneda (2006) and Wilczek, Daitche & Friedrich (2011), which found Kolmogorov's decay law to hold if the Loitsyansky integral is constant and if the Taylor-scale Reynolds number exceeds $Re_\lambda \geqslant 100$. Based on Rayleigh–Taylor experiments driven by either sustained or impulsive acceleration at various Atwood numbers, Dimonte & Schneider (2000) found scaling laws for the bubble and spike growth rate. For the present density ratio, the exponents become $1 - n_B/2 \approx 0.25 \pm 0.05$ for the former and $0.25 \leqslant 1 - n_S/2 \leqslant 0.43$ for the latter. The late-time mixing zone growth rate is therefore expected to correlate with the spike growth rate. The late-time growth-rate prediction of the present work is $\sim (t - t_0)^{2/7}$, i.e. $1 - n/2 = 2/7$, once the turbulent mixing zone is fully established. Time t_0 is a virtual time origin set to $t_0 = 2$ ms. This is consistent with the mixing zone width growth-rate predictions of Llor (2006) and the late-time growth-rate predictions of Dimonte & Schneider (2000), but underestimates the predictions of Zhou (2001), with a scaling of $t^{1-n/2}$ with $0.35 \leqslant 1 - n/2 \leqslant 0.45$ long after re-shock, once the nonlinear time scale has become the dominant time scale. In the numerical investigation of Lombardini *et al.* (2012), the authors found the mixing zone width to grow as $0.2 \leqslant 1 - n/2 \leqslant 0.33$. Before re-shock the infrared part of the kinetic energy spectrum (see figure 14) exhibits a k^2 range, for which a post-re-shock growth rate of $\sim t^{2/7}$ is predicted by the model of Youngs (2004), which is in good agreement with the present data.

The definition of the molecular mixing fraction Θ (Youngs 1991, 1994) is given as

$$\Theta(t) = \frac{\displaystyle\int_{-\infty}^{\infty} \langle X_{air} X_{HG} \rangle_{yz} \, \mathrm{d}x}{\displaystyle\int_{-\infty}^{\infty} \langle X_{air} \rangle_{yz} \, \langle X_{HG} \rangle_{yz} \, \mathrm{d}x} \tag{4.3}$$

and quantifies the amount of mixed fluid within the mixing zone. It can be interpreted as the ratio of molecular mixing to large-scale entrainment by convective motion.

As bubbles of light air and spikes of heavy gas begin to interfuse, the initially mixed interface between the fluids steepens and the fluids become more segregated on the molecular level (see figure 7*a*). The molecular mixing fraction reaches its minimum at $t \approx 1.3$ ms before Kelvin–Helmholtz instabilities lead to an increase of molecular mixing. The onset of secondary instabilities is very sensitive to the numerical method, as the numerical scheme determines how sharp the material interface can be represented or whether numerical diffusion or dispersion effects lead to an early mixing transition.

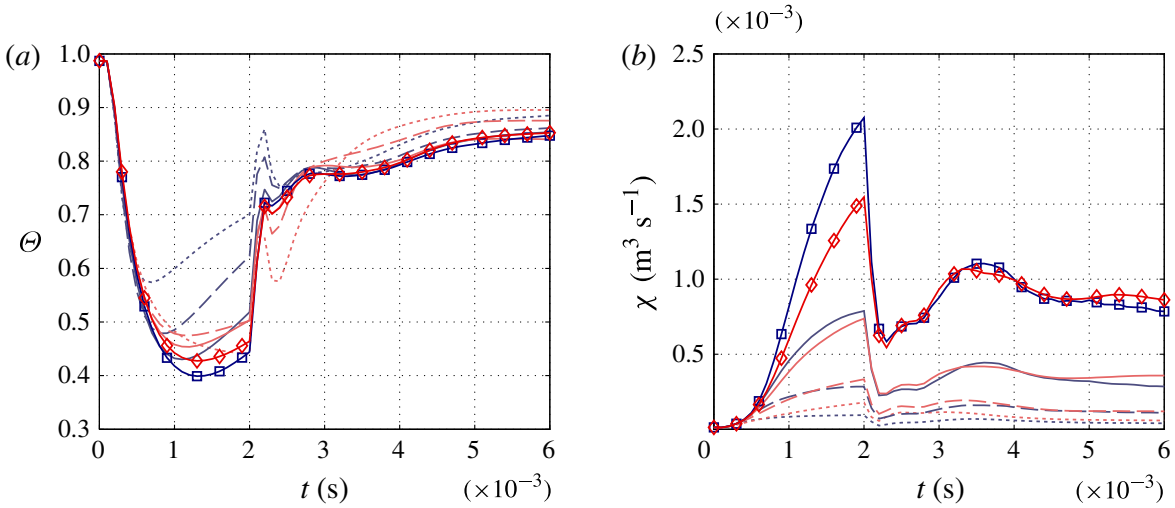

FIGURE 7. (Colour online) Molecular mixing fraction Θ and scalar dissipation rate χ from Miranda (dark grey; blue online) and INCA (light grey; red online). The different resolutions are represented as dotted line (64), dashed line (128), solid line (256) and solid line with open squares for Miranda and open diamonds for INCA (512).

After re-shock molecular mixing is strongly enhanced and reaches its maximum of $\Theta \approx 0.85$ by the end of the simulation. This finding is consistent with Lombardini *et al.* (2012), who also found an asymptotic late-time mixing behaviour with $\Theta \approx 0.85$ independent of the shock Mach number but without re-shock. The asymptotic limit is already accurately calculated on grid resolutions of ∼400 μm. As the second shock wave compresses the mixing zone, the instability becomes less entrained yet equally diffused (at least in the y and z directions) and therefore causes a steep rise in Θ. A gradual increase of the mixing fraction after the steep rise occurs as the mixing zone becomes more homogeneously distributed (Thornber *et al.* 2011) due to turbulent motion.

The temporal evolution of the scalar dissipation rate is plotted in figure 7(*b*) and is derived from the advection–diffusion equation for a scalar. The instantaneous scalar dissipation rate of the three-dimensional RMI is estimated from the SF_6 concentration field as

$$\chi(t) = \int_{-\infty}^{\infty} D_{SF6} \nabla Y_{SF6} \cdot \nabla Y_{SF6} \, \mathrm{d}x \, \mathrm{d}y \, \mathrm{d}z, \tag{4.4}$$

which quantifies the rate at which mixing occurs. For consistency of post-processing, a second-order central difference scheme has been used for the calculation of the spatial derivatives in (4.4) and (4.6) for all simulation data sets. Note that the order of the finite difference scheme with which the gradients in (4.4) and (4.6) are approximated affect their results.

The variation of the scalar dissipation rate with grid resolution before re-shock is largely due to the under-resolved material interface and the onset of mixing transition. Mixing is strongly enhanced after the second shock–interface interaction, but the mixing zone is also confined to a much smaller region, which results in a decrease of the integral χ. Also, χ only represents the resolved part of the dissipation rate and therefore certainly underestimates the true value.

The TKE and the enstrophy (ε) are integrated over cross-flow planes in the mixing zone that satisfy

$$4\phi[1-\phi] \geqslant 0.9. \tag{4.5}$$

This region is referred to as the inner mixing zone (IMZ) in the following.

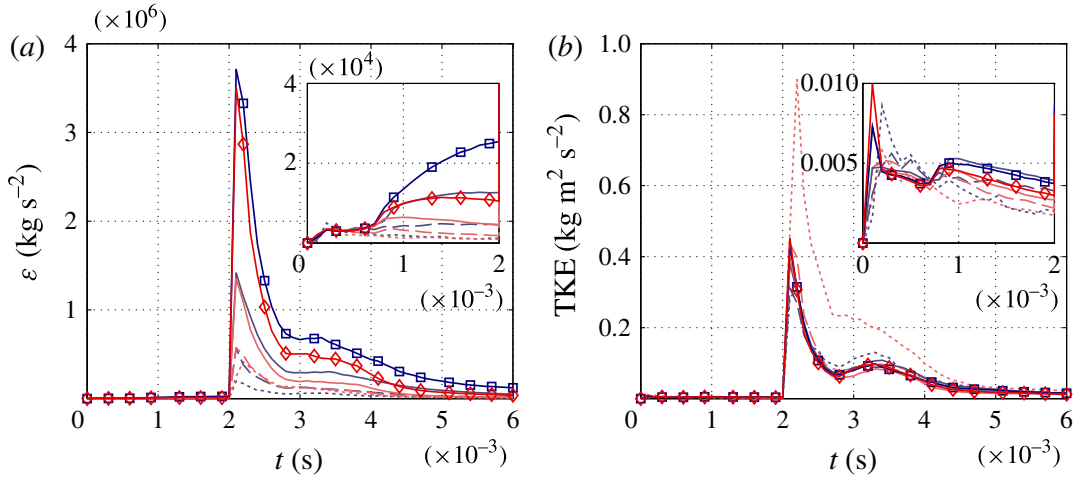

FIGURE 8. (Colour online) Enstrophy ε and turbulence kinetic energy (TKE) from Miranda (dark grey; blue online) and INCA (light grey; red online). The different resolutions are represented as dotted line (64), dashed line (128), solid line (256) and solid line with open squares for Miranda and open diamonds for INCA (512).

Baroclinic vorticity is deposited at the material interface during shock passage. The amount of generated vorticity scales directly with the pressure gradient of the shock wave and the density gradient of the material interface. The enstrophy is calculated by

$$\varepsilon(t) = \int_{IMZ} \rho(\omega_i \omega_i)\, \mathrm{d}x\, \mathrm{d}y\, \mathrm{d}z, \tag{4.6}$$

where ω_i is the vorticity.

As can be seen from figure 8, the enstrophy also exhibits a strong grid dependence. Fully grid-converged results are only obtained for times up to $t \approx 0.7$ ms. As the interface steepens due to strain and shear, the effective interface thickness is determined by numerical diffusion, which appears to occur at $t \approx 0.7$ ms. This is consistent with the evolution of Θ shown in figure 7(*a*). Following Youngs (2007) and Hahn *et al.* (2011), integration of enstrophy with a theoretical scaling of $k^{1/3}$ up to the cut-off wavenumber yields a proportionality between enstrophy and grid resolution as $\varepsilon \propto \Delta_{xyz}^{-4/3}$. From this follows an increase of enstrophy by a factor of approximately 2.5 from one grid resolution to the next finer, which is in good agreement with the present data.

The amount of TKE created by the impulsive acceleration of the interface is calculated as

$$\mathrm{TKE}(t) = \int_{IMZ} K\, \mathrm{d}x\, \mathrm{d}y\, \mathrm{d}z, \quad \text{with } K(x, y, z, t) = \frac{\rho}{2} u_i'' u_i''. \tag{4.7}$$

The fluctuating part φ'' of a quantity φ is calculated from

$$\varphi'' = \varphi - \bar{\varphi}, \quad \text{with } \bar{\varphi} = \langle \rho\varphi \rangle_{yz} / \langle \rho \rangle_{yz}, \tag{4.8}$$

where $\bar{\varphi}$ is the Favre average of φ.

Grid-converged TKE is obtained on grids with a minimum resolution of ~400 μm (see figure 8). This is consistent with the convergence rate of the mixing zone width. The total TKE deposited in the IMZ by the first shock–interface interaction can be seen in the inset of figure 8. The re-shock occurring at $t \approx 2$ ms deposits approximately 40 times more TKE than the initial shock wave. Hill *et al.* (2006)

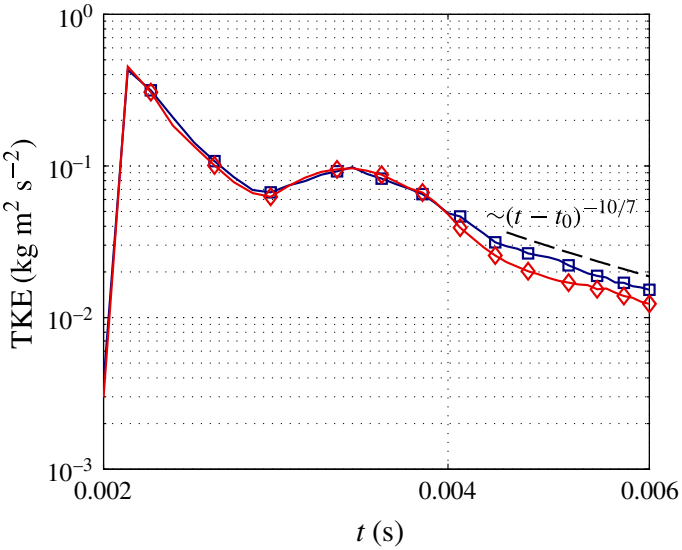

FIGURE 9. (Colour online) Log–log representation of TKE from Miranda (squares; blue online) and INCA (diamonds; red online) taken from the finest grid (512).

found a similar relative increase by the re-shock at the same shock Mach number. A significant decay in energy occurs immediately following re-shock. The material interface interacts with the first expansion fan (see figure 3) and results in a further increase in TKE between 3 and 3.5 ms. The amount of energy deposited by the first expansion wave, however, is much weaker than that deposited by the reflected shock wave. Hill *et al.* (2006) and Grinstein *et al.* (2011) found the amplification of TKE by the first rarefaction to be much stronger than for our data. Such differences are not surprising, because Grinstein *et al.* (2011) reported a strong dependence of energy deposition on the respective initial interface perturbations. After the first expansion wave has interacted with the interface, TKE decays slowly and the pressure gradients associated with the subsequent rarefactions are too shallow to generate any further noticeable increase in TKE.

Lombardini *et al.* (2012) found the decay rate of TKE to be larger than $\sim t^{-6/5}$, approaching $\sim t^{-10/7}$. In our data, the late-time TKE decay is also approximately $\sim(t - t_0)^{-10/7}$, with $t_0 = 2$ ms being the virtual time origin (see figure 9). This scaling would be characteristic for Batchelor-type turbulence (Batchelor & Proudman 1956) with a constant Loitsyansky integral (Kolmogorov 1941; Ishida *et al.* 2006) in contrast to $\sim t^{-6/5}$ typical for turbulence of Saffman type (Saffman 1967*a*,*b*).

In the limit of a self-similar quasi-isotropic state, the temporal evolution of the integral length scale δ_x is related to the evolution of TKE in the mixing zone. From TKE $\propto t^{-n}$, the growth rate of the integral scale follows as $\delta_x \propto t^{1-n/2}$. Llor (2006) derived a maximum decay rate of TKE $\sim t^{-10/7}$ that corresponds to a growth-rate scaling of the energy-containing eddies of $\delta_x \sim t^{2/7}$. These predictions are in excellent agreement with the growth-rate predictions of the mixing zone width of the present investigation (see figure 6) and the decay rate of TKE (see figure 9).

The scalings indicated for the growth rate of the mixing zone and the decay rate of TKE in figures 6 and 9 were not fitted in a strict sense. They merely serve as reference for comparison with incompressible isotropic decaying turbulence. The narrow data range of only $\approx$2 ms after re-shock for which the flow exhibits a self-similar regime precludes any precise estimates for decay and growth-rate laws.

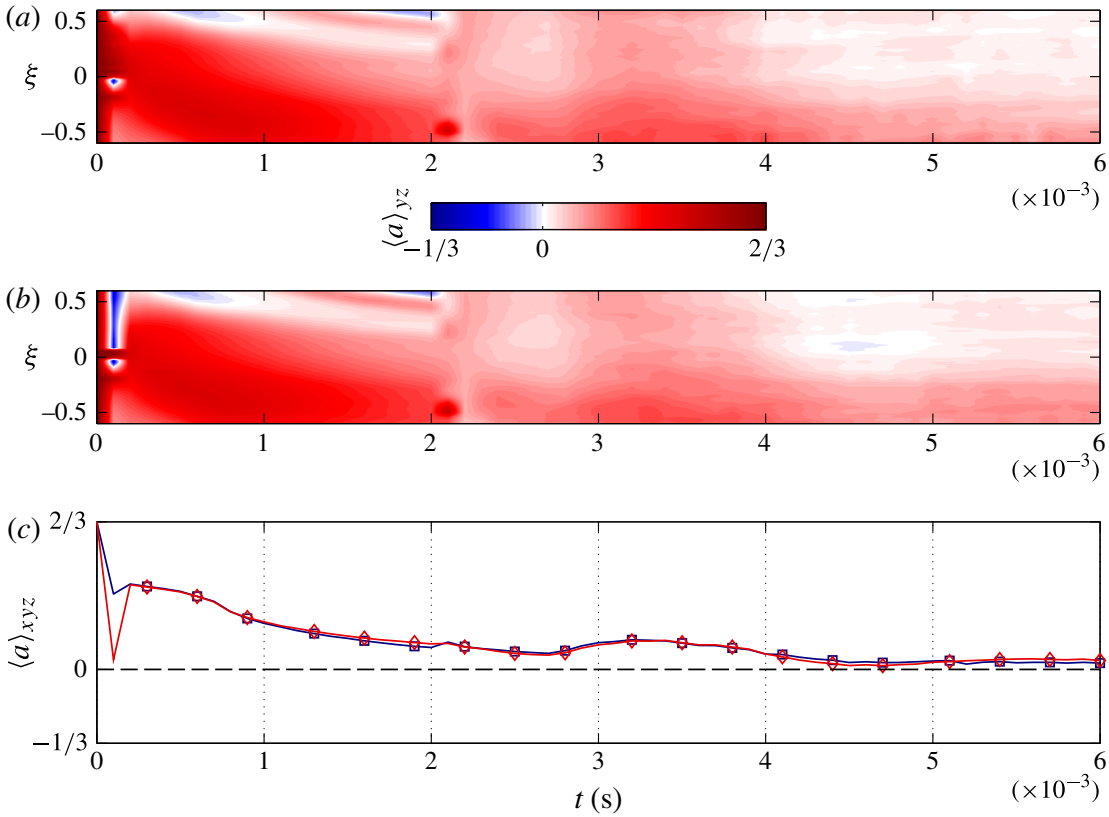

FIGURE 10. Anisotropy $\langle a\rangle_{yz}$ as a function of the dimensionless mixing zone coordinate ξ and time from (*a*) Miranda and (*b*) INCA. (*c*) The volume-averaged anisotropy $\langle a\rangle_{xyz}$ of the inner mixing zone from Miranda (squares) and INCA (diamonds). All data are taken from the finest grid (512).

4.2. *Anisotropy and inhomogeneity of the mixing zone*

In the following, the anisotropy in the mixing zone is investigated. We define the local anisotropy as

$$a(x, y, z, t) = \frac{|u''|}{|u''| + |v''| + |w''|} - \frac{1}{3}, \tag{4.9}$$

where $a = 2/3$ corresponds to having all TKE in the streamwise velocity component u'', whereas $a = -1/3$ corresponds to having no energy in the streamwise u'' component. In figure 10(*a*,*b*) we show the yz plane averaged anisotropy $\langle a\rangle_{yz}$ as a function of the dimensionless mixing zone coordinate ξ and time from Miranda and INCA. The dimensionless mixing zone coordinate ξ is defined as

$$\xi = \frac{x - x^*(t)}{\delta_x(t)}, \tag{4.10}$$

with $x^*(t)$ being the x location where $4(1 - \phi(x, t))\phi(x, t)$ is maximal.

The light-gas side of the mixing zone remains more anisotropic than the heavy-gas side but with a homogeneous anisotropy distribution after re-shock on either side. The volume-averaged anisotropy in the inner mixing zone $\langle a\rangle_{xyz}$ is shown in figure 10(*c*). No full recovery of isotropy of the mixing zone is achieved, and the re-shock does not significantly contribute in the sense of the volume-averaged quantity $\langle a\rangle_{xyz}$, but leads to a stratified anisotropy distribution around the centre of the mixing zone. After $t \approx 4.5$ ms an asymptotic limit of $\langle a\rangle_{xyz} \approx 0.04$ is reached, which

temporally coincides with the onset of the self-similar decay of TKE (see figures 9 and 10). The positive value of $\langle a \rangle_{xyz}$ implies that the streamwise component u'' remains, despite re-shock, the dominant velocity component throughout the simulation time. Lombardini *et al.* (2012) also found a temporal asymptotic limit of the isotropisation process in their simulations. Grinstein *et al.* (2011) observed that the velocity fluctuations in the mixing zone are more isotropic when the initial interface perturbations also include short wavelengths, in which case the authors nearly recovered full isotropy. When Grinstein *et al.* (2011) used long-wavelength perturbations, the mixing zone remained anisotropic except for a narrow range on the heavy-gas side.

In order to quantify the homogeneity of mixing, we calculate the density-specific volume correlation (Besnard *et al.* 1992)

$$\langle b \rangle_{yz}(\xi, t) = \left\langle -\left(\frac{1}{\rho}\right)'' \rho'' \right\rangle_{yz} = \left\langle \frac{1}{\rho} \right\rangle_{yz} \langle \rho \rangle_{yz} - 1, \tag{4.11}$$

which is non-negative. The value $\langle b \rangle_{yz} = 0$ corresponds to homogeneously mixed fluids with constant pressure and temperature. Large values indicate spatial inhomogeneities in the respective yz plane. The density-specific volume correlation has gained some attention in recent years and was the subject of several experimental investigations of the RMI – see Balakumar *et al.* (2012), Balasubramanian *et al.* (2012), Balasubramanian, Orlicz & Prestridge (2013), Orlicz, Balasubramanian & Prestridge (2013), Tomkins *et al.* (2013) and Weber *et al.* (2014).

Figure 11(*a*,*b*) shows the density-specific volume correlation normalised by the maximal value at time t,

$$\widetilde{\langle b \rangle}_{yz} = \langle b \rangle_{yz}(\xi, t) / \max(\langle b \rangle_{yz})(t), \tag{4.12}$$

as a function of the dimensionless mixing zone coordinate ξ and time from Miranda and INCA. The largest values of $\widetilde{\langle b \rangle}_{yz}$ are found around the centre of the mixing zone slightly shifted towards the heavy-gas side. The value of $\widetilde{\langle b \rangle}_{yz}$ peaks around the region where mixing between light and heavy gas occurs and tends to zero outside the mixing region, towards the respective pure-gas side. Weber *et al.* (2014) observed in their experiment that the peak of the density-specific volume correlation is initially shifted towards the light-gas side, but moves towards the centre of the mixing zone with increasing time.

In contrast to the anisotropy, where the re-shock does not contribute to the isotropisation and which levels out after $t \approx 4.5$ ms, the mixing zone becomes significantly more homogeneous after re-shock, as can be observed from the temporal evolution of the volume average of the density-specific volume correlation in the inner mixing zone $\langle b \rangle_{xyz}$. Following re-shock the fluids become more and more mixed (see figure 11*c*), with a value of $\langle b \rangle_{xyz} \approx 0.13$ at the latest time. The measured values of the density-specific volume correlation in the single shock–interface interaction experiment of Weber *et al.* (2014) at $Ma = 2.2$ are in good agreement with our simulated values at late times $O(0.1)$, whereas at the lower Mach number $Ma = 1.6$ Weber *et al.* (2014) observed a more inhomogeneous mixing zone $O(0.2)$. These values are significantly larger than those measured for instance in the shock-gas-curtain experiments of Orlicz *et al.* (2013) and Tomkins *et al.* (2013).

4.3. *Spectral quantities*

From homogeneous isotropic turbulence, it is well known that vorticity exhibits coherent worm-like structures with diameter of the order of the Kolmogorov length

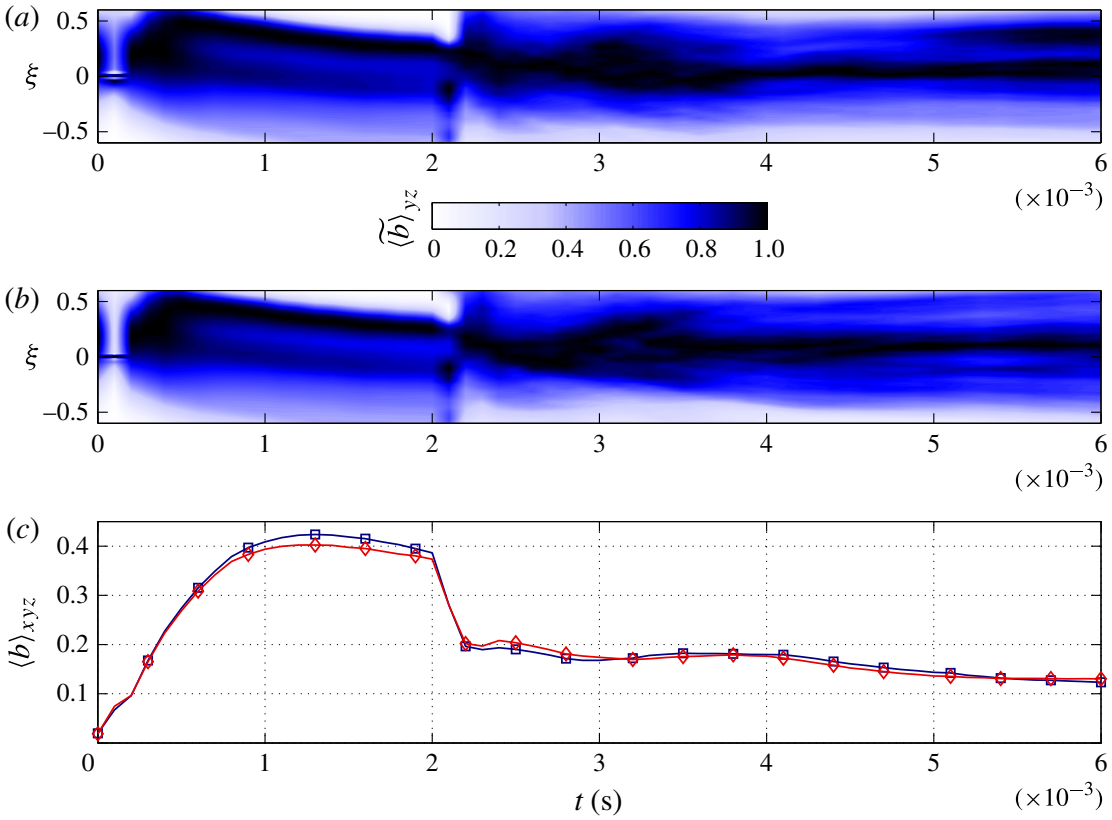

FIGURE 11. (Colour online) Normalised density-specific volume correlation $\widetilde{\langle b\rangle}_{yz}$ as a function of the dimensionless mixing zone coordinate ξ and time from (*a*) Miranda and (*b*) INCA. (*c*) The volume-averaged density-specific volume correlation $\langle b\rangle_{xyz}$ of the inner mixing zone from Miranda (squares) and INCA (diamonds). All data are taken from the finest grid (512).

scale and of a length that scales with the integral scale of the flow. The work of Jiménez *et al.* (1993) suggests that these structures are especially intense features of the background vorticity and independent of any particular forcing that generates the vorticity. In contrast to forced homogeneous isotropic turbulence, where self-similar stationary statistics are achieved, shock-induced turbulent mixing is an inhomogeneous anisotropic unsteady decay phenomenon. Nevertheless, homogeneous isotropic turbulence is used as theoretical framework for most of the numerical analysis of RMI. However, it is unclear at what time and at what locations the mixing zone exhibits the appropriate features and if homogeneous isotropic turbulence is achieved at all. A fully isotropic mixing zone is never obtained, as the anisotropy, even though decreasing with time, reaches an asymptotic limit at $t \approx 4.5$ ms.

The temporal evolution of the initial perturbation is depicted in figure 12. Before re-shock the dominant modes of the initial perturbation slowly break down. After re-shock, however, the additional vorticity deposited during the second shock–interface interaction rapidly destroys structures generated by the initial perturbation and initial shock, leading to a self-similar decay after $t \approx 4$ ms.

Thornber *et al.* (2010, 2012) found, formally in the limit of infinite Reynolds numbers, a persistent $k^{-3/2}$ scaling of the TKE spectrum as well as a $k^{-3/2}$ spectrum with a $k^{-5/3}$ spectrum at high wavenumbers that covers more and more of the spectrum as time proceeds. Furthermore, the same authors (Thornber *et al.* 2011) found (depending on the initial conditions) a $k^{-5/3}$ or a k^{-2} scaling range after

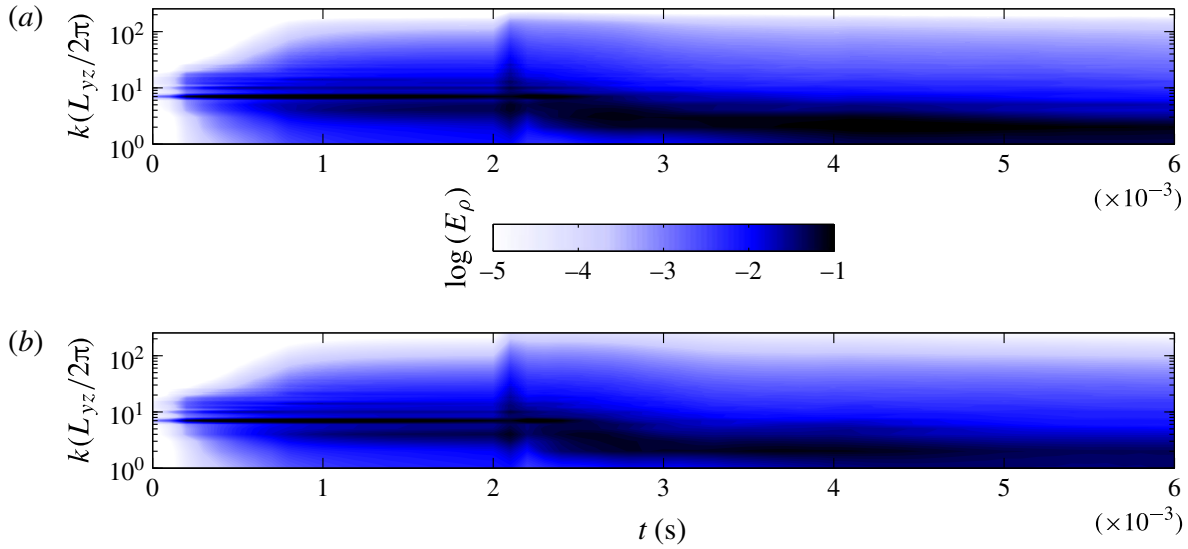

FIGURE 12. (Colour online) Power spectra of density from (*a*) Miranda and (*b*) INCA as a function of wavenumber $k(L_{yz}/2\pi)$ and time. The data are taken from the finest grid (512).

re-shock. Long after re-shock, however, these scalings return to a $k^{-3/2}$ scaling at intermediate scales and to a $k^{-5/3}$ scaling at high wavenumbers, close to the cut-off wavenumber. The authors evaluated the radial spectra either in the centre of the mixing zone or averaged over a fixed number of yz planes within the mixing zone. A different scaling behaviour was observed by Hill *et al.* (2006) and Lombardini *et al.* (2012), who found in their multicomponent LES at finite Reynolds numbers a $k^{-5/3}$ scaling in the centre of the mixing zone, whereas Cohen *et al.* (2002) found a $k^{-6/5}$ scaling range for the single-shock RMI averaged over four transverse slices within the mixing zone. In a recent experimental investigation of a shock-accelerated shear layer, Weber *et al.* (2012) showed a $k^{-5/3}$ inertial range followed by an exponential decay in the dissipation range of the scalar spectrum. This result was numerically reproduced by Tritschler *et al.* (2013*a*). Here, the authors averaged over a predefined IMZ.

All spectra shown in this section are radial spectra with a radial wavenumber that is defined as $k = (k_y^2 + k_z^2)^{1/2}$. The radial spectra are averaged over all yz planes within the IMZ in the x direction that satisfy the condition in (4.5).

The radial power spectra of density are plotted in figure 13, where 13(*a*,*b*) show the spectra before and 13(*c*,*d*) after re-shock. The power spectra of density and mass fraction concentration (not shown) show a close correlation, even though they are not directly related, as the mass fractions are constrained to be between zero and one.

Before re-shock, the dominant initial modes slowly break down and redistribute energy to smaller scales. Re-shock causes additional baroclinic vorticity production with inverse sign that results in a destruction process of the pre-shock structures (see also figure 12). This process in conjunction with a vorticity deposition that is one order of magnitude larger than the pre-shock deposition leads to rapid formation of complex disordered structures, which eliminates most of the memory of the initial interface perturbation, as can be seen in figures 12–14. Schilling, Latini & Don (2007) reported that during re-shock vorticity production is strongly enhanced along the interface where density gradients and misalignment of pressure and density gradients is largest. The vorticity deposited by the re-shock transforms bubbles into spikes and vice versa, which subsequently results in more complex and highly disordered structures.

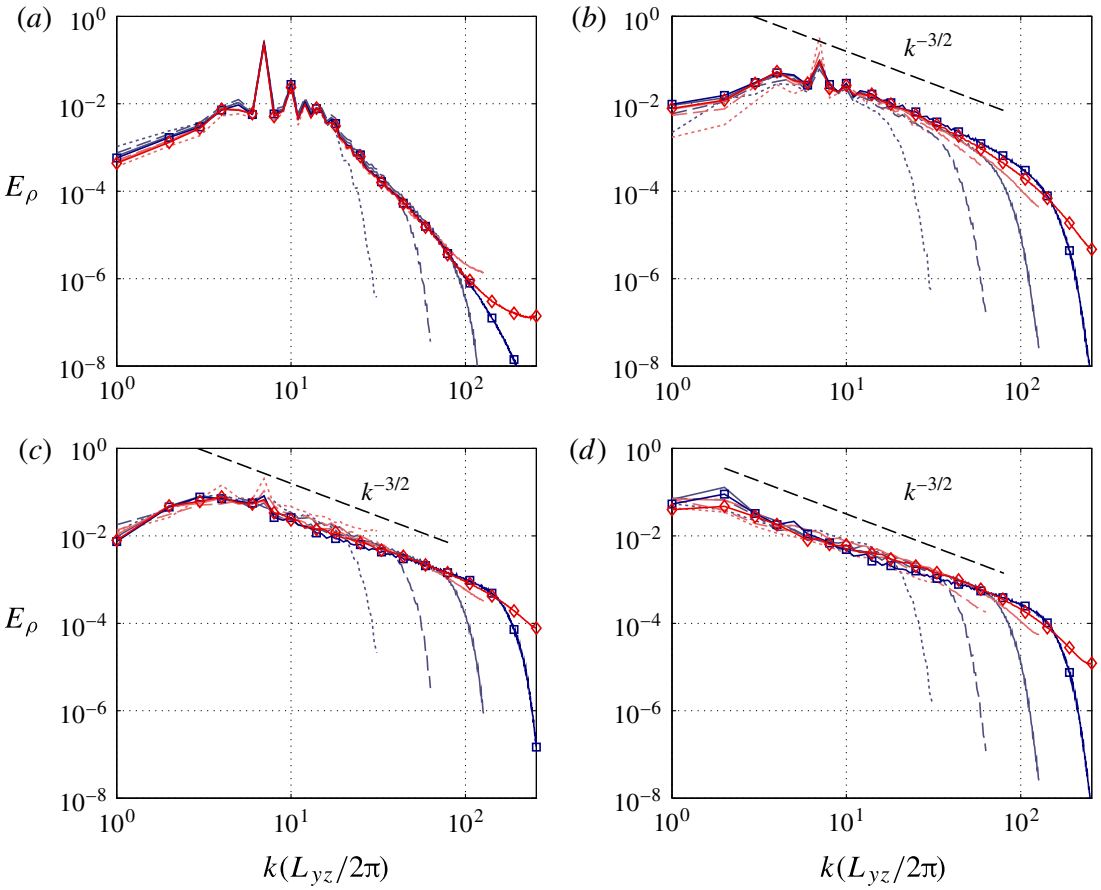

FIGURE 13. (Colour online) Power spectra of density from Miranda (dark grey; blue online) and INCA (light grey; red online) before re-shock at (*a*) $t = 0.5$ ms and (*b*) $t = 2$ ms and after re-shock at (*c*) $t = 2.5$ ms and (*d*) $t = 6$ ms. The different resolutions are represented as dotted line (64), dashed line (128), solid line (256) and solid line with open squares for Miranda and open diamonds for INCA (512).

At late times the power spectra of density appear to be more shallow than $k^{-3/2}$, and rather approach $k^{-6/5}$, as was found by Cohen *et al.* (2002). The smallest length scale in scalar turbulence is the Batchelor scale. For isotropic turbulence and Schmidt numbers of order unity, it has the same order of magnitude as the Kolmogorov microscale $\lambda_B \approx \eta$. Therefore, the TKE spectra are closely correlated with the scalar power spectra. Figure 14 shows the spectra of TKE before and after re-shock. The significant increase in TKE is mainly due to the interaction of the enhanced small-scale structures with comparatively steep density gradients and the reflected shock wave. The re-shock at $t \approx 2$ ms leads to a self-similar lifting of the spectrum (see figure 14). The destruction process of the vortical structures initiated by the re-shock leads to the formation of small scales, which rapidly remove the memory of the initial condition. The intense fluctuating velocity gradients past re-shock are rapidly smoothed out by viscous stresses. This results in a fast decay of the TKE following the first ≈0.5 ms after re-shock (see figures 8 and 14*c*,*d*).

The sharp drop-off of the spectral energy in figures 13 and 14 in the Miranda data at high wavenumbers is due to the filtering operator of the numerical method. Opposite behaviour, that is, an increase of spectral energy at the highest wavenumbers, is observed for the less dissipative INCA code, where the spurious behaviour at the non-resolved scales is mainly dispersive.

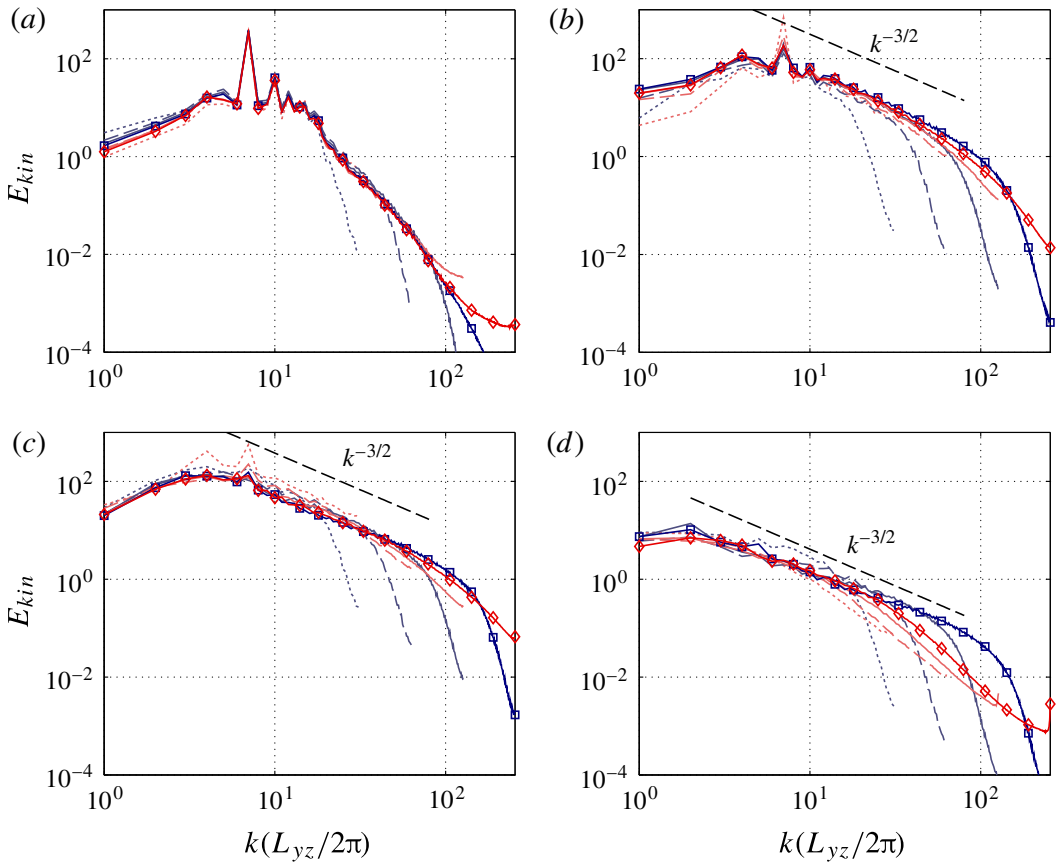

FIGURE 14. (Colour online) Spectra of TKE from Miranda (dark grey; blue online) and INCA (light grey; red online) before re-shock at (*a*) $t = 0.5$ ms and (*b*) $t = 2$ ms and after re-shock at (*c*) $t = 2.5$ ms and (*d*) $t = 6$ ms. The different resolutions are represented as dotted line (64), dashed line (128), solid line (256) and solid line with open squares for Miranda and open diamonds for INCA (512).

The scaled TKE spectra $kE_{kin}(k)$ represent the effective energy contributed by each mode. Artifacts of the initial conditions still exist immediately before re-shock at $t = 2.0$ ms, as can be seen in figure 15(*a*), where most energy is contained at mode $k(L_{yz}/2\pi) = 7$. At re-shock, baroclinic vorticity is deposited at the interface and the energy-containing wavenumber range immediately widens as vortex stretching and tangling introduce new scales and higher vorticity. This broader profile is plotted in figure 15(*b*), which clearly shows that the relative difference between the imposed initial length scale $k(L_{yz}/2\pi) = 7$ and the remaining length scales (both larger and smaller) is vanishing. Indeed, as the mixing layer fully transitions to turbulence, the flow reaches a self-similar state where the memory of initial perturbations is lost.

The spectra of the scalar dissipation rate χ in figure 16 quickly build up in the cut-off wavenumber range after the initial shock impact (see figure 16*b*). After re-shock and at late time (see figure 16*c*,*d*), the inertial subrange broadens to wavenumbers where numerical dissipation damps out structures. The inertial range is observed to scale with $k^{1/2}$ after re-shock, which is consistent with the $k^{-3/2}$ scaling observed for E_ρ and E_{kin}. For the resolved wavenumbers, there is good agreement between both codes at the finest two resolutions. Differences observed in figure 16(*b*) are also reflected in figures 7 and 11. A sharper material interface and the associated segregation of the fluids lead to a higher scalar dissipation rate (χ), whereas at late

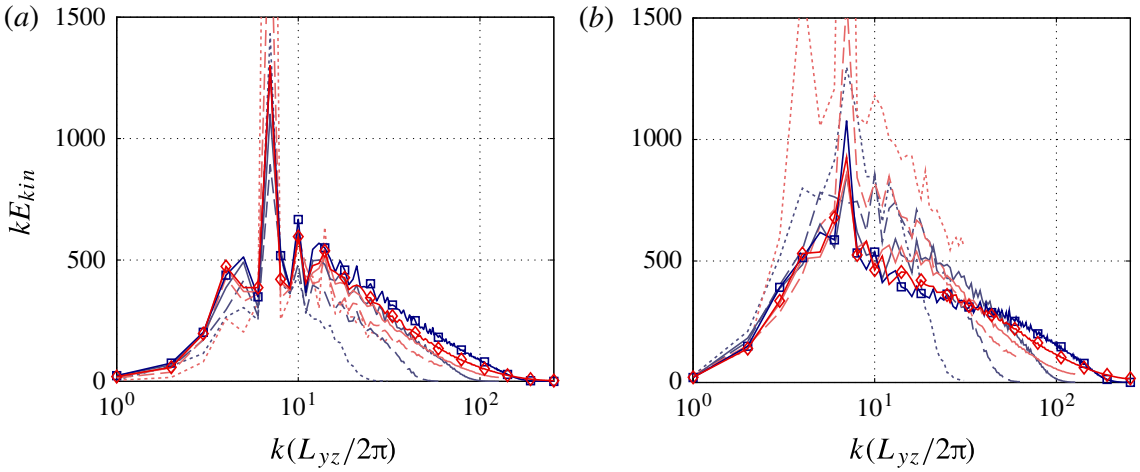

FIGURE 15. (Colour online) Scaled spectra of TKE from Miranda (dark grey; blue online) and INCA (light grey; red online) before re-shock at (*a*) $t = 2$ ms and (*b*) $t = 2.5$ ms. The different resolutions are represented as dotted line (64), dashed line (128), solid line (256) and solid line with open squares for Miranda and open diamonds for INCA (512).

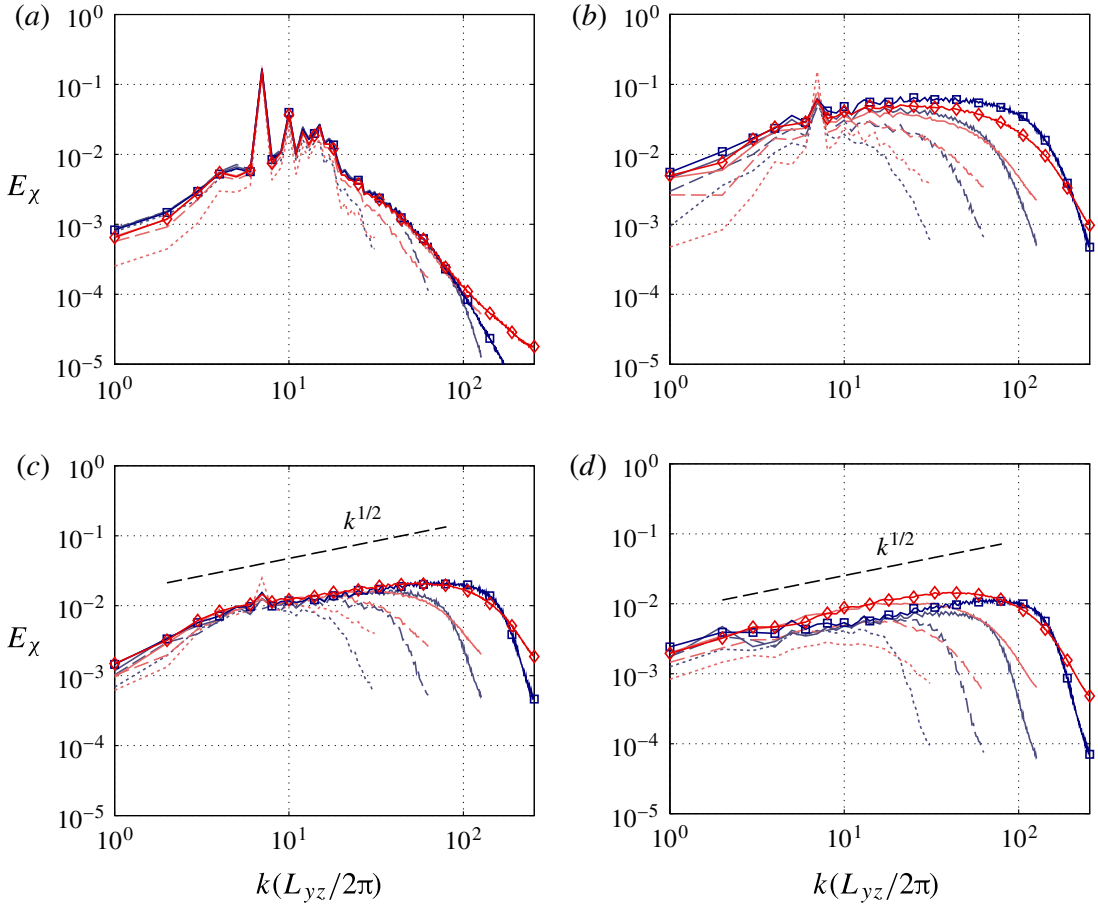

FIGURE 16. (Colour online) Spectra of scalar dissipation rate from Miranda (dark grey; blue online) and INCA (light grey; red online) before re-shock at (*a*) $t = 0.5$ ms and (*b*) $t = 2$ ms and after re-shock at (*c*) $t = 2.5$ ms and (*d*) $t = 6$ ms. The different resolutions are represented as dotted line (64), dashed line (128), solid line (256) and solid line with open squares for Miranda and open diamonds for INCA (512).

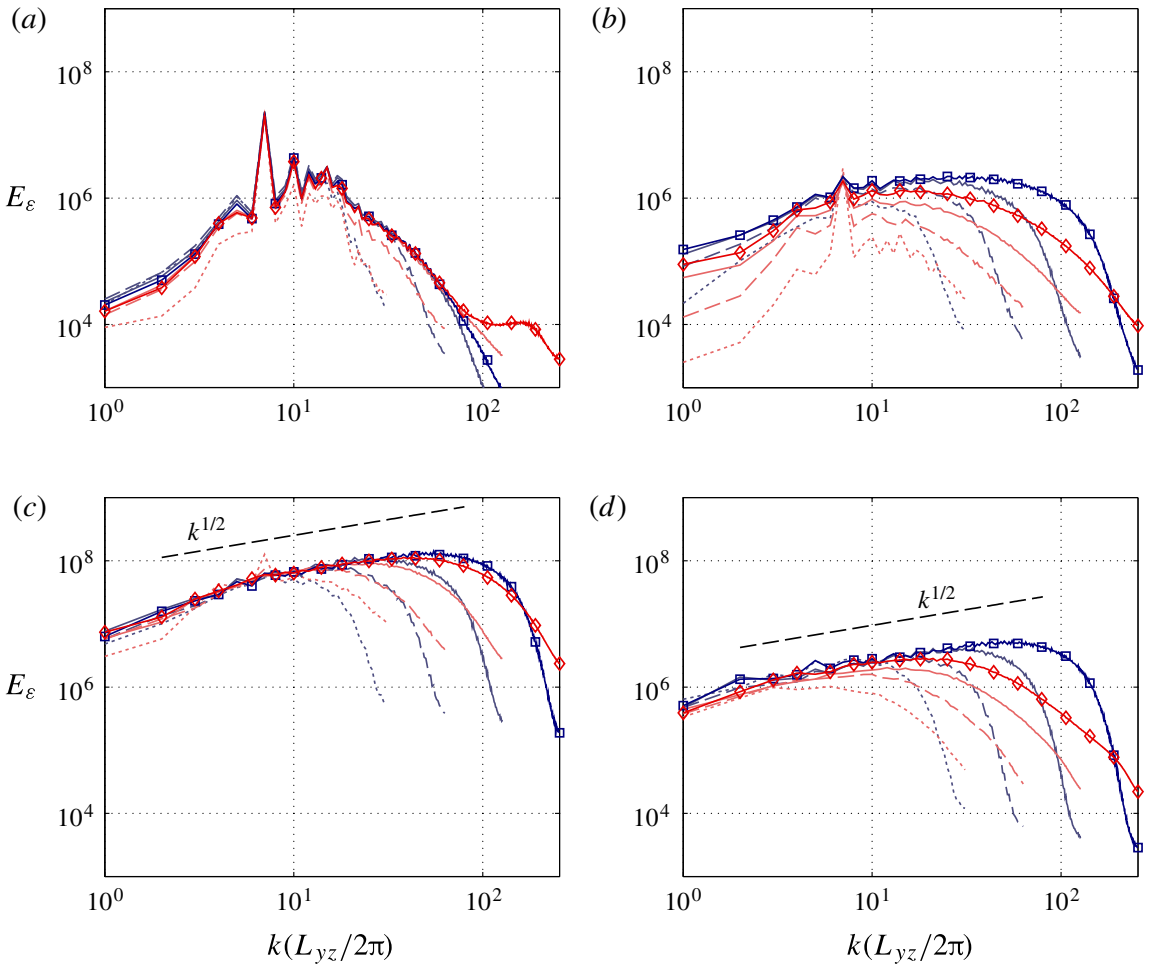

FIGURE 17. (Colour online) Spectra of enstrophy from Miranda (dark grey; blue online) and INCA (light grey; red online) before re-shock at (*a*) $t = 0.5$ ms and (*b*) $t = 2$ ms and after re-shock at (*c*) $t = 2.5$ ms and (*d*) $t = 6$ ms. The different resolutions are represented as dotted line (64), dashed line (128), solid line (256) and solid line with open squares for Miranda and open diamonds for INCA (512).

times the difference in the scalar dissipation rate does not significantly influence the mixing measures $\langle b \rangle_{xyz}$ and Θ.

Larger quantitative differences are observed in the power spectra of enstrophy shown in figure 17. Immediately after either of the shock–interface interactions, the quantitative agreement between the predicted enstrophy levels is excellent (see figure 17*a*,*c*). The observed scalings of the inertial range following re-shock are predicted consistently and agree with the inertial range scalings for the scalar dissipation rate $k^{1/2}$. However, the temporal decay of the small-scale enstrophy is significantly different for either code, as can be seen immediately before re-shock and long after re-shock in figures 17(*b*) and (*d*), respectively.

In isotropic homogeneous turbulence, the scaled spectra of the enstrophy (see figure 18) has a single peak at the wavenumber where the dissipation range begins. Therefore, under grid refinement this peak will shift to higher wavenumbers and magnitudes as smaller scales are captured. The peak at $k(L_{yz}/2\pi) = 7$ is associated with the initial perturbation and disappears after re-shock as the flow becomes turbulent (see figure 18). Good agreement for lower wavenumbers is observed between codes and resolutions. Larger differences are observed at high wavenumbers, where

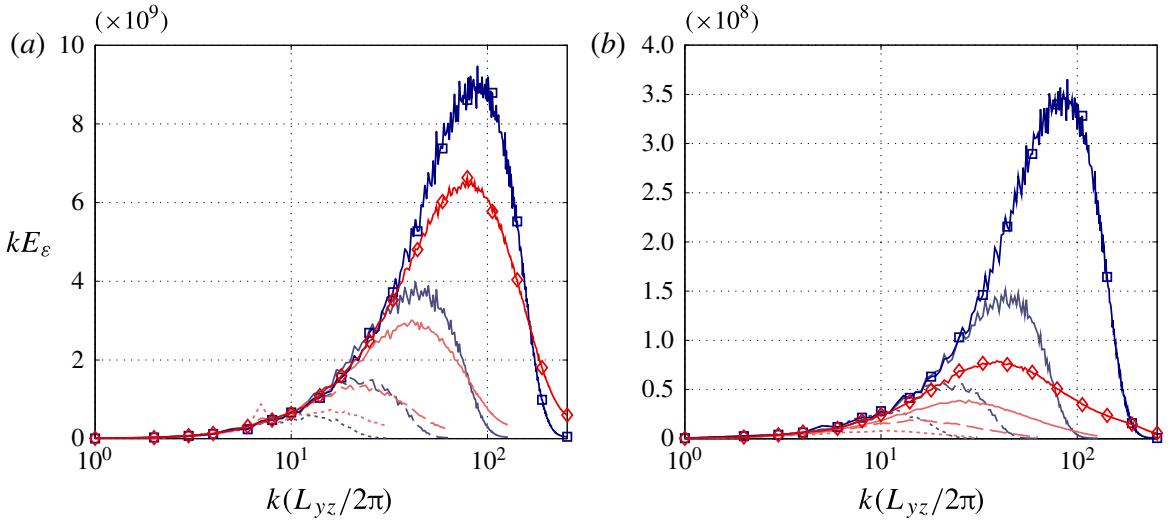

FIGURE 18. (Colour online) Scaled spectra of enstrophy from Miranda (dark grey; blue online) and INCA (light grey; red online) after re-shock at (*a*) $t = 2.5$ ms and (*b*) $t = 6$ ms. The different resolutions are represented as dotted line (64), dashed line (128), solid line (256) and solid line with open squares for Miranda and open diamonds for INCA (512).

the dependence on numerical dissipation is greatest. At $t = 2.5$ ms the peak in the scaled enstrophy spectra is at $k(L_{yz}/2\pi) \approx 85$ for both codes at the highest resolution. Later, at $t = 6.0$ ms this peak has shifted to $k(L_{yz}/2\pi) \approx 40$ in INCA, whereas in Miranda there is no apparent shift, although both have substantially decayed in magnitude.

As RMI is a pure decay process after re-shock, differences in the numerical approach become most apparent at late times. The numerical models of this study predict different turbulence decay rates, as is evident from differences in the enstrophy spectrum (figures 17 and 18) and in TKE (figure 9). The differences in enstrophy (ε) and scalar dissipation rate (χ) have a qualitative effect that becomes apparent in the fine-scale structures of figure 5 at $t = 6$ ms. Although INCA resolved less scales with smaller enstrophy levels, it does resolve steeper mass fraction gradients, which is reflected in the higher χ and higher levels of E_χ. Although it is unclear which dissipation rate (scalar or kinetic) has most effect on the mixing process, both are important (Dimotakis 2000).

4.4. *Probability density functions*

The bin size for computing the discrete probability density function (p.d.f.) is defined as $\Delta\varphi = [\varphi_{max} - \varphi_{min}]/N_b$ for a quantity $\varphi(x, y, z, t)$. The number of bins for all quantities and all grid resolutions is $N_b = 64$. Each discrete value of φ is distributed into the bins, yielding a frequency N_k for each bin. The p.d.f. is then defined by

$$P_k(\varphi, t) = \frac{N_k}{\Delta\varphi N}, \tag{4.13}$$

such that $\sum_{k=1}^{N_k} P_k \Delta\varphi = 1$, with N as the total number of cells in the IMZ that fall within the range $\varphi_{min} \leqslant \varphi \leqslant \varphi_{max}$. The limits φ_{max} and φ_{min} are held constant for all resolutions and times.

The p.d.f. of the heavy-gas mass fraction is constrained to be $0.1 \leqslant Y_{HG} \leqslant 0.9$. Figure 19 shows the p.d.f. at times before re-shock ($t = 0.5$ ms, $t = 2$ ms) and

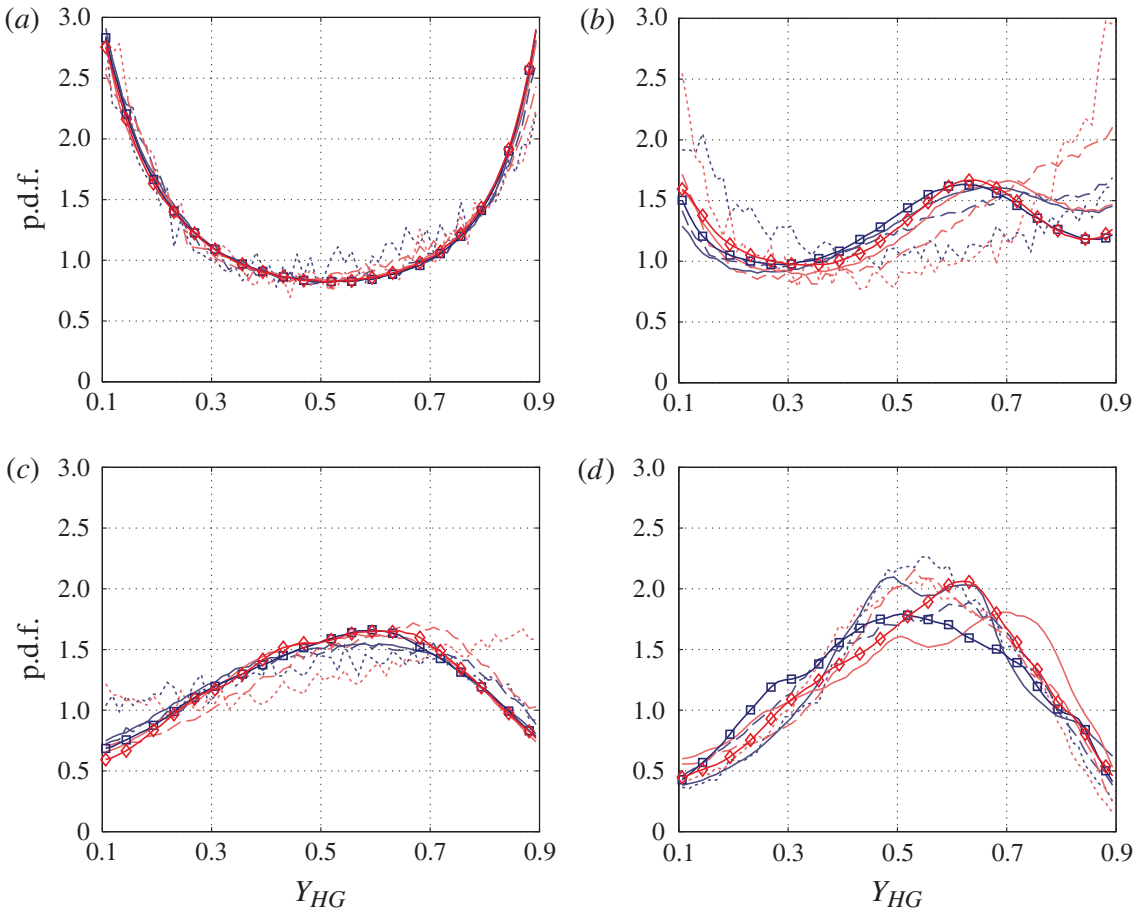

FIGURE 19. (Colour online) Probability density function of Y_{HG} from Miranda (dark grey; blue online) and INCA (light grey; red online) before re-shock at (*a*) $t = 0.5$ ms and (*b*) $t = 2$ ms and after re-shock at (*c*) $t = 2.5$ ms and (*d*) $t = 6$ ms. The different resolutions are represented as dotted line (64), dashed line (128), solid line (256) and solid line with open squares for Miranda and open diamonds for INCA (512).

following re-shock ($t = 2.5$ ms, $t = 6$ ms). From figure 19(*a*) it is evident that at early times following the initial shock–interface interaction the IMZ consists mostly of segregated fluid, as the large peaks at the p.d.f. bounds indicate. Before re-shock, inter-species mixing is largely dominated by the inviscid linear and nonlinear entrainment. Molecular diffusion processes have not yet had enough time to act (see figure 19*b*). Following re-shock, a fundamental change in the p.d.f. of Y_{HG} ($P(Y_{HG})$) is observed (see figure 19*c*,*d*). The additional vorticity deposited by the re-shock leads to rapid formation of small and very intense vortical structures that lead to very effective mixing and destruction of the initial interface perturbation. The p.d.f. takes a unimodal form at $t = 2.5$ ms, as also reported by Hill *et al.* (2006). The peak value, however, is not as well correlated with the average value of the mixture mass fraction as was reported by Hill *et al.* (2006). With our data the peak value is slightly shifted towards the heavy-gas side centred around $Y_{HG} \approx 0.6$. The degree of convergence between codes and resolutions is reassuring at $t = 2.5$ ms. Note that $P(Y_{HG})$ is a very sensitive measure of the light–heavy gas mixing.

The rarefaction wave at $t \approx 3.2$ ms does not significantly contribute to the mixing, as it is not as pronounced as found in comparable investigations (Hill *et al.* 2006; Grinstein *et al.* 2011). Long after re-shock the mixing process continues, which is reflected in narrower tails of $P(Y_{HG})$. The peak value of Y_{HG} predicted by Miranda now

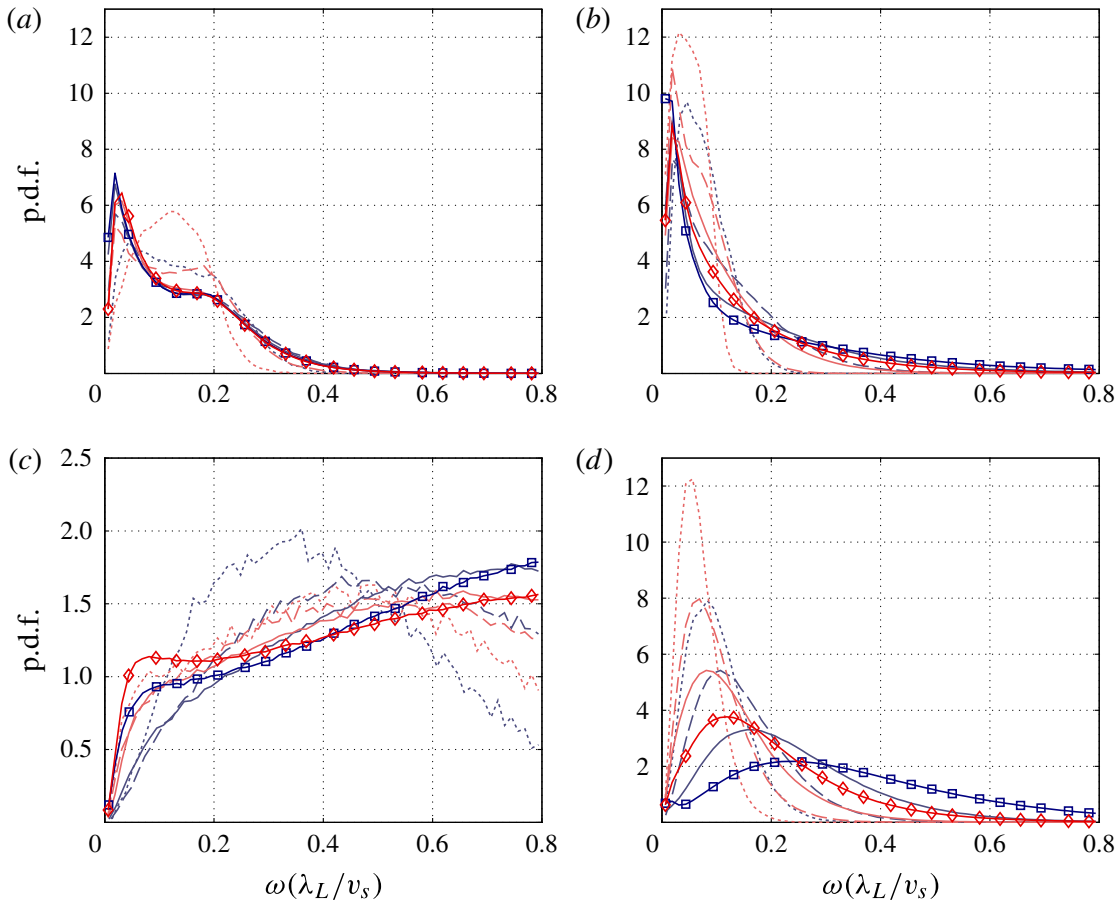

FIGURE 20. (Colour online) Probability density function of $\omega(\lambda_L/v_s)$ from Miranda (dark grey; blue online) and INCA (light grey; red online) before re-shock at (*a*) $t=0.5$ ms and (*b*) $t=2$ ms and after re-shock at (*c*) $t=2.5$ ms and (*d*) $t=6$ ms. The different resolutions are represented as dotted line (64), dashed line (128), solid line (256) and solid line with open squares for Miranda and open diamonds for INCA (512).

coincides with the average value of the mixture mass fraction. In the INCA results, this value remains slightly shifted towards the heavy-gas side. However, the bimodal character of $P(Y_{HG})$ reported by Hill *et al.* (2006), who used air–SF_6 as light–heavy gases, is not observed on the finest grid. Despite the strong mixing past re-shock the turbulent mixing zone remains inhomogeneous until the end of the simulation time, which makes the observed p.d.f. very sensitive to their location of evaluation within the mixing layer.

The p.d.f. of the normalised vorticity is constrained between $0 \leqslant \tilde{\omega} \leqslant 0.8$ with $\tilde{\omega} = \omega(\lambda_L/v_s)$, where v_s is the initial shock velocity and λ_L is a characteristic length scale of the perturbations taken as $\lambda_L = L_{yz}/\tilde{k}_{max}$, where L_{yz} is the width of the domain in the transverse direction and $\tilde{k}_{max} = k_{max}(L_{yz}/2\pi) = 16$.

Figure 20 shows the p.d.f. of the normalised vorticity $P(\tilde{\omega})$. Before re-shock, mixing is driven by weak large-scale vortices (see figure 20*a*,*b*). Following re-shock, however, structures with very intense vorticity develop with a dual-mode shape in $P(\tilde{\omega})$ at $t=2.5$ ms on the finest grid. The early times after the second shock–interface interaction are again consistently predicted by both codes (figure 20*c*). Nevertheless, we observe larger differences for $P(\tilde{\omega})$ at $t=6$ ms. The peak and distribution of $P(\tilde{\omega})$ from Miranda are shifted towards larger values of $\tilde{\omega}$ as compared to INCA. This supports the previous observation that the vorticity decay is affected by the numerical

approach. The difference in the vorticity intensity observed in figure 20, however, does not lead to noticeable differences for the integral mixing measures shown in figures 7(*a*) and 11 or for the integral length scale in figure 6.

5. Conclusion

We have investigated the shock-induced turbulent mixing between a light (N_2, O_2) and heavy (SF_6, acetone) gas in highly resolved numerical simulations. The mixing was initiated by the interaction of a $Ma = 1.5$ shock wave with a deterministic multimode interface. After the initial baroclinic vorticity deposition, the shock wave is reflected at the opposite adiabatic wall boundary. The reflected shock wave impacts the interface (re-shock) and deposits additional vorticity with enstrophy that is more than two orders of magnitude larger than that of the initial vorticity deposition. The transformation of spike structures into bubbles and vice versa in conjunction with a large increase in vorticity results in the formation of disordered structures which eliminate most of the memory of the initial interface perturbation.

A proposed standardised initial condition for simulating the RMI has been assessed by two different numerical approaches, Miranda and INCA, over a range of grid resolutions. The deterministic interface definition allows for spectrally identical initial conditions for different numerical models and grid resolutions. A direct comparison shows that larger energy-containing scales are in excellent agreement. Different subgrid-scale regularisations affect marginally resolved flow scales, but allow for a clear identification of a resolved scale range that is unaffected by the subgrid-scale regularisation.

Mixing widths are nearly identical between the two approaches at the highest resolution. At lower resolutions, the solutions differ, and we found a minimum resolution of $\sim$400 μm to be necessary in order to produce reasonable late-time results. The initial mixing zone growth rate scaled with $\delta_x \sim t^{7/12}$, whereas long after re-shock the predicted growth rate was $\sim t^{2/7}$. The decay of TKE was also found to be consistent and in good agreement between the approaches. The decay scaled with TKE $\sim t^{-10/7}$ at late times, which corresponds to a growth-rate scaling of the energy-containing eddies of $\sim t^{2/7}$. The agreement in the large scales of the solution between the two approaches is striking and has not been observed before.

Previous work on three-dimensional LES of RMI has examined numerical dependence only indirectly. For example, Thornber *et al.* (2010) performed a code comparison of single-shock RMI. However, the initialisation was different for the two codes and the purpose was not to quantify the effect of different numerical methods. Accordingly, the comparison of results at different resolutions for mean, spectral and gradient-based quantities was limited. With the current work, we have presented for the first time a comprehensive quantitative analysis of numerical effects on RMI.

Our results conclusively show that the large scales are in excellent agreement for the two methods. Differences are observed in the representation of the material interface. We conclude that the numerical challenge, prior to re-shock, is to predict the large-scale nonlinear entrainment and the associated interface sharpening. Under shear and strain, the interface steepens and eventually becomes under-resolved with a thickness defined by the resolution limit of the numerical scheme. Therefore, the saturation of the interface thickness by the numerical method occurs later as the grid is refined. The molecular mixing fraction reached an asymptotic limit as $\Theta \approx 0.85$ after re-shock, which was already correctly calculated on grid resolutions of $\sim$400 μm. The yz plane averaged anisotropy $\langle a \rangle_{yz}$ revealed that the mixing zone

exhibits a stratified anisotropy distribution with lower anisotropy on the heavy-gas side and higher anisotropy on the light-gas side. Moreover, the volume-averaged anisotropy $\langle a\rangle_{xyz}$ approached an asymptotic limit of $\langle a\rangle_{xyz} \approx 0.04$, implying that the fluctuating velocity component u'' remains the dominant component even after re-shock and that no full recovery of isotropy of the mixing zone is obtained. The density self-correlation has been investigated in order to better understand the mixing inhomogeneity in the mixing zone. The volume-averaged density-specific volume correlation $\langle b\rangle_{xyz}$ showed that the re-shock significantly increases mixing homogeneity approaching a value of $\langle b\rangle_{xyz} \approx 0.13$ at the latest time.

The spectra demonstrate a broad range of resolved scales, which are in very good agreement. Data also show that differences exist in the small-scale range. The frequency dependence of the velocity and density fluctuations shows the existence of an inertial subrange and that the two approaches agree at lower frequencies. The observed spectral scalings were consistent among the methods with $k^{-3/2}$.

Quantities that are gradient-dependent and therefore more sensitive to small scales, such as the scalar dissipation rate and enstrophy, exhibit stronger dependence on numerical method and grid resolution. The flow field shows visual differences for the fine-scale structures at late times. The tenth-order compact scheme and the explicit filtering and artificial fluid properties used in Miranda resolved more small scales in TKE and enstrophy, whereas the sixth-order WENO-based scheme used in INCA resolves more of the small-scale scalar flow features as observed in the spectra of density and scalar dissipation rate. This result is somewhat intuitive given the numerics of the two codes. High-order compact methods are capable of resolving higher modes than explicit finite difference methods (Lele 1992). Given that the artificial shear viscosity in Miranda has only a small effect on the solution compared to the effect of the eighth-order filter, the primary difference, we conclude, of the resolving power between methods is due to the difference in order of accuracy and modified wavenumber profiles between the schemes. The compact finite difference method with high-order filtering appears to capture a broader range of dynamic scales at late times.

The p.d.f. statistics of heavy-gas mass fraction Y_{HG} revealed that the IMZ remains inhomogeneous until the end of the simulation and that the peak probability is centred around $Y_{HG} \approx 0.6$ and thus is slightly shifted towards the heavy-gas side. Although the overall quantitative agreement was very good, the p.d.f. of the vorticity showed larger differences once intense small-scale vortical structures exist. The decay of vorticity differs accordingly between the numerical methods.

Acknowledgements

The authors gratefully acknowledge the Gauss Centre for Supercomputing e.V. (GCS, www.gauss-centre.eu) for providing computing time on the GCS Supercomputer SuperMUC at Leibniz Supercomputing Centre (LRZ, www.lrz.de). This work was performed under the auspices of the US Department of Energy by Lawrence Livermore National Laboratory under contract number DE-AC52-07NA27344. V.K.T. gratefully acknowledges the support of the TUM Graduate School. B.J.O. thanks A. Cook and W. Cabot for valuable insight and for use of the Miranda code.

Appendix A. Multicomponent mixing rules

The specific heat capacity of species i is found by

$$c_{p,i} = \frac{\gamma_i}{\gamma_i - 1} R_i, \quad \text{with } R_i = \frac{R_{univ}}{M_i}, \tag{A 1}$$

where γ_i is the ratio of specific heats. The ratio of specific heats of the mixture follows as

$$\bar{\gamma} = \frac{\overline{c_p}}{\overline{c_p} - \bar{R}}, \quad \text{with } \overline{c_p} = \sum_i^N Y_i c_{p,i}, \tag{A 2}$$

where Y_i is the mass fraction of species i and $\bar{R}$ is the specific gas constant of the mixture with $\bar{R} = R_{univ}/\bar{M}$. The molar mass of the mixture is given by

$$\bar{M} = \left(\sum_i^N \frac{Y_i}{M_i} \right)^{-1}. \tag{A 3}$$

For the gas mixture, Dalton's law $p = \sum_i p_i$ will be valid with $p_i = \rho R_i T$. The mixture viscosity $\bar{\mu}$ and the mixture thermal conductivity $\bar{\kappa}$ are calculated from (Reid, Pransuitz & Poling 1987)

$$\bar{\mu} = \frac{\sum_{i=1}^N \mu_i Y_i / M_i^{1/2}}{\sum_{i=1}^N Y_i / M_i^{1/2}}, \quad \bar{\kappa} = \frac{\sum_{i=1}^N \kappa_i Y_i / M_i^{1/2}}{\sum_{i=1}^N Y_i / M_i^{1/2}}. \tag{A 4a,b}$$

The effective binary diffusion coefficients (diffusion of species i into all other species) are approximated as (Ramshaw 1990)

$$D_i = (1 - X_i) \left(\sum_{i \neq j}^N \frac{X_j}{D_{ij}} \right)^{-1}, \tag{A 5}$$

where X_i is the mole fraction of species i. Equation (A 5) ensures that the inter-species diffusion fluxes balance to zero.

Appendix B. Molecular mixing rules

The viscosity of a pure gas is calculated from the Chapman–Enskog model (Chapman & Cowling 1990)

$$\mu_i = 2.6693 \times 10^{-6} \frac{\sqrt{M_i T}}{\Omega_{\mu,i} \sigma_i^2}, \tag{B 1}$$

where σ_i is the collision diameter and $\Omega_{\mu,i}$ is the collision integral,

$$\Omega_{\mu,i} = A(T_i^*)^B + C \exp(D T_i^*) + E \exp(F T_i^*), \tag{B 2}$$

with $A = 1.161\,45$, $B = -0.148\,74$, $C = 0.524\,87$, $D = -0.7732$, $E = 2.161\,78$ and $F = -2.437\,87$ and where $T_i^* = T/(\epsilon/k)_i$. Here $(\epsilon/k)_i$ is the Lennard-Jones energy parameter, with ϵ the minimum of the Lennard-Jones potential and k the Boltzmann constant.

The thermal conductivity of species i is defined by

$$\kappa_i = c_{p,i} \frac{\mu_i}{Pr_i}, \tag{B 3}$$

with Pr_i the species-specific Prandtl number.

Property	Nitrogen	Oxygen	SF_6	Acetone
$(\epsilon/k)_i$ (K)	82.0	102.6	212.0	458.0
σ_i (Å)	3.738	3.48	5.199	4.599
M_i (g mol^{-1})	28.0140	31.9990	146.0570	58.0805
γ_i	1.4	1.4	1.1	1.1
Pr_i	0.72	0.72	0.8	0.8

TABLE 2. Molecular properties of nitrogen, oxygen, SF_6 and acetone.

The mass diffusion coefficient of a binary mixture is calculated from the empirical law (Reid *et al.* 1987)

$$D_{ij} = \frac{0.0266}{\Omega_{D,ij}} \frac{T^{3/2}}{p\sqrt{M_{ij}}\sigma_{ij}^2}, \tag{B 4}$$

with the collision integral for diffusion

$$\Omega_{D,ij} = A(T_{ij}^*)^B + C\exp(DT_{ij}^*) + E\exp(FT_{ij}^*) + G\exp(HT_{ij}^*), \tag{B 5}$$

where $T_{ij}^* = T/T_{\epsilon_{ij}}$ and $A = 1.060\,36$, $B = -0.1561$, $C = 0.193\,00$, $D = -0.476\,35$, $E = 1.035\,87$, $F = -1.529\,96$, $G = 1.764\,74$, $H = -3.894\,11$ and

$$M_{ij} = \frac{2}{\dfrac{1}{M_i} + \dfrac{1}{M_j}}, \tag{B 6a}$$

$$\sigma_{ij} = \frac{\sigma_i + \sigma_j}{2}, \tag{B 6b}$$

$$T_{\epsilon_{ij}} = \sqrt{\left(\frac{\epsilon}{k}\right)_i \left(\frac{\epsilon}{k}\right)_j}. \tag{B 6c}$$

The molecular properties of all species in the present study are given in table 2.

REFERENCES

AGLITSKIY, Y., VELIKOVICH, A. L., KARASIK, M., METZLER, N., ZALESAK, S. T., SCHMITT, A. J., PHILLIPS, L., GARDNER, J. H., SERLIN, V., WEAVER, J. L. & OBENSCHAIN, S. P. 2010 Basic hydrodynamics of Richtmyer–Meshkov-type growth and oscillations in the inertial confinement fusion-relevant conditions. *Phil. Trans. R. Soc. Lond.* A **368** (1916), 1739–1768.

ALMGREN, A. S., BELL, J. B., RENDLEMAN, C. A. & ZINGALE, M. 2006 Low Mach number modeling of type Ia supernovae I. Hydrodynamics. *Astrophys. J.* **637**, 922–936.

ARNETT, D. 2000 The role of mixing in astrophysics. *Astrophys. J. Suppl.* **127**, 213–217.

ARNETT, W. D., BAHCALL, J. N., KIRSHNER, R. P. & STANFORD, E. W. 1989 Supernova 1987a. *Annu. Rev. Astron. Astrophys.* **27**, 629–700.

BALAKUMAR, B. J., ORLICZ, G. C., RISTORCELLI, J. R., BALASUBRAMANIAN, S., PRESTRIDGE, K. P. & TOMKINS, C. D. 2012 Turbulent mixing in a Richtmyer–Meshkov fluid layer after reshock: velocity and density statistics. *J. Fluid Mech.* **696**, 67–93.

BALASUBRAMANIAN, S., ORLICZ, G. C. & PRESTRIDGE, K. P. 2013 Experimental study of initial condition dependence on turbulent mixing in shock-accelerated Richtmyer–Meshkov fluid layers. *J. Turbul.* **14** (3), 170–196.

BALASUBRAMANIAN, S., ORLICZ, G. C., PRESTRIDGE, K. P. & BALAKUMAR, B. J. 2012 Experimental study of initial condition dependence on Richtmyer–Meshkov instability in the presence of reshock. *Phys. Fluids* **24**, 034103.

BATCHELOR, G. K. & PROUDMAN, I. 1956 The large-scale structure of homogeneous turbulence. *Phil. Trans. R. Soc. Lond.* A **248**, 369–405.

BESNARD, D., HARLOW, F. H., RAUENZAHN, R. M. & ZEMACH, C. 1992 Turbulence transport equations for variable-density turbulence and their relationship to two-field models. *Recon Tech. Rep.* No. 92, 33159. NASA STI.

BROUILLETTE, M. 2002 The Richtmyer–Meshkov instability. *Annu. Rev. Fluid Mech.* **34**, 445–468.

CABOT, W. H. & COOK, A. W. 2006 Reynolds number effects on Rayleigh–Taylor instability with possible implications for type Ia supernovae. *Nat. Phys.* **2** (8), 562–568.

CHAPMAN, S. & COWLING, T. G. 1990 *The Mathematical Theory of Non-Uniform Gases: An Account of the Kinetic Theory of Viscosity*. Cambridge University Press.

COHEN, R. H., DANNEVIK, W. P., DIMITS, A. M., ELIASON, D. E., MIRIN, A. A., ZHOU, Y., PORTER, D. H. & WOODWARD, P. R. 2002 Three-dimensional simulation of a Richtmyer–Meshkov instability with a two-scale initial perturbation. *Phys. Fluids* **14** (10), 3692–3709.

COOK, A. W. 2007 Artificial fluid properties for large-eddy simulation of compressible turbulent mixing. *Phys. Fluids* **19** (5), 055103.

COOK, A. W. 2009 Enthalpy diffusion in multicomponent flows. *Phys. Fluids* **21**, 055109.

COOK, A. W., CABOT, W. & MILLER, P. L. 2004 The mixing transition in Rayleigh–Taylor instability. *J. Fluid Mech.* **511**, 333–362.

DIMONTE, G., FRERKING, C. E. & SCHNEIDER, M. 1995 Richtmyer–Meshkov instability in the turbulent regime. *Phys. Rev. Lett.* **74**, 4855–4858.

DIMONTE, G. & SCHNEIDER, M. 2000 Density ratio dependence of Rayleigh–Taylor mixing for sustained and impulsive acceleration histories. *Phys. Fluids* **12** (2), 304–321.

DIMOTAKIS, P. E. 2000 The mixing transition in turbulent flows. *J. Fluid Mech.* **409**, 69–98.

DRIKAKIS, D. 2003 Advances in turbulent flow computations using high-resolution methods. *Prog. Aerosp. Sci.* **39** (6–7), 405–424.

DRIKAKIS, D., HAHN, M., MOSEDALE, A. & THORNBER, B. 2009 Large eddy simulation using high-resolution and high-order methods. *Phil. Trans. R. Soc. Lond.* A **367** (1899), 2985–2997.

FEDKIW, R. P., MERRIMAN, B. & OSHER, S. 1997 High accuracy numerical methods for thermally perfect gas flows with chemistry. *J. Comput. Phys.* **190**, 175–190.

GOTTLIEB, S. & SHU, C.-W. 1998 Total variation diminishing Runge–Kutta schemes. *Math. Comput.* **67**, 73.

GRINSTEIN, F. F., GOWARDHAN, A. A. & WACHTOR, A. J. 2011 Simulations of Richtmyer–Meshkov instabilities in planar shock-tube experiments. *Phys. Fluids* **23**, 034106.

HAHN, M., DRIKAKIS, D., YOUNGS, D. L. & WILLIAMS, R. J. R. 2011 Richtmyer–Meshkov turbulent mixing arising from an inclined material interface with realistic surface perturbations and reshocked flow. *Phys. Fluids* **23** (4), 046101.

HILL, D. J., PANTANO, C. & PULLIN, D. I. 2006 Large-eddy simulation and multiscale modelling of a Richtmyer–Meshkov instability with reshock. *J. Fluid Mech.* **557**, 29–61.

HILL, D. J. & PULLIN, D. I. 2004 Hybrid tuned center-difference-WENO method for large eddy simulations in the presence of strong shocks. *J. Comput. Phys.* **194**, 435–450.

HU, X. Y. & ADAMS, N. A. 2011 Scale separation for implicit large eddy simulation. *J. Comput. Phys.* **230** (19), 7240–7249.

HU, X. Y., ADAMS, N. A. & SHU, C.-W. 2013 Positivity-preserving method for high-order conservative schemes solving compressible Euler equations. *J. Comput. Phys.* **242**, 169–180.

HU, X. Y., WANG, Q. & ADAMS, N. A. 2010 An adaptive central-upwind weighted essentially non-oscillatory scheme. *J. Comput. Phys.* **229** (23), 8952–8965.

ISHIDA, T., DAVIDSON, P. A. & KANEDA, Y. 2006 On the decay of isotropic turbulence. *J. Fluid Mech.* **564**, 455–475.

JIMÉNEZ, J., WRAY, A. A., SAFFMAN, P. G. & ROGALLO, R. S. 1993 The structure of intense vorticity in isotropic turbulence. *J. Fluid Mech.* **255**, 65–90.

KENNEDY, C. A., CARPENTER, M. H. & LEWIS, M. R. 2000 Low-storage, explicit Runge–Kutta schemes for the compressible Navier–Stokes equations. *Appl. Numer. Maths* **35** (3), 177–219.

KHOKHLOV, A. M., ORAN, E. S. & THOMAS, G. O. 1999 Numerical simulation of deflagration-to-detonation transition: the role of shock–flame interactions in turbulent flames. *Combust. Flame* **117** (1–2), 323–339.

KOLMOGOROV, A. N. 1941 On the degeneration of isotropic turbulence in an incompressible viscous fluid. *Dokl. Akad. Nauk SSSR* **31**, 538–541.

KOSOVIĆ, B., PULLIN, D. I. & SAMTANEY, R. 2002 Subgrid-scale modeling for large-eddy simulations of compressible turbulence. *Phys. Fluids* **14** (4), 1511–1522.

LAROUTUROU, B. & FEZOUI, L. 1989 On the equations of multi-component perfect or real gas inviscid flow. In *Nonlinear Hyperbolic Problems*, Lecture Notes in Mathematics, vol. 1402, pp. 69–97. Springer.

LELE, S. K. 1992 Compact finite-difference schemes with spectral-like resolution. *J. Comput. Phys.* **103**, 16–42.

LINDL, J. D., MCCRORY, R. L. & CAMPBELL, E. M. 1992 Progress toward ignition and burn propagation in inertial confinement fusion. *Phys. Today* **45** (9), 32–40.

LLOR, A. 2006 Invariants of free turbulent decay, arXiv:physics/0612220.

LOMBARDINI, M., HILL, D. J., PULLIN, D. I. & MEIRON, D. I. 2011 Atwood ratio dependence of Richtmyer–Meshkov flows under reshock conditions using large-eddy simulations. *J. Fluid Mech.* **670**, 439–480.

LOMBARDINI, M., PULLIN, D. I. & MEIRON, D. I. 2012 Transition to turbulence in shock-driven mixing: a Mach number study. *J. Fluid Mech.* **690**, 203–226.

MANI, A., LARSSON, J. & MOIN, P. 2009 Suitability of artificial bulk viscosity for large-eddy simulation of turbulent flows with shocks. *J. Comput. Phys.* **228** (19), 7368–7374.

MESHKOV, E. E. 1969 Instability of the interface of two gases accelerated by a shock wave. *Fluid Dyn.* **4**, 151–157.

MIKAELIAN, K. O. 1989 Turbulent mixing generated by Rayleigh–Taylor and Richtmyer–Meshkov instabilities. *Physica* D **36** (3), 343–357.

OLSON, B. J. & COOK, A. W. 2007 Rayleigh–Taylor shock waves. *Phys. Fluids* **19**, 128108.

OLSON, B. J., LARSSON, J., LELE, S. K. & COOK, A. W. 2011 Non-linear effects in the combined Rayleigh–Taylor/Kelvin–Helmholtz instability. *Phys. Fluids* **23**, 114107.

ORLICZ, G. C., BALASUBRAMANIAN, S. & PRESTRIDGE, K. P. 2013 Incident shock Mach number effects on Richtmyer–Meshkov mixing in a heavy gas layer. *Phys. Fluids* **25** (11), 114101.

PULLIN, D. I. 2000 A vortex-based model for the subgrid flux of a passive scalar. *Phys. Fluids* **12** (9), 2311–2319.

RAMSHAW, J. D. 1990 Self-consistent effective binary diffusion in multicomponent gas mixtures. *J. Non-Equilib. Thermodyn.* **15**, 295–300.

RAYLEIGH, LORD 1883 Investigation of the character of the equilibrium of an incompressible heavy fluid of variable density. *Proc. Lond. Math. Soc.* **14**, 170–177.

REID, R. C., PRANSUITZ, J. M. & POLING, B. E. 1987 *The Properties of Gases and Liquids*. McGraw-Hill.

RICHTMYER, R. D. 1960 Taylor instability in shock acceleration of compressible fluids. *Commun. Pure Appl. Maths* **13**, 297–319.

ROE, P. L. 1981 Approximate Riemann solvers, parameter and difference schemes. *J. Comput. Phys.* **43**, 357–372.

SAFFMAN, P. G. 1967*a* Note on decay of homogeneous turbulence. *Phys. Fluids* **10**, 1349.

SAFFMAN, P. G. 1967*b* The large-scale structure of homogeneous turbulence. *J. Fluid Mech.* **27**, 581–593.

SCHILLING, O. & LATINI, M. 2010 High-order WENO simulations of three-dimensional reshocked Richtmyer–Meshkov instability to late times: dynamics, dependence on initial conditions, and comparisons to experimental data. *Acta Math. Sci.* **30B**, 595–620.

SCHILLING, O., LATINI, M. & DON, W. S. 2007 Physics of reshock and mixing in single-mode Richtmyer–Meshkov instability. *Phys. Rev.* E **76**, 026319.

TACCETTI, J. M., BATHA, S. H., FINCKE, J. R., DELAMATER, N. D., LANIER, N. E., MAGELSSEN, G. R., HUECKSTAEDT, R. M., ROTHMAN, S. D., HORSFIELD, C. J. & PARKER, K. W. 2005 Richtmyer–Meshkov instability reshock experiments using laser-driven double-cylinder implosions. In *High Energy Density Laboratory Astrophysics* (ed. G. A. Kyrala), pp. 327–331. Springer.

TAYLOR, G. 1950 The instability of liquid surfaces when accelerated in a direction perpendicular to their planes. Part 1. Waves on fluid sheets. *Proc. R. Soc. Lond.* A **201**, 192–196.

THORNBER, B., DRIKAKIS, D., YOUNGS, D. L. & WILLIAMS, R. J. R. 2010 The influence of initial conditions on turbulent mixing due to Richtmyer–Meshkov instability. *J. Fluid Mech.* **654**, 99–139.

THORNBER, B., DRIKAKIS, D., YOUNGS, D. L. & WILLIAMS, R. J. R. 2011 Growth of a Richtmyer–Meshkov turbulent layer after reshock. *Phys. Fluids* **23**, 095107.

THORNBER, B., DRIKAKIS, D., YOUNGS, D. L. & WILLIAMS, R. J. R. 2012 Physics of the single-shocked and reshocked Richtmyer–Meshkov instability. *J. Turbul.* **13** (1), N10.

THORNBER, B., MOSEDALE, A., DRIKAKIS, D., YOUNGS, D. & WILLIAMS, R. J. R. 2008 An improved reconstruction method for compressible flows with low Mach number features. *J. Comput. Phys.* **227** (10), 4873–4894.

TOMKINS, C. D., BALAKUMAR, B. J., ORLICZ, G., PRESTRIDGE, K. P. & RISTORCELLI, J. R. 2013 Evolution of the density self-correlation in developing Richtmyer–Meshkov turbulence. *J. Fluid Mech.* **735**, 288–306.

TORO, E. F. 1999 *Riemann Solvers and Numerical Methods for Fluid Dynamics*. Springer.

TRITSCHLER, V. K., AVDONIN, A., HICKEL, S., HU, X. Y. & ADAMS, N. A. 2014 Quantification of initial-data uncertainty on a shock-accelerated gas cylinder. *Phys. Fluids* **26** (2), 026101.

TRITSCHLER, V. K., HICKEL, S., HU, X. Y. & ADAMS, N. A. 2013*a* On the Kolmogorov inertial subrange developing from Richtmyer–Meshkov instability. *Phys. Fluids* **25**, 071701.

TRITSCHLER, V. K., HU, X. Y., HICKEL, S. & ADAMS, N. A. 2013*b* Numerical simulation of a Richtmyer–Meshkov instability with an adaptive central-upwind 6th-order WENO scheme. *Phys. Scr.* **T155**, 014016.

WEBER, C. R., COOK, A. W. & BONAZZA, R. 2013 Growth rate of a shocked mixing layer with known initial perturbations. *J. Fluid Mech.* **725**, 372–401.

WEBER, C., HAEHN, N., OAKLEY, J., ROTHAMER, D. & BONAZZA, R. 2012 Turbulent mixing measurements in the Richtmyer–Meshkov instability. *Phys. Fluids* **24**, 074105.

WEBER, C. R., HAEHN, N. S., OAKLEY, J. G., ROTHAMER, D. A. & BONAZZA, R. 2014 An experimental investigation of the turbulent mixing transition in the Richtmyer–Meshkov instability. *J. Fluid Mech.* **748**, 457–487.

WILCZEK, M., DAITCHE, A. & FRIEDRICH, R. 2011 On the velocity distribution in homogeneous isotropic turbulence: correlations and deviations from gaussianity. *J. Fluid Mech.* **676**, 191–217.

YANG, J., KUBOTA, T. & ZUKOSKI, E. E. 1993 Applications of shock-induced mixing to supersonic combustion. *AIAA J.* **31**, 854–862.

YOUNGS, D. L. 1991 Three-dimensional numerical simulation of turbulent mixing by Rayleigh–Taylor instability. *Phys. Fluids* A: *Fluid Dyn.* **3** (5), 1312–1320.

YOUNGS, D. L. 1994 Numerical simulations of mixing by Rayleigh–Taylor and Richtmyer–Meshkov instabilities. *Laser Part. Beams* **12** (2), 538–544.

YOUNGS, D. L. 2004 Effect of initial conditions on self-similar turbulent mixing. In *Proceedings of the International Workshop on the Physics of Compressible Turbulent Mixing*, vol. 9.

YOUNGS, D. L. 2007 *Implicit Large Eddy Simulation: Computing Turbulent Fluid Dynamics*, pp. 392–412. Cambridge University Press.

ZABUSKY, N. J. 1999 Vortex paradigm for accelerated inhomogeneous flows: visiometrics for the Rayleigh–Taylor and Richtmyer–Meshkov environments. *Annu. Rev. Fluid Mech.* **31**, 495–536.

ZHOU, Y. 2001 A scaling analysis of turbulent flows driven by Rayleigh–Taylor and Richtmyer–Meshkov instabilities. *Phys. Fluids* **13** (2), 538–543.

Evolution of length scales and statistics of Richtmyer-Meshkov instability from direct numerical simulations

V. K. Tritschler,* M. Zubel, S. Hickel, and N. A. Adams
Institute of Aerodynamics and Fluid Mechanics, Technische Universität München, 85747 Garching, Germany
(Received 21 July 2014; published 1 December 2014)

In this study we present direct numerical simulation results of the Richtmyer-Meshkov instability (RMI) initiated by Ma = 1.05, Ma = 1.2, and Ma = 1.5 shock waves interacting with a perturbed planar interface between air and SF_6. At the lowest shock Mach number the fluids slowly mix due to viscous diffusion, whereas at the highest shock Mach number the mixing zone becomes turbulent. When a minimum critical Taylor microscale Reynolds number is exceeded, an inertial range spectrum emerges, providing further evidence of transition to turbulence. The scales of turbulent motion, i.e., the Kolmogorov length scale, the Taylor microscale, and the integral length, scale are presented. The separation of these scales is found to increase as the Reynolds number is increased. Turbulence statistics, i.e., the probability density functions of the velocity and its longitudinal and transverse derivatives, show a self-similar decay and thus that turbulence evolving from RMI is not fundamentally different from isotropic turbulence, though nominally being only isotropic and homogeneous in the transverse directions.

DOI: 10.1103/PhysRevE.90.063001 PACS number(s): 47.20.Ma, 47.27.ek, 47.40.Nm, 47.51.+a

I. INTRODUCTION

The Rayleigh-Taylor instability is an instability that occurs at the material interface between two fluids of different densities when one fluid is accelerated into the other one. In 1950, Taylor [1] provided a theoretical prediction of the growth rate of irregularities on the material interface between two fluids of different densities under constant acceleration. In his pioneering work Richtmyer [2] extended the theory of Taylor [1] to the impulsive acceleration of material interfaces. In the impulsive model of Richtmyer [2] the constant acceleration g of the material interface is replaced by an impulsive acceleration $\Delta u \delta(t)$. According to Richtmyer [2], the amplitude $a(t)$ of a single-mode perturbation with wave number k grows as

$$a(t) = (1 + k\Delta u A^+ t) a_0^+, \tag{1}$$

where $(\cdot)^+$ refers to values after the shock-interface interaction. a_0^+ is the postshock amplitude of the perturbed interface, $A^+ = (\rho_1 - \rho_2)/(\rho_1 + \rho_2)$ is the postshock Atwood number, and t is the time. Later, Richtmyer's theoretical predictions were experimentally verified by Meshkov [3], and the instability is thus known as the Richtmyer-Meshkov instability (RMI).

There are two hypotheses to explain the generation of vorticity at the material interface during shock-interface interaction [4]. The first one is based on baroclinic vorticity production; the other proposes that distorted transmitted and reflected waves create pressure variations across the material interface, which lead to tangential velocity perturbations. According to Brouillette [4] both hypotheses can be formally reconciled by noting that the induced tangential velocity components are responsible for the circulation. For more details see also Wouchuk and Nishihara [5], Wouchuk [6], and Zabusky [7]. The generated vorticity amplifies the initial interface perturbations, and if the initial energy input is sufficient, i.e., at sufficiently high Reynolds numbers, the flow evolves eventually into a turbulent mixing zone.

Because of the high Reynolds numbers and the associated small time and length scales, direct numerical simulations (DNSs) seemed to be unfeasible, and therefore large eddy simulations (LESs) have become the standard simulation approach to RMI [8–14]. Grinstein *et al.* [10] used a grid adaptive Eulerian code with implicit LES (ILES) modeling to study three-dimensional material mixing evolving from RMI. The ILES model combines a second-order Godunov-type scheme with the van Leer flux limiter. In the investigation of Schilling and Latini [11], the authors performed ILES with a high-order WENO scheme to study three-dimensional reshocked RMI to late times. In LES and ILES the energy-containing large scales are resolved and the dynamic interaction of unrepresented small scales with grid-resolved large scales is modeled by a subgrid-scale model. Due to the multiscale properties of RMI underresolved numerical simulations are very sensitive to the underlying numerical scheme, which does not only model the unresolved scales but also captures discontinuities such as shock waves and material interfaces; see Tritschler *et al.* [15].

Some recent investigations showed that the Kolmogorov length scale might be larger than assumed so far. In the experimental investigation of Weber *et al.* [16] the authors provided an estimate for the Kolmogorov length scale of a Ma = 1.5 shock accelerated shear layer. The estimate was obtained from fitting model spectra to the experimental spectra, which resulted in an estimate of 125 μm $\leqslant \eta \leqslant$ 214 μm. Tritschler *et al.* [17] found for the same shock Mach number a similar range for the Kolmogorov length scale 75 μm $\leqslant \eta \leqslant$ 224 μm. Consistent with these estimates Lombardini *et al.* [9] found $\eta \approx 620$ μm for RMI driven by a Ma = 1.05 shock wave and $\eta \approx 72$ μm for Ma = 5 long after the shock-interface interaction. Shortly after the shock-interface interaction the Kolmogorov scale can, however, be considerably smaller, being as small as $\eta \sim O(1)$ μm.

*volker.tritschler@aer.mw.tum.de

For the present investigation the shock tube size is scaled down in order to resolve all relevant length scales for Taylor microscale Reynolds numbers $\mathrm{Re}_\lambda \lesssim 140$. With this setup we are able to provide for the first time fully resolved results of the Richtmyer-Meshkov instability.

The paper is structured as follows: in Sec. II we outline the governing equations, which are solved with the numerical method given in Sec. III. The numerical setup is provided in Sec. IV. The results including grid convergence, the scales of turbulent motion, such as the integral length scale, Taylor microscale, and the Kolmogorov scale, as well as the probability density functions of the velocity and its longitudinal and transverse derivatives are presented in Sec. V. We conclude with a summary of our key findings in Sec. VI.

II. GOVERNING EQUATIONS

We solve the multicomponent Navier-Stokes equations in conservative form

$$\frac{\partial \boldsymbol{U}}{\partial t} + \nabla \cdot \boldsymbol{F}(\boldsymbol{U}) = \nabla \cdot \boldsymbol{F}_v(\boldsymbol{U}), \tag{2}$$

where $\boldsymbol{U}$ are the conserved variables:

$$\boldsymbol{U} = \begin{pmatrix} \rho & \rho \boldsymbol{u} & E & \rho Y_i \end{pmatrix}. \tag{3}$$

The inviscid and viscous fluxes are given by

$$\boldsymbol{F}(\boldsymbol{U}) = \begin{pmatrix} \rho \boldsymbol{u} \\ \rho \boldsymbol{u}\boldsymbol{u} + p\underline{\boldsymbol{\delta}} \\ (E+p)\boldsymbol{u} \\ \rho \boldsymbol{u} Y_i \end{pmatrix}, \quad \boldsymbol{F}_v(\boldsymbol{U}) = \begin{pmatrix} 0 \\ \underline{\boldsymbol{\tau}} \\ \underline{\boldsymbol{\tau}} \cdot \boldsymbol{u} - \boldsymbol{q_c} - \boldsymbol{q_d} \\ -\boldsymbol{J_i} \end{pmatrix}. \tag{4}$$

Here we denote $\boldsymbol{u} = [u_1, u_2, u_3] = [u, v, w]$ as the velocity vector, p as the pressure, E as the total energy, ρ as the mixture density, and Y_i as the mass fraction of species i with $i = 1, 2, \ldots, N$, where N is the total number of species. The identity matrix is $\underline{\boldsymbol{\delta}}$. The viscous stress tensor $\underline{\boldsymbol{\tau}}$ for a Newtonian fluid is

$$\underline{\boldsymbol{\tau}} = \overline{\mu}\,[2\underline{\boldsymbol{S}} - 2/3\underline{\boldsymbol{\delta}}\,(\nabla \cdot \boldsymbol{u})], \tag{5}$$

where $\overline{\mu}$ is the mixture viscosity and $\underline{\boldsymbol{S}}$ is the strain rate tensor. Equation (5) uses Stoke's hypothesis according to which the bulk viscosity is zero. We note that there is controversy in literature about the value of the bulk viscosity of large molecules, and setting it to zero may suppress some aspects of the real flow physics.

According to Fourier's law we define the heat conduction as

$$\boldsymbol{q_c} = -\overline{\kappa} \nabla T, \tag{6}$$

where $\overline{\kappa}$ is the mixture heat conductivity. The interspecies diffusional heat flux [18] is defined as

$$\boldsymbol{q_d} = \sum_{i=1}^{N} h_i \boldsymbol{J_i} \tag{7}$$

with

$$\boldsymbol{J_i} \approx -\rho \left(D_i \nabla Y_i - Y_i \sum_{j=1}^{N} D_j \nabla Y_j \right). \tag{8}$$

D_i indicates the effective binary diffusion coefficient of species i, and h_i is the individual species enthalpy. The equations are closed with the equation of state for an ideal gas

$$p(\rho e, Y_i) = (\overline{\gamma} - 1)\,\rho e, \tag{9}$$

where $\overline{\gamma}$ is the ratio of specific heat capacities of the mixture and e is the internal energy

$$\rho e = E - \frac{\rho}{2}\boldsymbol{u}^2. \tag{10}$$

The ratio of specific heat capacities of the mixture $\overline{\gamma}$ is calculated as

$$\overline{\gamma} = \frac{\overline{c_p}}{\overline{c_p} - \overline{R}}, \quad \text{with} \quad \overline{c_p} = \sum_{i}^{N} Y_i \frac{\gamma_i}{\gamma_i - 1}\overline{R}, \tag{11}$$

where $\overline{R}$ is the specific gas constant of the mixture with $\overline{R} = \mathcal{R}/\overline{M}$ and

$$\overline{M} = \left(\sum_{i}^{N} \frac{Y_i}{M_i} \right)^{-1}. \tag{12}$$

The viscosity and the thermal conductivity of the mixture, $\overline{\mu}$ and $\overline{\kappa}$, are calculated according to [19]

$$\overline{\mu} = \frac{\sum_{i=1}^{N} \mu_i Y_i / M_i^{1/2}}{\sum_{i=1}^{N} Y_i / M_i^{1/2}}, \qquad \overline{\kappa} = \frac{\sum_{i=1}^{N} \kappa_i Y_i / M_i^{1/2}}{\sum_{i=1}^{N} Y_i / M_i^{1/2}}. \tag{13}$$

The species specific viscosity μ_i is calculated from the Chapman-Enskog viscosity model

$$\mu_i = 2.6693 \times 10^{-6} \frac{\sqrt{M_i T}}{\Omega_{\mu,i} \sigma_i^2}, \tag{14}$$

where σ_i is the collision diameter and $\Omega_{\mu,i}$ is the collision integral [20] given as

$$\Omega_{\mu,i} = A(T_i^*)^B + C \exp\{DT_i^*\} + E \exp\{FT_i^*\}, \tag{15}$$

with $A = 1.16145$, $B = -0.14874$, $C = 0.52487$, $D = -0.7732$, $E = 2.16178$, and $F = -2.43787$, where the temperature is normalized by the Lennard-Jones energy parameter $T_i^* = T/(\epsilon/k)_i$.

The thermal conductivity is calculated from the species specific Prandtl number Pr_i as

$$\kappa_i = \frac{\gamma_i}{\gamma_i - 1} R_i \frac{\mu_i}{\mathrm{Pr}_i}, \tag{16}$$

and the mass diffusivities D_i are given by

$$D_i = \frac{\mu_i}{\rho \mathrm{Sc}_i}. \tag{17}$$

III. COMPUTATIONAL METHOD

Classical WENO approaches, albeit being formally high-order accurate, are too dissipative at discontinuities and in turbulent regions of the flow because in these regions the theoretical maximum order is never achieved. In order to reduce the excessive dissipation of classical WENO schemes Hu *et al.* [21] developed an adaptive central-upwind sixth-order accurate WENO scheme (WENO-CU6). This scheme significantly reduces the numerical dissipation, while preserving the shock-capturing properties of classical WENO schemes

and being only slightly computationally more complex than the standard fifth-order WENO scheme. Additionally, Hu and Adams [22] improved the scale separation of the original version, which makes the WENO-CU6 scheme also applicable to underresolved simulations.

In a recent investigation Hu *et al.* [23] introduced a dispersion-dissipation condition for finite-difference schemes. The dispersion-dissipation condition imposes a constraint on dissipation and dispersion errors in order to prevent backscatter of nonresolved spurious scales into the resolved-scale range. The modified version B according to Hu *et al.* [23] of the WENO-CU6 scheme is used in the present investigation.

Flux projection onto local characteristics is applied, which requires the Roe-averaged matrix to be calculated for the full multispecies system in Eq. (2) [24,25]. After reconstruction of the numerical fluxes at the cell boundaries the fluxes are projected back onto the physical field. A local switch to a Lax-Friedrichs flux is used as entropy fix; see, e.g., Toro [26]. Temporal integration is performed by a third-order total variation diminishing Runge-Kutta scheme [27].

The present numerical model has been tested and validated for shock induced turbulent multispecies mixing problems at finite Reynolds numbers [17,28,29]. Moreover, it has been demonstrated that it is a state-of-the-art approach to turbulent mixing processes evolving from RMI [15].

IV. NUMERICAL SETUP

The material interface separating air and SF_6 is accelerated by shock waves propagating with Ma = 1.05, Ma = 1.2, and Ma = 1.5. The corresponding postshock thermodynamic states are calculated from the Rankine-Hugoniot jump conditions with the preshock state defined by the stagnation condition $p_0 = 23\,000$ Pa and $T_0 = 298$ K. The Schmidt number of both gases is Sc = 1 and all other thermodynamic gas properties, which are taken from Poling *et al.* [19], are also constant; see Table I. The shock wave is initialized at $x = -L_x/4$ and propagates in the positive x direction. The transverse width L_{yz} of the shock tube is set to $L_{yz} = 0.01$ m, and periodic boundary conditions are used in the y and z direction. The fine-grid domain of the shock tube extends symmetrically in the positive and negative x direction about $x = 0$ m from $-L_x/2$ to $L_x/2$ with $L_x = 2L_{yz}$. A moving reference frame is applied such that the mixing zone remains within the fine-grid domain. The inflow and outflow boundary conditions are imposed very far from the fine-grid domain in order to avoid shock reflections. Outside of the fine-grid domain the computational grid is coarsened to reduce the computational costs. The fine-grid domain is discretized

TABLE I. Constant thermodynamic properties of air and SF_6.

Property	Air	SF_6
M_i [g mol^{-1}]	28.964	146.057
$(\epsilon/k)_i$ [K]	78.6	222.1
σ_i [Å]	3.711	5.128
γ_i	1.4	1.1
Pr$_i$	0.72	0.9

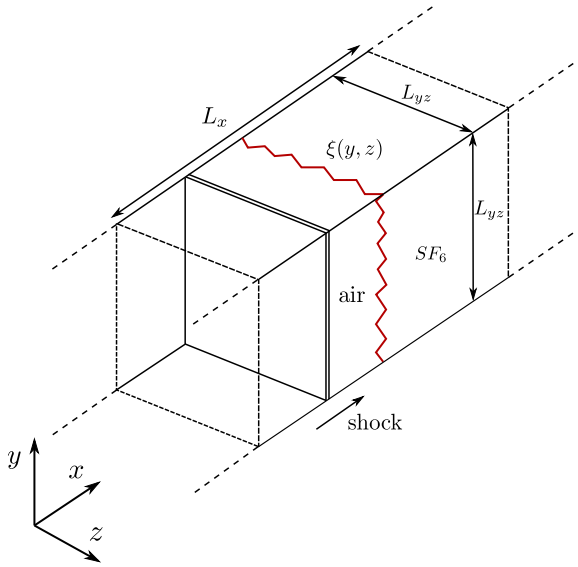

FIG. 1. (Color online) Schematic of the square shock tube showing the dimensions of the computational domain.

by three different grid resolutions $128^2 \times 256$, $256^2 \times 512$, and $512^2 \times 1024$ resulting in cubic cells of size $78\ \mu\text{m} \gtrsim \Delta_{xyz} \gtrsim 19.5\ \mu$m. The three grid resolutions are used for the convergence study, but only the results obtained on the finest grid are presented later. A schematic of the computational domain is given in Fig. 1.

In the present investigation the initial interface perturbation is given by

$$\xi(y,z) = a_1 \sin(k_0 y)\sin(k_0 z) + a_2 \sum_{n=1}^{13}\sum_{m=3}^{15} a_{n,m} \sin(k_n y + \phi_n)\sin(k_m z + \chi_m) \tag{18}$$

with the constant amplitudes $a_1 = -2.5 \times 10^{-4}$ m and $a_2 = 2.5 \times 10^{-5}$ m and wave numbers $k_0 = 10\pi/L_{yz}$, $k_n = 2\pi n/L_{yz}$, and $k_m = 2\pi m/L_{yz}$. The amplitudes $a_{n,m}$ and the phase shifts ϕ_n and χ_m are given by $a_{n,m} = \sin(nm)/2$, $\phi_n = \tan(n)$, and $\chi_m = \tan(m)$.

For the purpose of verifying grid convergence an initial length scale is imposed by a finite initial interface thickness

$$\psi(x,y,z) = \frac{1}{2}\left\{1 + \tanh\left[\frac{x - \xi(y,z)}{L_\rho}\right]\right\} \tag{19}$$

with $L_\rho = 0.001$ m being the characteristic initial thickness. The individual species mass fractions are imposed by $Y_{SF_6} = \psi$ and $Y_{\text{air}} = 1 - \psi$. The time when the shock impacts the perturbed interface is $t = 0$ s.

V. RESULTS

A. Grid convergence

In order to verify the convergence, the average Kolmogorov length scale $\tilde{\eta}$ within the inner mixing zone (imz) according to Tritschler *et al.* [15] as well as the compensated spectra of

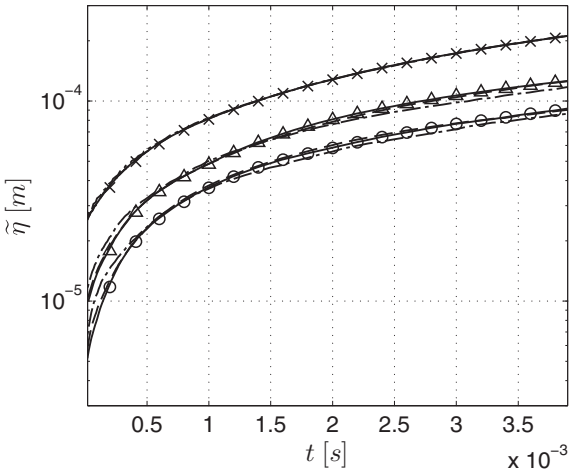

FIG. 2. Average Kolmogorov length scale of the inner mixing zone for Ma = 1.05 (crosses), Ma = 1.2 (triangles), and Ma = 1.5 (circles) computed on three different grid resolutions 128 (dashed-dotted), 256 (dashed), and 512 (solid lines with symbols).

enstrophy $E_\mathcal{E}$ are presented in Fig. 2 and Fig. 3 for the three grid resolutions.

We define the average Kolmogorov length scale as

$$\widetilde{\eta} = \left\langle \left(\frac{\langle \nu \rangle_{yz}^3}{\langle \varepsilon \rangle_{yz}} \right)^{1/4} \right\rangle_x , \tag{20}$$

where ε and ν are the viscous dissipation and the kinematic viscosity and $\langle \cdot \rangle$ denotes spatial averaging. The mean rate of viscous dissipation of kinetic energy is calculated from the single-point correlation of the fluctuating velocity gradients

$$\varepsilon = \nu \left[\frac{\partial u_i''}{\partial x_j} \frac{\partial u_i''}{\partial x_j} + \frac{\partial u_i''}{\partial x_j} \frac{\partial u_j''}{\partial x_i} - \frac{2}{3} \left(\frac{\partial u_i''}{\partial x_i} \right)^2 \right]. \tag{21}$$

For low-order statistics a resolution criterion of $k_{\max}\eta \geqslant 1$ is adequate for DNSs. For higher-order statistics, however, it was found (e.g., Ref. [30]) that a value of $k_{\max}\eta \geqslant 1.5$ is needed. Following this criterion, the finest grid resolution $\Delta_{xyz} \approx 19.5\ \mu$m sufficiently resolves turbulence with a minimal Kolmogorov length scale of $\eta_{min} \approx 9.3\ \mu$m. The average Kolmogorov length scale given in Fig. 2 verifies that for Ma = 1.05 and Ma = 1.2 the DNS resolution requirement is satisfied throughout the simulation on the finest grid resolution. For Ma = 1.5 it is satisfied after a short initial transient $t \gtrsim 130\ \mu$s.

The Kolmogorov length scale reaches a minimum right after the shock passage, which is $\widetilde{\eta} \approx 26\ \mu$m for Ma = 1.05 and decreases as the shock Mach number is increased to $\widetilde{\eta} \approx 5\ \mu$m for Ma = 1.5. After the shock passage the Kolmogorov length scale monotonically increases to $\widetilde{\eta} \approx 211\ \mu$m and $\widetilde{\eta} \approx 92\ \mu$m for Ma = 1.05 and Ma = 1.5, respectively, at the final time.

The compensated enstrophy spectra at $t = 50\ \mu$s, $t = 200\ \mu$s, $t = 500\ \mu$s, $t = 1000\ \mu$s, and $t = 3500\ \mu$s for Ma = 1.05, Ma = 1.2, and Ma = 1.5 are shown in Fig. 3. At Ma = 1.05 the peak enstrophy is fully resolved at all times and for all grid resolutions, whereas at Ma = 1.5 the peak enstrophy is not fully resolved at the earliest time $t = 50\ \mu$s. This is consistent with the average Kolmogorov length scale at these times. For the intermediate shock Mach number Ma = 1.2 the peak enstrophy is resolved on the two finest grids.

Note that enstrophy is a sensitive quantity and that other quantities converge already on coarser grids. From this, we conclude that our simulation results on the finest grid qualify as DNSs.

B. Scales of turbulent motion

The Taylor-microscale Reynolds number is defined as

$$\mathrm{Re}_\lambda = \frac{u''\lambda_T}{\nu}, \tag{22}$$

where u'' is the RMS velocity fluctuation obtained from Reynolds averaging, λ_T is the Taylor microscale, and ν is the kinematic viscosity. According to Dimotakis [31] the Taylor microscale Reynolds number must exceed $\mathrm{Re}_\lambda \geqslant 100$–$140$ or $\mathrm{Re} \geqslant 10^4$, if calculated as an outer-scale Reynolds number, in

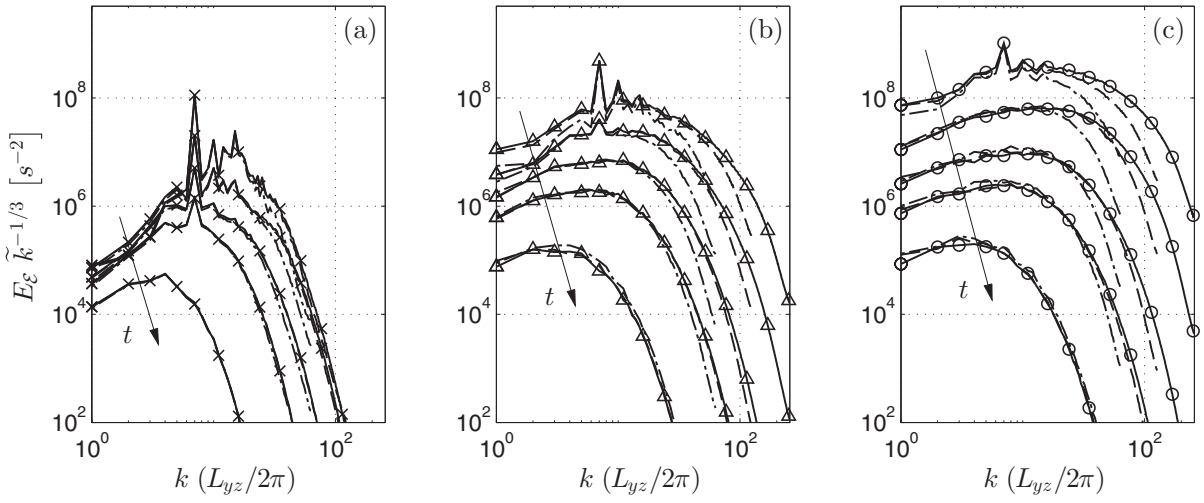

FIG. 3. Compensated enstrophy spectra for Ma = 1.05 (a), Ma = 1.2 (b), Ma = 1.5 (c) at $t = 50\ \mu$s, $t = 200\ \mu$s, $t = 500\ \mu$s, $t = 1000\ \mu$s, and $t = 3500\ \mu$s on three different grid resolutions 128 (dashed-dotted), 256 (dashed), and 512 (solid lines with symbols) with $\widetilde{k} = k\,(L_{yz}/2\pi)$.

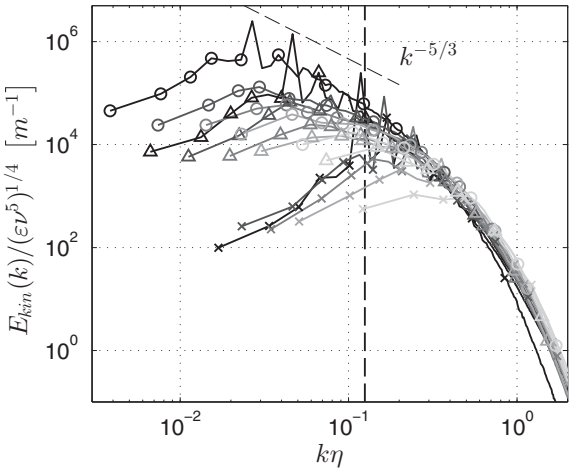

FIG. 4. Normalized turbulence kinetic energy spectra for Ma = 1.05 (crosses), Ma = 1.2 (triangles), and Ma = 1.5 (circles) at $t = 50\ \mu$s, $t = 200\ \mu$s, $t = 500\ \mu$s, $t = 1000\ \mu$s, and $t = 3500\ \mu$s. The gray scale changes from black to light gray as time increases. The dashed vertical line at $k\eta = 1/8$ marks the beginning of the dissipation range.

order to observe fully developed turbulence. When the critical Reynolds number is exceeded a range of scales evolves that is independent from the large scales of motion and free from viscous effects. Only then does the inertial-range similarity concept of Kolmogorov [32] apply. The Taylor microscale Reynolds numbers depicted in Fig. 5 (a) show that for the two higher Mach numbers the Reynolds numbers are $\mathrm{Re}_\lambda \approx 143$ and $\mathrm{Re}_\lambda \approx 47$ after shock passage.

An inner viscous scale λ_ν [31], i.e., the upper limit of the dissipation range, can be estimated from the wave number k_ν where the spectrum begins to deviate from the inertial range spectrum, which is $k_\nu\eta \approx 1/8$ according to Dimotakis [31] who found this value by inspecting the data compilation of Saddoughi and Veeravalli [33]. The turbulence kinetic energy spectra normalized as proposed by Saddoughi and Veeravalli [33] are given in Fig. 4. The dashed line represents the inner viscous wave number according to $k_\nu\eta \approx 1/8$, which verifies that at this wave number all spectra begin to deviate from the inertial range scaling. Figure 4 also verifies that all spectra collapse within the dissipation range in agreement with Kolmogorov's theory.

From $k_\nu\eta \approx 1/8$ the inner viscous scale directly follows as

$$\lambda_\nu = \frac{2\pi}{k_\nu} \approx 50\eta. \tag{23}$$

The upper bound of the uncoupled range, the Liepmann-Taylor scale λ_L, is the smallest scale that can be directly generated from the outer scale δ. Based on experimental data Dimotakis [31] determined that the Liepmann-Taylor scale is proportional to the Taylor-microscale

$$\lambda_L \approx c_L\lambda_T, \tag{24}$$

with c_L as a flow-dependent parameter with a value of around $c_L \approx 5$; cf. Dimotakis [31], Zhou *et al.* [34], and Robey *et al.* [35].

The Taylor microscale λ_T is obtained from the curvature of the transverse spatial covariance of the velocity fluctuations $R_{t,i}(r,t)$ at $r = 0$:

$$\lambda_{T,i}(t) = \left[-\frac{1}{2}\frac{\partial^2 R_{t,i}(0,t)}{\partial r^2}\right]^{-1/2}, \tag{25}$$

with

$$R_{t,i}(r,t) = \frac{\langle u_i''(\vec{x},t)u_i''(\vec{x}+r\vec{e}_{j\neq i},t)\rangle}{\langle u_i''u_i''\rangle}, \quad \text{with} \quad i = 2,3. \tag{26}$$

The transverse covariance is evaluated in the homogeneous directions at each plane in the inner mixing zone with $-3 \leqslant r \leqslant 3$, giving $\lambda_{T,y}$ and $\lambda_{T,z}$. The directional Taylor microscales are averaged in the streamwise x direction, from which the effective mean Taylor microscale is calculated.

Dimotakis [31] argued that an uncoupled range of scales exists when $\lambda_L/\lambda_\nu \geqslant 1$. The uncoupled range is illustrated in Fig. 5(b) evolving between Liepmann-Taylor scale λ_L and the upper limit of the dissipation range λ_ν. In the present study only the highest Mach number case exceeds $\mathrm{Re}_\lambda > 100$ and should therefore exhibit a range of uncoupled scales. At Ma = 1.5 a range of uncoupled scales with $\lambda_L > \lambda_\nu$ evolves for $t \lesssim 400\ \mu$s. At this time the Taylor microscale Reynolds number is $\mathrm{Re}_\lambda \approx 26$, which is smaller than the expected value of $\mathrm{Re}_\lambda > 100 - 140$ according to Dimotakis [31]; see Fig. 5(a). Because

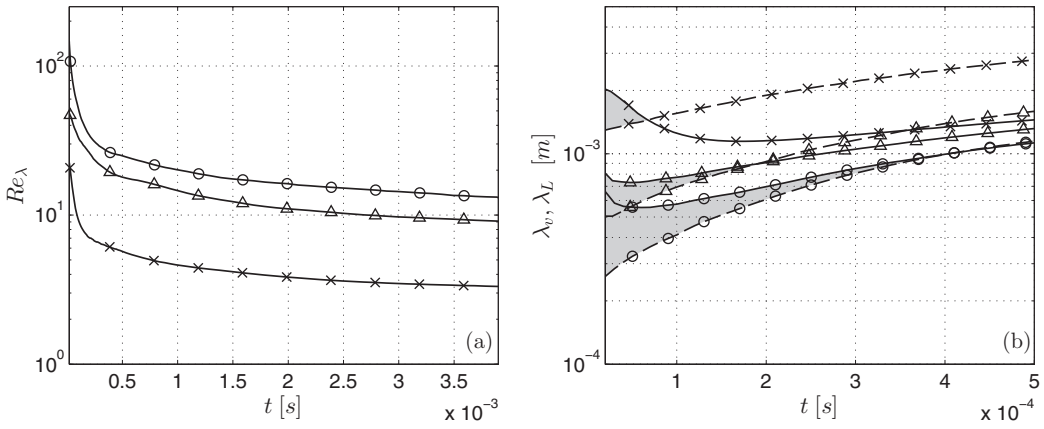

FIG. 5. Taylor microscale Reynolds number and uncoupled range of scales, given by the inner viscous scale λ_ν (dashed) and the Liepmann-Taylor scale λ_L (solid) for Ma = 1.05 (crosses), Ma = 1.2 (triangles), and Ma = 1.5 (circles).

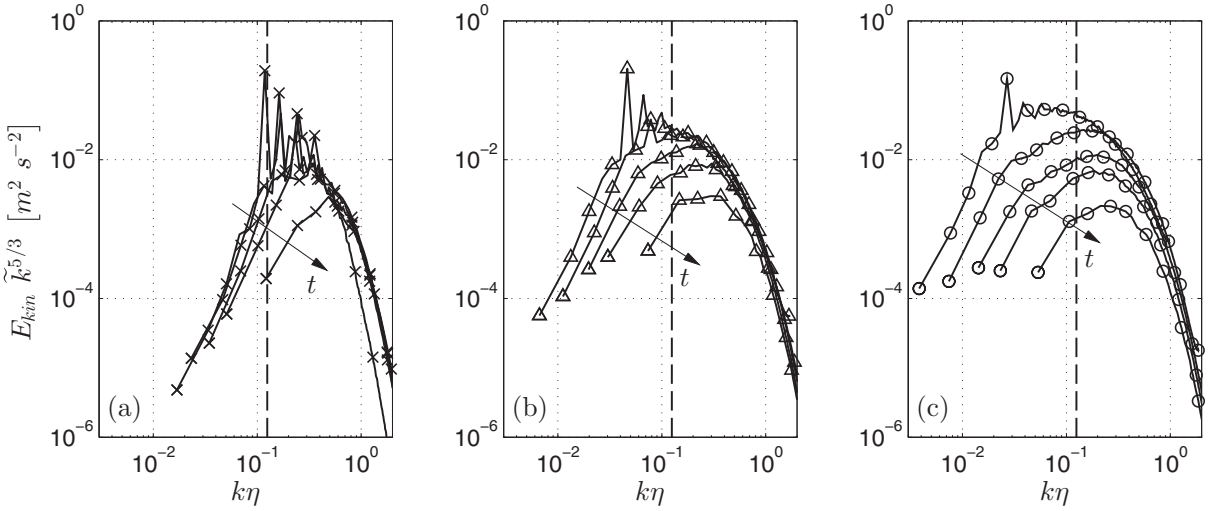

FIG. 6. Compensated spectra of turbulence kinetic energy for Ma = 1.05 (a), Ma = 1.2 (b), Ma = 1.5 (c) at $t = 50\ \mu$s, $t = 200\ \mu$s, $t = 500\ \mu$s, $t = 1000\ \mu$s, and $t = 3500\ \mu$s with $\widetilde{k} = k\eta$. The dashed vertical line at $k\eta = 1/8$ marks the beginning of the dissipation range.

of the uncertainties associated with the estimates for λ_L and λ_v and the shallow intersection of their curves a more realistic value for the critical Reynolds number in the present setup is $\mathrm{Re}_\lambda \gtrsim 35$–$80$.

Scales within the uncoupled range should exhibit a spectral scaling close to a $k^{-5/3}$ scaling. In Fig. 6 we show the compensated spectra of turbulence kinetic energy for all Mach numbers at 50 μs, 200 μs, 500 μs, 1000 μs, and 3500 μs over the Kolmogorov normalized wave number. The dashed line marks the beginning of the dissipation range at $k\eta = 1/8$. As observed in Fig. 5 the lowest Mach number case does not exhibit an uncoupled range of scales beyond $t \geqslant 60\ \mu$s. Accordingly, all scales are either affected by viscous effects or driven by the large-scale motion, such that no scales can become unstable and subsequently turbulent. As can be seen in Fig. 6(a) almost the full spectrum is within the dissipation range, which implies that the growth of the mixing zone is dominated by the large scales of motion and molecular diffusion.

For the medium Mach number, shown in Fig. 6(b), the energy-containing scales are also relatively close to the dissipation range with only a very narrow range of uncoupled scales immediately after the shock-interface interaction; see also Fig. 5(b). The existence of a $k^{-5/3}$ range is not evident, since the dominant wave numbers overlay an eventual inertial range at $t = 50\ \mu$s. At later times the spectrum becomes more shallow than Kolmogorov's scaling.

As the Mach number is increased to Ma = 1.5 an uncoupled range of scales develops during the first $t \approx 400\ \mu$s, which manifests in a narrow inertial range following approximately $k^{-5/3}$ at $t = 50\ \mu$s as can be seen in the compensated energy spectra in Fig. 6(c). At later times, however, an inertial range following $k^{-5/3}$ is not evident anymore. Only a very narrow band of uncoupled scales exists for $t \geqslant 200\ \mu$s, and thus, scales are likely to be either damped by viscous effects or affected by the large scales of motion beyond this time.

Scales within the uncoupled range can become unstable through nonlinear growth and mode coupling, which quickly removes the imprint of the initial perturbation. As seen in Fig. 6(a), if the energy-containing mode initially is in the dissipation range, the modes do not become unstable and are slowly dissipated. At the highest Mach number, Fig. 6(c), the modes become unstable, and the energy-containing mode quickly breaks down into smaller scales leaving no evidence of the initial perturbation.

Figure 7 shows the mixing zone width δ_x and the integral length scale Λ. The integral length scale is calculated from the longitudinal spatial velocity covariance [36]

$$\Lambda_i = \int_0^\infty R_{l,i}(r,t)\,dr, \tag{27}$$

with

$$R_{l,i}(r,t) = \frac{\langle u_i''(\vec{x},t)u_i''(\vec{x}+r\vec{e}_i,t)\rangle}{\langle u_i''u_i''\rangle}, \quad \text{with} \quad i = 2,3. \tag{28}$$

To compute the spatial velocity covariance in the whole domain $R_{l,i}(r,t)$ the Wiener-Khinchin theorem is applied. The theorem states that the autocorrelation function is the inverse Fourier

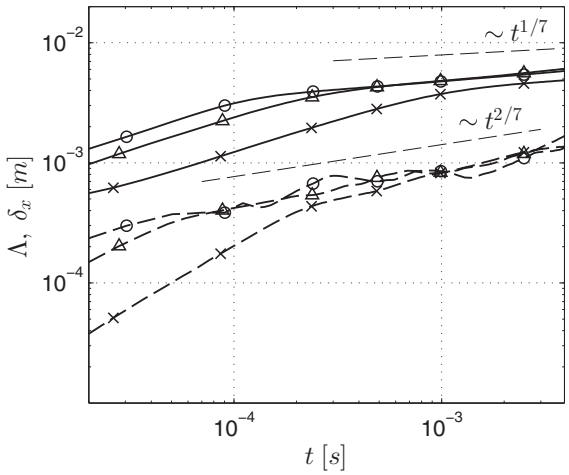

FIG. 7. The mixing zone width δ_x and the integral length scale Λ as a function of time.

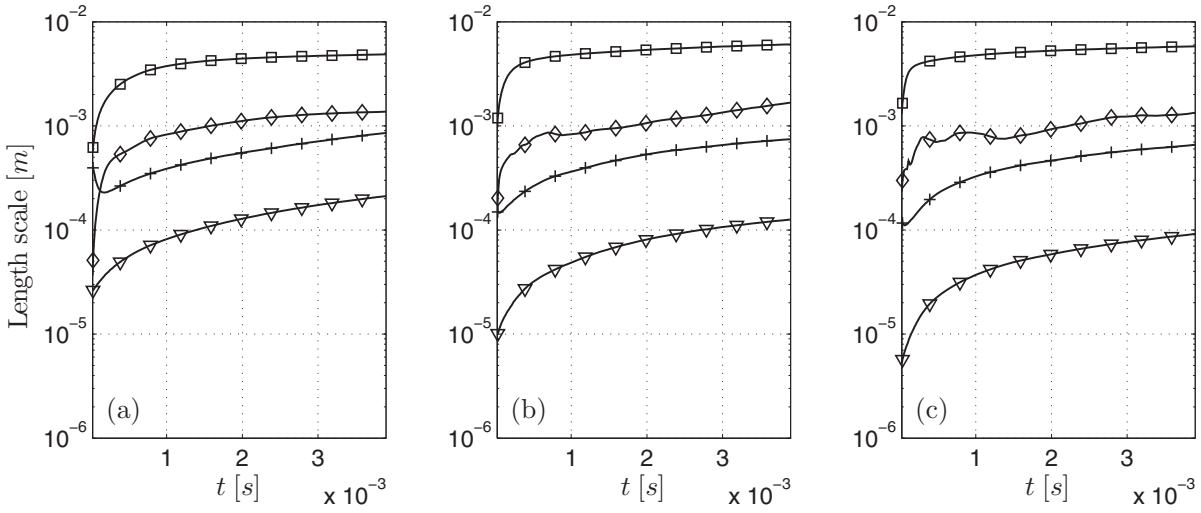

FIG. 8. Summary of length scales for Ma = 1.05 (a), Ma = 1.2 (b), and Ma = 1.5 (c). The solid lines with symbols represent the mixing zone width δ_x (squares), the integral length scale Λ (diamonds), the Taylor microscale λ_T (plus), and the Kolmogorov length scale η (triangles).

transform of its power spectrum

$$R_{l,i}(r,t) = \mathcal{F}^{-1}[\hat{u}_i''^{*}\hat{u}_i'']. \tag{29}$$

Integration of $R_{l,i}(r,t)$ leads to longitudinal integral scales in the y and z direction, Λ_y and Λ_z. The directional integral length scales Λ_i are averaged in the streamwise x direction from which the effective integral length scale Λ is calculated.

The mixing zone width is defined as

$$\delta_x(t) = \int_{-\infty}^{\infty} 4\langle Y_{SF_6}\rangle_{yz}(1 - \langle Y_{SF_6}\rangle_{yz})dx, \tag{30}$$

where $\langle\cdot\rangle_{yz}$ denotes ensemble averaging in the cross-stream yz plane.

The mixing zone width grows approximately proportional to $\sim t^{1/7}$, whereas the integral length scale in the homogeneous directions grows as $\sim t^{2/7}$. Various growth rate exponents Θ have been proposed in the past ranging from $\Theta = 2/7$ [37] to $\Theta = 2/3$ [38]. Our results are in the lower range of previously published data.

A summary of all length scales is given in Fig. 8. It shows the mixing zone width, the integral length scale, the Taylor microscale, and the Kolmogorov length scale for the three investigated shock Mach numbers Ma = 1.05, Ma = 1.2, and Ma = 1.5. Figure 8 verifies the increasing separation of scales with increasing shock Mach number. Weber *et al.* [39] also presented the mixing zone width, the Taylor microscale, and the Kolmogorov length scale obtained from experimental measurements at Ma = 1.6 and Ma = 2.2. In the investigation of Weber *et al.* [39] the separation of scales appears not to depend on the shock Mach number. The Kolmogorov length scale at Ma = 1.5 in our investigation has the same order of magnitude as in the experiment of Weber *et al.* [39].

C. Decaying turbulence

There are two distinct canonical cases of decaying isotropic turbulence which result from the solution of the Kármán-Howarth equation: turbulence of Saffman type with a Birkhoff-Saffman spectrum [40,41] $E(k \to 0) \sim Lk^2$ and turbulence of Batchelor type $E(k \to 0) \sim Ik^4$, where $L = \int\langle \boldsymbol{u} \times \boldsymbol{u'}\rangle d\boldsymbol{r}$ and $I = \int \boldsymbol{r}^2\langle \boldsymbol{u} \times \boldsymbol{u'}\rangle d\boldsymbol{r}$ are known as Saffman and Loitsyansky

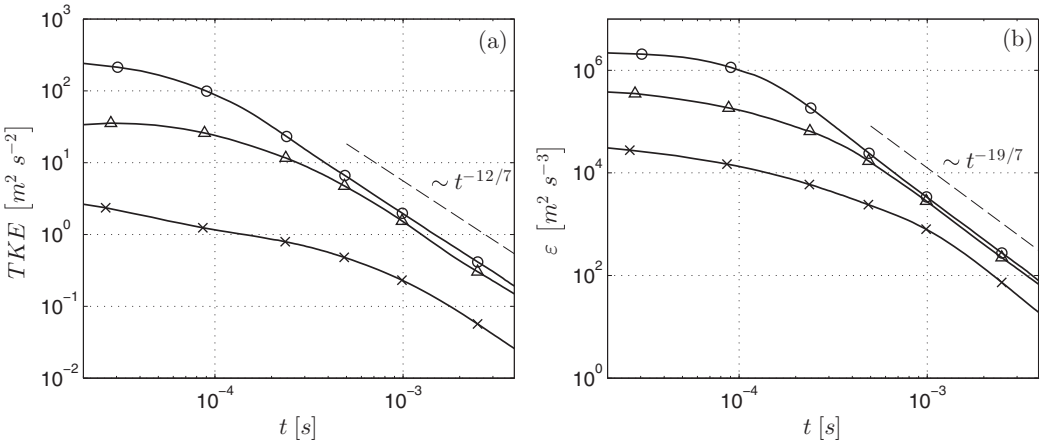

FIG. 9. Average turbulence kinetic energy TKE and viscous dissipation rate ε in the inner mixing zone as functions of time for Ma = 1.05 (crosses), Ma = 1.2 (triangles), and Ma = 1.5 (circles).

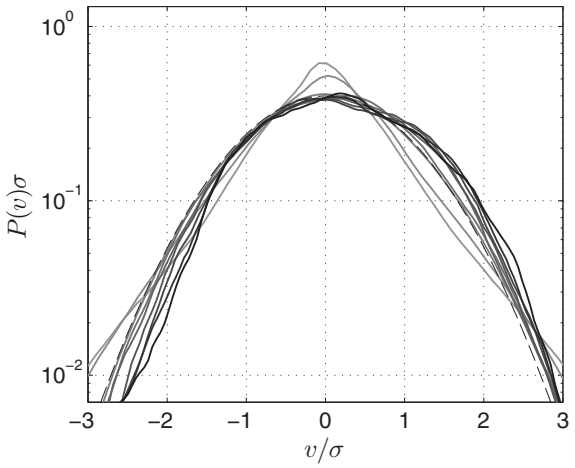

FIG. 10. Normalized probability density functions of the velocity for Ma = 1.5. The gray scale changes from light gray to black as time increases. The Gaussian distribution is given by the dashed line. The PDFs are normalized by their standard deviation σ.

integrals, respectively. These two canonical cases have been derived under the assumption that the triple velocity correlation tensor as well as the pressure-velocity correlation decay fast enough for remote points.

The Saffman integral L is an invariant provided that the triple velocity correlation tensor and the pressure-velocity correlation decay as $O(r^{-2})$ implying that the global linear momentum is conserved. Saffman [41] showed that in this case the Saffman integral is proportional to $L \sim u^2 l^3$. Then the decay of turbulence kinetic energy follows as $u^2 \sim t^{-6/5}$, whereas the integral scale grows proportional to $l \sim t^{2/5}$.

If the long-range statistics become uncorrelated according to $O(r^{-4})$, i.e., if turbulence is dominated by angular momentum with negligible linear momentum the Loitsyansky integral I is conserved [42]. Given that $I = \text{const}$ and that the large scales evolve in a self-similar way, the Loitsyansky integral is proportional to $I \sim u^2 l^5$ [32] implying that the turbulence kinetic energy of isotropic homogeneous turbulence decays as $u^2 \sim t^{-10/7}$, whereas the integral scale grows as $l \sim t^{2/7}$.

Ishida *et al.* [43] reported the kinetic energy of isotropic turbulence to decay as $\sim t^{-n}$ with $n \approx 1.4$, if the Loitsyansky integral is constant and if the Taylor microscale Reynolds number exceeds $\mathrm{Re}_\lambda > 100$. Long-range interactions between remote eddies resulted in a deviation from $I = \text{const}$ and thus in $n \neq 10/7$.

In Fig. 9 the average turbulence kinetic energy in the inner mixing zone is shown for shock Mach numbers Ma = 1.05, Ma = 1.2, and Ma = 1.5. After an initial transient all cases exhibit a decay exponent close to $n = 12/7 \approx 1.71$, which is steeper than predicted by the third hypothesis of Kolmogorov [32], i.e., $n = 10/7$. Ishida *et al.* [43], however, found that $n \to 1.5$ for $\mathrm{Re}_\lambda = 62.5$ and for lower Reynolds numbers ($\mathrm{Re}_\lambda = 31.3$) $n \to 1.63$, while $n \to 10/7$ for $\mathrm{Re}_\lambda = 125$ from which the authors concluded that the Reynolds number must exceed $\mathrm{Re}_\lambda \approx 100$ in order to observe $n = 10/7$. In the present simulations the Taylor microscale Reynolds numbers are $\mathrm{Re}_\lambda \sim O(10)$ for the two higher shock Mach number and $\mathrm{Re}_\lambda \lesssim O(10)$ for Ma = 1.05 at late times as depicted in Fig. 5. For the highest shock Mach number Ma = 1.5 the Taylor microscale Reynolds number is $\mathrm{Re}_\lambda \approx 140$ after shock passage and decays to $\mathrm{Re}_\lambda \approx 20$ at the latest time. Burattini *et al.* [44] found a dependency between the initial Reynolds number $\mathrm{Re}_\lambda(t = 0)$ and the observed decay exponent n of turbulence kinetic energy, that is, $n \to 1$ as $\mathrm{Re}_\lambda(t = 0) \to \infty$. This dependence approximately follows $n = 1.05 + 60/\mathrm{Re}_\lambda(t = 0)$ in good agreement with other data from the literature. For an initial Taylor microscale Reynolds number of $\mathrm{Re}_\lambda(t = 0) \approx 140$ the power-law exponent becomes $n \approx 1.48$ and thus is smaller than the observed value in the present investigation. Samtaney *et al.* [45] investigated decaying compressible turbulence and found for a range of different initial conditions the decay exponent of turbulence kinetic energy to be in the range $1.37 \leqslant n \leqslant 1.71$, which is in good agreement with the present results.

It is interesting to note that all three cases follow the same decay law and do not show a dependence on the initial Reynolds number as observed previously [43,44]. Also, the lowest Mach number case follows $\sim t^{-12/7}$ even though the flow does not become turbulent. Lombardini *et al.* [9] investigated shock-initiated decaying turbulence at various shock Mach numbers ranging from Ma = 1.05 to Ma = 5.

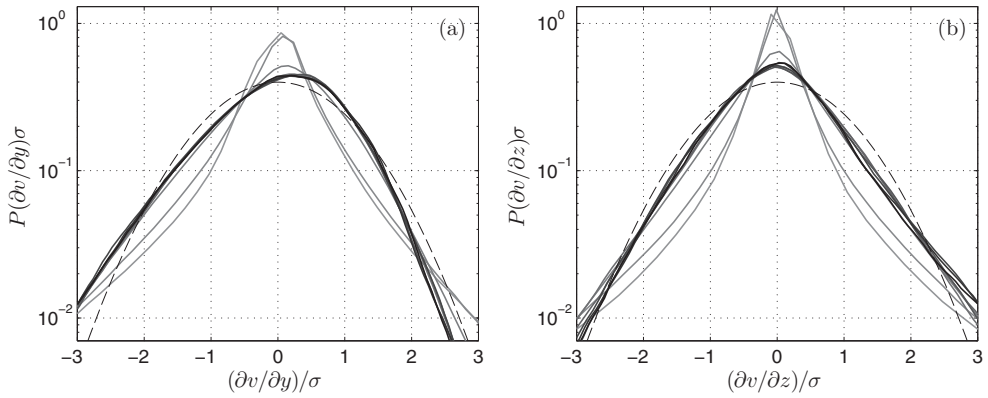

FIG. 11. Normalized probability density function of the longitudinal (a) and transverse velocity gradients (b) for Ma = 1.5. The gray scale changes from light gray to black as time increases. The Gaussian distribution is given by the dashed line. The PDFs are normalized by their standard deviation σ.

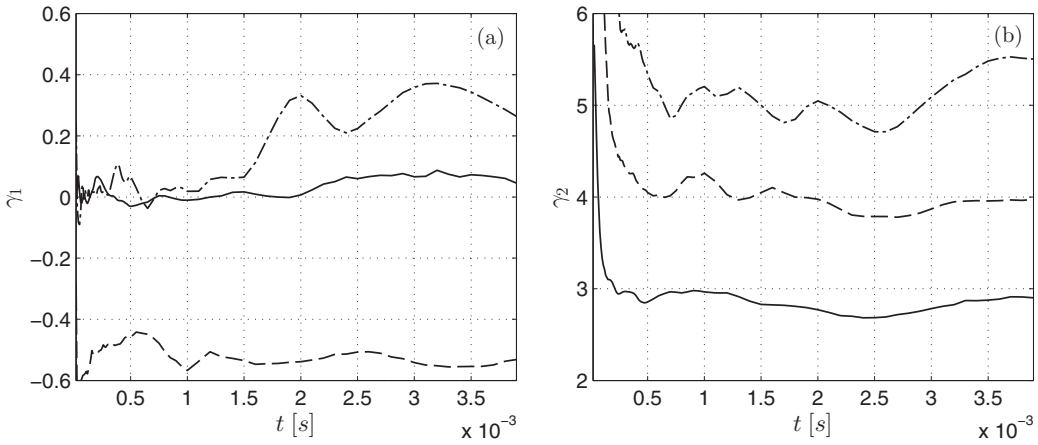

FIG. 12. Skewness (a) and kurtosis (b) of the velocity (solid line), the longitudinal velocity gradient (dashed line), and the transverse velocity gradient (dashed-dotted) for Ma = 1.5.

The turbulence kinetic energy decay was found to be larger than $\sim t^{-6/5}$ and closer to $\sim t^{-10/7}$, independent of the shock Mach number. Tritschler *et al.* [15] also found the decay of turbulence kinetic energy to be proportional to $\sim t^{-10/7}$.

Figure 9(b) shows the average viscous dissipation rate in the inner mixing zone as a function of time. The viscous dissipation rate decays as $\sim t^{-19/7}$, consistent with the decay of turbulence kinetic energy.

D. Probability density functions

According to the theory of Kolmogorov, the probability density function (PDF) of the velocity field of homogeneous isotropic turbulence exhibits a Gaussian normal distribution. However, Batchelor [46] showed that velocity gradients, especially for scales that are close to the dissipation limit, do not satisfy the assumption of uncorrelated long-range interactions.

Jiménez *et al.* [47] investigated the vorticity statistics of forced isotropic turbulence at Taylor microscale Reynolds numbers ranging from $\mathrm{Re}_\lambda = 35$ to $\mathrm{Re}_\lambda = 170$. This work indicates that the PDF of the single-point vorticity and the PDF of strain of isotropic turbulence is non-Gaussian and shows growing tails with increasing Reynolds numbers. Furthermore, the tails of the PDF do not show an asymptotic behavior for the limiting case $\mathrm{Re} \to \infty$. Despite the deviations from Gaussianity and the lack of an asymptotic behavior, the spectra showed a $k^{-5/3}$ decay law and a dissipation range as predicted by Kolmogorov. Jiménez *et al.* [47] explained this observation with long coherent vortices ("worms"). The authors state that these worms are part of the background vorticity and responsible for a large amount of turbulent dissipation. The worms themselves, however, are only responsible for a small fraction of kinetic energy which is proportional to the volume fraction that they occupy.

Wilczek *et al.* [48] found that decaying and forced turbulence do not differ fundamentally, since the velocity component PDFs show self-similarity when normalized by the respective standard deviation. Furthermore, the vorticity distribution exhibits an intermittent behavior as reported by Jiménez *et al.* [47]. The velocity distribution deviates from a Gaussian distribution with sub-Gaussian tails, implying a kurtosis of $\gamma_2 < 3$.

We show the statistics of the velocity and the transverse and longitudinal velocity gradients of the Ma = 1.5 case in Fig. 10 and Fig. 11. At lower Mach numbers the PDF show qualitatively a similar behavior as the PDFs for a shock Mach number of Ma = 1.5.

The PDFs are normalized by their respective standard deviation σ. At later times the PDFs collapse, indicating a self-similar decay as proposed previously [48]; see Fig. 10. The PDFs of velocity are approximately Gaussian, with a kurtosis slightly below that of the Gaussian distribution, i.e., $\gamma_2 \approx 2.8$. This is in very good agreement with previous results [47] for sustained isotropic turbulence, which found $\gamma_2 = 2.8$ for $\mathrm{Re}_\lambda = 35.1$. The skewness is expected to be zero in isotropic turbulence. In the present case, it fluctuates around zero before finally deviating to $\gamma_1 > 0$ and approaching $\gamma_1 \approx 0.05$ at later times; see Fig. 12(a) and Fig. 12(b).

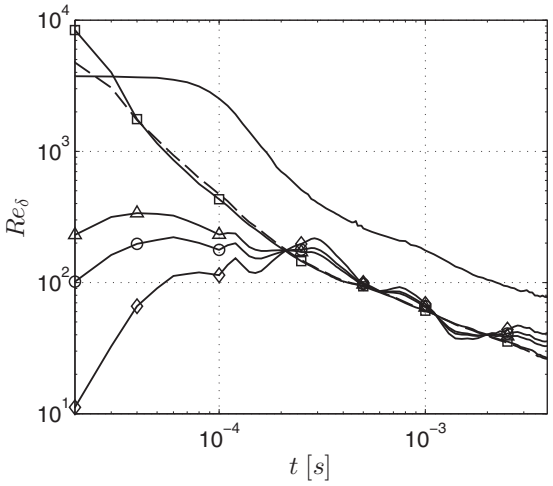

FIG. 13. Temporal evolution of different Reynolds number approximations for a shock Mach number of Ma = 1.5 [36] and as given in Table II.

TABLE II. Reynolds number approximations for a shock Mach number of Ma = 1.5 [36].

Re_δ	$\frac{\delta_x \dot{\delta_x}}{\nu}$	$\left(\frac{\Lambda}{\eta}\right)^{4/3}$	$\frac{\mathrm{TKE}^{1/2}\Lambda}{\nu}$	$\left(\frac{\sqrt{10}\Lambda}{\lambda_T}\right)^2$	$\frac{1}{100}\left(\frac{\lambda_T}{\eta}\right)^4$	$\frac{3}{20}\mathrm{Re}_\lambda^2$
$\mathrm{Re}_\delta(t = 200\ \mu\mathrm{s})$	701	171	176	165	183	188
Symbol	Solid	Circle	Triangle	Diamond	Square	Dashed

The PDFs of the velocity gradients are clearly non-Gaussian with long tails. The values of the statistical moments γ_1, γ_2 are in very good agreement with that observed previously [47]. For the longitudinal velocity gradient $\partial v/\partial y$, shown in Fig. 11(a), we find the skewness and kurtosis [see Fig. 12(a) and Fig. 12(b)] to be only slightly smaller than that given by Ref. [47] at $\mathrm{Re}_\lambda = 35.1$ ($\gamma_1 = -0.49$, $\gamma_2 = 4.2$) and Ref. [45] ($-0.5 \leqslant \gamma_1 \leqslant -0.4$) and in very good overall agreement. Note that the Taylor microscale Reynolds number is $\mathrm{Re}_\lambda \approx 15$–$25$ at later times, which is smaller than the lowest Reynolds number investigated in Ref. [47] of $\mathrm{Re}_\lambda = 35.1$.

The transverse velocity gradient $\partial v/\partial z$ shows good agreement with that of Ref. [47], but begins to deviate at later times becoming more skewed. The kurtosis γ_2 of the transverse velocity gradient agrees well with the value in Ref. [47], which found $\gamma_2 = 5.7$ for $\mathrm{Re}_\lambda = 35.1$.

Inspecting the compensated spectra of turbulence kinetic energy, shown in Fig. 6, it is evident that for times $t > 1000\ \mu$s, the spectrum is very shallow with a large portion within the dissipation range. The present data suggest that RMI exhibits features of isotropic turbulence, provided that the energy injected by the shock wave is strong enough to create a range of uncoupled scales, which is the case in the present investigation for $\mathrm{Re}_\lambda \gtrsim 35$–$80$.

E. Outer-scale Reynolds number

For Richtmyer-Meshkov unstable flows the outer-scale Reynolds number is estimated from the mixing zone width δ_x and its growth rate $\dot{\delta_x}$ according to

$$\mathrm{Re}_\delta = \frac{\delta_x \dot{\delta_x}}{\nu}. \tag{31}$$

The temporal evolution of Re_δ as given in Eq. (31) together with length scale approximations for isotropic turbulence as given in Ref. [36] are shown in Fig. 13 and listed in Table II. As also reported in Ref. [39] the approximation given in Eq. (31) overestimates the true Reynolds number in RMI, see Table II. $\mathrm{Re}_\delta = 3/20\mathrm{Re}_\lambda^2$ can be considered as reference since it is derived from the exact definition of the Taylor microscale Reynolds number. According to the outer-scale Reynolds number approximations given in Table II the Reynolds number is in the range $165 \lesssim \mathrm{Re}_\delta \lesssim 188$ at $t = 200\ \mu$s.

VI. CONCLUSION

Because direct numerical simulations (DNSs) of experimental-scale setups are beyond todays computational resources, DNSs on a reduced computational domain were performed. For this reduced computational domain we have presented fully resolved DNS results for the Richtmyer-Meshkov instability evolving from a deterministic multimode planar interface. The interface was accelerated by three different shock waves of strength Ma = 1.05, Ma = 1.2, and Ma = 1.5.

While at the lowest Mach number the dominant modes slowly mix with the ambient fluid by viscous diffusion, a turbulent mixing zone is obtained at the highest shock Mach number. An uncoupled range of scales evolves associated with the emergence of a narrow Kolmogorov inertial subrange for $t \lesssim 200\ \mu$s at Ma = 1.5. The Taylor microscale Reynolds number decreases after the shock passage from $\mathrm{Re}_\lambda \approx 143$ to $\mathrm{Re}_\lambda \approx 13$ at the final time. Increasing the shock Mach number leads to larger Taylor microscale Reynolds numbers, and the scales of turbulent motion become more and more separated.

The growth of integral scale and mixing zone width as well as the decay rates of turbulence kinetic energy and enstrophy are independent of the shock Mach number and in good agreement with values known from decaying isotropic turbulence.

Probability density functions of the velocity and its longitudinal and transverse derivatives are also in agreement with those for decaying isotropic turbulence.

We conclude that turbulence evolving from the Richtmyer-Meshkov instability is not fundamentally different from decaying isotropic turbulence despite being only isotropic and homogeneous in two spatial directions. This is particularly true when the Reynolds number exceeds a critical value and the flow becomes turbulent. The critical Taylor microscale Reynolds number was found to be $\mathrm{Re}_\lambda \gtrsim 35$–$80$ for the investigated relatively low shock Mach numbers.

ACKNOWLEDGMENTS

V.K.T. thanks S. K. Lele and B. J. Olson for many fruitful discussions and for valuable insights. We want to acknowledge the Gauss Centre for Supercomputing e.V. for providing computing time on the GCS Supercomputer SuperMUC at Leibniz Supercomputing Centre.

[1] G. Taylor, Proc. R. Soc. Lond. A **201**, 192 (1950).
[2] R. D. Richtmyer, Comm. Pure Appl. Math. **13**, 297 (1960).
[3] E. E. Meshkov, Fluid Dyn. **4**, 101 (1969).
[4] M. Brouillette, Annu. Rev. Fluid Mech. **34**, 445 (2002).
[5] J. G. Wouchuk and K. Nishihara, Phys. Plasmas **4**, 1028 (1997).
[6] J. G. Wouchuk, Phys. Rev. E, **63**, 056303 (2001).
[7] N. J. Zabusky, Annu. Rev. Fluid Mech., **31**, 495 (1999).
[8] D. J. Hill, C. Pantano, and D. I. Pullin, J. Fluid Mech. **557**, 29 (2006).
[9] M. Lombardini, D. I. Pullin, and D. I. Meiron, J. Fluid Mech. **690**, 203 (2012).
[10] F. F. Grinstein, A. A. Gowardhan, and A. J. Wachtor, Phys. Fluids **23**, 034106 (2011).
[11] O. Schilling and M. Latini, Acta Math. Scientia **30**, 595 (2010).

[12] B. Thornber, D. Drikakis, D. L. Youngs, and R. J. R. Williams, Phys. Fluids **23**, 095107 (2011).
[13] J.-S. Bai, J.-H. Liu, T. Wang, L.-Y. Zou, P. Li, and D.-W. Tan, Phys. Rev. E **81**, 056302 (2010).
[14] J.-S. Bai, B. Wang, T. Wang, and K. Liu, Phys. Rev. E **86**, 066319 (2012).
[15] V. K. Tritschler, B. J. Olson, S. K. Lele, S. Hickel, X. Y. Hu, and N. A. Adams, J. Fluid Mech. **755**, 429 (2014).
[16] C. Weber, N. Haehn, J. Oakley, D. Rothamer, and R. Bonazza, Phys. Fluids **24**, 074105 (2012).
[17] V. K. Tritschler, S. Hickel, X. Y. Hu, and N. A. Adams, Phys. Fluids **25**, 071701 (2013).
[18] A. W. Cook, Phys. Fluids **21**, 055109 (2009).
[19] B. E. Poling, J. M. Prausnitz, and J. P. O'Connell, *The Properties of Gases and Liquids* (McGraw-Hill, New York, 2001).
[20] P. D. Neufeld, A. R. Janzen, and R. A. Aziz, J. Chem. Phys. **57**, 1100 (1972).
[21] X. Y. Hu, Q. Wang, and N. A. Adams, J. Comp. Phys. **229**, 8952 (2010).
[22] X. Y. Hu and N. A. Adams, J. Comp. Phys. **230**, 7240 (2011).
[23] X. Y. Hu, V. K. Tritschler, S. Pirozzoli, and N. A. Adams, arXiv:1204.5088.
[24] P. L. Roe, J. Comp. Phys. **43**, 357 (1981).
[25] B. Larouturou and L. Fezoui, in *Nonlinear Hyperbolic Problems*, Lecture Notes in Mathematics vol. 1402 (Springer, Berlin, 1989), p. 69.
[26] E. F. Toro, *Riemann Solvers and Numerical Methods for Fluid Dynamics* (Springer, Berlin, 1999).
[27] S. Gottlieb and C.-W. Shu, Math. Comp. **67**, 73 (1998).
[28] V. K. Tritschler, X. Y. Hu, S. Hickel, and N. A. Adams, Phys. Scr. T **155**, 014016 (2013).
[29] V. K. Tritschler, A. Avdonin, S. Hickel, X. Y. Hu, and N. A. Adams, Phys. Fluids **26**, 026101 (2014).
[30] P. Yeung and S. Pope, J. Fluid Mech. **207**, 531 (1989).
[31] P. E. Dimotakis, J. Fluid Mech. **409**, 69 (2000).
[32] A. N. Kolmogorov, Dokl. Akad. Nauk SSSR **31**, 538 (1941).
[33] S. G. Saddoughi and S. V. Veeravalli, J. Fluid Mech. **268**, 333 (1994).
[34] Y. Zhou, H. F. Robey, and A. C. Buckingham, Phys. Rev. E **67**, 056305 (2003).
[35] H. Robey, Y. Zhou, A. Buckingham, P. Keiter, B. Remington, and R. Drake, Phys. Plasmas **10**, 614 (2003).
[36] S. B. Pope, *Turbulent Flows* (Cambridge University Press, Cambridge, 2000).
[37] A. Llor, European J. Mech. B **30**, 480 (2011).
[38] D. L. Youngs, Laser Part. Beams **12**, 725 (1994).
[39] C. R. Weber, N. S. Haehn, J. G. Oakley, D. A. Rothamer, and R. Bonazza, J. Fluid Mech. **748**, 457 (2014).
[40] G. Birkhoff, Comm. Pure Appl. Math. **7**, 19 (1954).
[41] P. G. Saffman, J. Fluid Mech. **27**, 581 (1967).
[42] L. G. Loitsyansky, Trudy Tsentr. Aero.-Giedrodin Inst. **440**, 3 (1939).
[43] T. Ishida, P. A. Davidson, and Y. Kaneda, J. Fluid Mech. **564**, 455 (2006).
[44] P. Burattini, P. Lavoie, A. Agrawal, L. Djenidi, and R. A. Antonia, Phys. Rev. E **73**, 066304 (2006).
[45] R. Samtaney, D. I. Pullin, and B. Kosovic, Phys. Fluids **13**, 1415 (2001).
[46] G. K. Batchelor, *The Theory of Homogeneous Turbulence* (Cambridge University Press, Cambridge, 1953).
[47] J. Jiménez, A. A. Wray, P. G. Saffman, and R. S. Rogallo, J. Fluid Mech. **255**, 65 (1993).
[48] M. Wilczek, A. Daitche, and R. Friedrich, J. Fluid Mech. **676**, 191 (2011).

C. Bibliography

R. Abgrall. How to Prevent Pressure Oscillations in Multicomponent Flow Calculations: A Quasi Conservative Approach. *J. Comp. Phys.*, 160(125):150–160, 1996.

R. Abgrall and K. Smadar. Computations of compressible multifluids. *J. Comp. Phys.*, 169(2):594–623, 2001.

Y. Aglitskiy, A. L. Velikovich, M. Karasik, N. Metzler, S. T. Zalesak, A. J. Schmitt, L. Phillips, J. H. Gardner, V. Serlin, J. L. Weaver, and S. P. Obenschain. Basic hydrodynamics of richtmyer–meshkov-type growth and oscillations in the inertial confinement fusion-relevant conditions. *Philosophical Transactions of the Royal Society A: Mathematical, Physical and Engineering Sciences*, 368(1916):1739–1768, 2010.

A. S. Almgren, J. B. Bell, C. A. Rendleman, and M. Zingale. Low Mach number modeling of type Ia supernovae I. Hydrodynamics. *The Astrophysical Journal*, 637:922, 2006.

J. D. Anderson et al. *Computational fluid dynamics*, volume 206. Springer, 1995.

D. Arnett. The role of mixing in astrophysics. *Ap. J. Suppl.*, 127:213, 2000.

W. D. Arnett, J. N. Bahcall, R. P. Kirshner, and E. W. Stanford. Supernova 1987a. *Annu. Rev. Astrom. Astrophys.*, 27:629, 1989.

J.-S. Bai, B. Wang, T. Wang, and K. Liu. Numerical simulation of the richtmyer-meshkov instability in initially nonuniform flows and mixing with reshock. *Phys. Rev. E*, 86: 066319, 2012.

B. J. Balakumar, G. C. Orlicz, C. D. Tomkins, and K. P. Prestridge. Dependence of growth patterns and mixing width on initial conditions in Richtmyer–Meshkov unstable fluid layers. *Phys. Scr.*, T132, 2008.

S. Balasubramanian, G. C. Orlicz, K. P. Prestridge, and B. J. Balakumar. Experimental study of initial condition dependence on Richtmyer-Meshkov instability in the presence of reshock. *Physics of Fluids*, 24:034103, 2012.

M. Brouillette. The Richtmyer-Meshkov instability. *Annu. Rev. Fluid Mech.*, (34):445–468, 2002.

M. Brouillette and B. Sturtevant. Experiments on the Richtmyer-Meshkov instability: single-scale perturbations on a continuous interface. *J. Fluid Mech.*, 263:271–292, 1994.

R. H. Cohen, W. P. Dannevik, A. M. Dimits, D. E. Eliason, A. A. Mirin, Y. Zhou, D. H. Porter, and P. R. Woodward. Three-dimensional simulation of a Richtmyer–Meshkov instability with a two-scale initial perturbation. *Physics of Fluids*, 14(10):3692, 2002.

B. D. Collins and J. W. Jacobs. PLIF flow visualization and measurements of the Richtmyer–Meshkov instability of an air/SF6 interface. *J. Fluid Mech.*, 464:113, 2002.

A. W. Cook. Enthalpy diffusion in multicomponent flows. *Physics of Fluids*, 21:055109, 2009.

P. E. Dimotakis. The mixing transition in turbulent flows. *J. Fluid Mech.*, 409:6998, 2000.

D. Drikakis. Advances in turbulent flow computations using high-resolution methods. *Progress in Aerospace Sciences*, 39(6–7):405 – 424, 2003.

D. Drikakis, M. Hahn, A. Mosedale, and B. Thornber. Large eddy simulation using high-resolution and high-order methods. *Philosophical Transactions of the Royal Society A: Mathematical, Physical and Engineering Sciences*, 367(1899):2985–2997, 2009.

R. P. Fedkiw, B. Merriman, and S. Osher. High accuracy numerical methods for thermally perfect gas flows with chemistry. *J. Comp. Phys.*, 190:175, 1997.

J. H. Ferziger and M. Perić. *Computational methods for fluid dynamics*, volume 3. Springer Berlin, 2002.

P. Glaister. An approximate linearised riemann solver for the Euler equations for real gases. *J. Comp. Phys.*, 74(2):382–408, 1988.

S. Gottlieb and C.-W. Shu. Total variation diminishing Runge-Kutta schemes. *Math. Comp.*, 67:73, 1998.

F. F. Grinstein, A. A. Gowardhan, and A. J. Wachtor. Simulations of Richtmyer–Meshkov instabilities in planar shock-tube experiments. *Physics of Fluids*, 034106(23), 2011.

J.-F. Haas and B. Sturtevant. Interaction of weak shock waves with cylindrical and spherical gas inhomogeneities. *J. Fluid Mech.*, 181:41, 1987.

A. Harten, B. Engquist, S. Osher, and S. R. Chakravarthy. Uniformly High Order Accurate Essentially Non-oscillatory Schemes. *J. Comp. Phys.*, 71:231–303, 1987.

F. Herning and L. Zipperer. Calculation of the viscosity of technical gas of the individual gases. *Gas & Wasserfach*, 79(49), 1936.

S. Hickel and J. Larsson. An adaptive local deconvolution model for compressible turbulence. *Center for Turbulence Research Proceedings of the Summer Program*, 2008.

S. Hickel, N. A. Adams, and J. A. Domaradzki. An adaptive local deconvolution method for implicit LES. *J. Comput. Phys.*, 213(1):413–436, 2006.

D. J. Hill and D. I. Pullin. Hybrid tuned center-difference-WENO method for large eddy simulations in the presence of strong shocks. *J. Comp. Phys.*, 194:435–450, 2004.

D. J. Hill, C. Pantano, and D. I. Pullin. Large-eddy simulation and multiscale modelling of a Richtmyer–Meshkov instability with reshock. *J. Fluid Mech.*, 557:29, 2006.

X. Y. Hu and N. A. Adams. Scale separation for implicit large eddy simulation. *J. Comp. Phys.*, 230(19):7240, 2011.

X. Y. Hu, N. A. Adams, and G. Iaccarino. On the HLLC Riemann solver for interface interaction in compressible multi-fluid flow. *J. Comp. Phys.*, 228(17):6572–6589, 2009.

X. Y. Hu, Q. Wang, and N. A. Adams. An adaptive central-upwind weighted essentially non-oscillatory scheme. *J. Comp. Phys.*, 229(23):8952, 2010.

X. Y. Hu, V. K. Tritschler, S. Pirozzoli, and N. A. Adams. Dispersion-dissipation condition for finite difference schemes. *arXiv*, 2014.

O. A. Hurricane, D. A. Callahan, D. T. Casey, P. M. Celliers, C. Cerjan, E. L. Dewald, T. R. Dittrich, T. Döppner, D. E. Hinkel, L. F. B. Hopkins, et al. Fuel gain exceeding unity in an inertially confined fusion implosion. *Nature*, 2014.

N. A. Ingogamov. The role of Rayleigh-Taylor and Richtmyer-Meshkov instabilities in astrophysics. *Astrophysics and Space Physics Reviews*, 10:1–335, 1999.

J. W. Jacobs and V. V. Krivets. Experiments on the late-time development of single-mode Richtmyer–Meshkov instability. *Physics of Fluids*, 17(3):034105, 2005.

M. A. Jones and J. W. Jacobs. A membraneless experiment for the study of Richtmyer-Meshkov instability of a shock-accelerated gas interface. *Physics of Fluids*, 9:3078, 1997.

J. Kane, R. Drake, and B. Remington. An Evaluation of the Richtmyer-Meshkov Instability in Supernova Remant Formation. *The Astrophysical Journal*, 511:335–340, 1999.

S. Karni. Multicomponent flow calculations by a consistent primitive algorithm. *J. Comp. Phys.*, 112:31–43, 1994.

S. Karni. Hybrid Multifluid Algorithms. *SIAM J. Sci. Comput.*, 17(5):1019, 1996.

A. M. Khokhlov, E. S. Oran, and G. O. Thomas. Numerical simulation of deflagration-to-detonation transition: the role of shock–flame interactions in turbulent flames. *Combustion and Flame*, 117(1–2):323 – 339, 1999.

B. Kosović, D. I. Pullin, and R. Samtaney. Subgrid-scale modeling for large-eddy simulations of compressible turbulence. *Physics of Fluids*, 14(4):1511–1522, 2002.

B. Larouturou and L. Fezoui. On the equations of mulit-component perfect or real gas inviscid flow. *Lecture Notes in Mathematics*, 1402:69, 1989.

M. Latini, O. Schilling, and W. S. Don. Effects of WENO flux reconstruction order and spatial resolution on reshocked two-dimensional Richtmyer–Meshkov instability. *J. Comp. Phys.*, 221(2):805, 2007a.

M. Latini, O. Schilling, and W. S. Don. High-resolution simulations and modeling of reshocked single-mode Richtmyer-Meshkov instability: Comparison to experimental data and to amplitude growth model predictions. *Physics of Fluids*, 19(2):024104, 2007b.

J. D. Lindl, R. L. McCrory, and E. M. Campbell. Progress toward ignition and burn propagation in inertial confinement fusion. *Physics Today*, 45(9):32–40, 1992.

M.-S. Liou, B. van Leer, and J.-S. Shuen. Splitting of inviscid fluxes for real gases. *J. Comp. Phys.*, 87(1):1–24, 1990.

X.-D. Liu, S. Osher, and T. Chan. Weighted essentially non-oscillatory schemes. *Journal of Computational Physics*, 115(1):200 – 212, 1994.

M. Lombardini, D. J. Hill, D. I. Pullin, and D. I. Meiron. Atwood ratio dependence of Richtmyer-Meshkov flows under reshock conditions using large-eddy simulations. *J. Fluid Mech.*, 670:439–480, 2011.

M. Lombardini, D. I. Pullin, and D. I. Meiron. Transition to turbulence in shock-driven mixing: a Mach number study. *J. Fluid Mech.*, 690:203, 2012.

E. E. Meshkov. Instability of the interface of two gases accelerated by a shock wave. *Fluid Dyn.*, 4:151, 1969.

K. O. Mikaelian. Turbulent mixing generated by Rayleigh-Taylor and Richtmyer-Meshkov instabilities. *Physica D: Nonlinear Phenomena*, 36(3):343 – 357, 1989.

K. O. Mikaelian. Explicit expressions for the evolution of single-mode Rayleigh-Taylor and Richtmyer-Meshkov instabilities at arbitrary Atwood numbers. *Physical Review E*, 67(2):026319, 2003.

P. D. Neufeld, A. R. Janzen, and R. A. Aziz. Empirical Equations to Calculate 16 of the Transport Collision Integrals $\omega^{(l,s)*}$ for the Lennard-Jones (12-6) Potential. *The Journal of Chemical Physics*, 57(3):1100–1102, 1972.

G. C. Orlicz, S. Balasubramanian, and K. P. Prestridge. Incident shock Mach number effects on Richtmyer-Meshkov mixing in a heavy gas layer. *Physics of Fluids*, 25(11): 114101, 2013.

B. E. Poling, J. M. Prausnitz, and J. P. O'Connell. *The Properties of Gases and Liquids*. McGraw-Hill, New York, 2001.

K. Prestridge, P. Vorobieff, P. M. Rightley, and R. F. Benjamin. Validation of an instability growth model using particle image velocimetry measurements. *Phys. Rev. Lett.*, 84:4353–4356, 2000.

K. Prestridge, G. Orlicz, S. Balasubramanian, and B. J. Balakumar. Experiments of the Richtmyer-Meshkov instability. *Philosophical Transactions of the Royal Society A: Mathematical, Physical and Engineering Sciences*, 371(2003), 2013.

D. I. Pullin. A vortex-based model for the subgrid flux of a passive scalar. *Physics of Fluids*, 12(9):2311–2319, 2000.

J. J. Quirk and S. Karni. On the dynamics of a shock-bubble interaction. *Journal of Fluid Mechanics*, 318:129–163, 7 1996.

J. D. Ramshaw. Self-consistent effective binary diffusion in multicomponent gas mixtures. *J. Non-Equilib. Thermodyn.*, 15:295, 1990.

L. Rayleigh. Investigation of the character of the equilibrium of an incompressible heavy fluid of variable density. *Proc. Lond. Math. Soc.*, 14:170–177, 1883.

R. D. Richtmyer. Taylor instability in shock acceleration of compressible fluids. *Communications on pure and applied mathematics*, 13:297, 1960.

P. L. Roe. Approximate Riemann Solvers, Parameter and Difference Schemes. *J. Comp. Phys.*, 43:357, 1981.

P. Sagaut. *Large eddy simulation for incompressible flows*. Springer, 2002.

O. Schilling and M. Latini. High-order WENO simulations of three-dimensional reshocked Richtmyer-Meshkov instability to late times: Dynamics, dependence on initial conditions, and comparisons to experimental data. *Acta Math. Scientia*, 30B:595–620, 2010.

O. Schilling, M. Latini, and W. S. Don. Physics of reshock and mixing in single-mode Richtmyer-Meshkov instability. *Phys. Rev. E*, 76(026319):1, 2007.

S. K. Shankar, S. Kawai, and S. K. Lele. Two-dimensional viscous flow simulation of a shock accelerated heavy gas cylinder. *Physics of Fluids*, 23(2):024102, 2011.

C.-W. Shu. Essentially Non-Oscillatory and Weighted Essentially Non-Oscillatory Schemes for Hyperbolic Conservation Laws, 1997.

K.-M. Shyue. A fluid-mixture type algorithm for compressible multicomponent flow with Mie-Grüneisen equation of state. *J. Comp. Phys.*, 171(2):678–707, 2001.

A. J. Smits. *A physical introduction to fluid mechanics*. John Wiley, 2000.

J. M. Taccetti, S. H. Batha, J. R. Fincke, N. D. Delamater, N. E. Lanier, G. R. Magelssen, R. M. Hueckstaedt, S. D. Rothman, C. J. Horsfield, and K. W. Parker. Richtmyer-meshkov instability reshock experiments using laser-driven double-cylinder implosions. In G. Kyrala, editor, *High Energy Density Laboratory Astrophysics*, pages 327–331. Springer Netherlands, 2005.

G. Taylor. The instability of liquid surfaces when accelerated in a direction perpendicular to their planes. Part 1. Waves on fluid sheets. *Proc. R. Soc. Lond. A*, 201:192–196, 1950.

B. Thornber, A. Mosedale, D. Drikakis, D. Youngs, and R. Williams. An improved reconstruction method for compressible flows with low mach number features. *J. Comp. Phys.*, 227(10):4873 – 4894, 2008.

B. Thornber, D. Drikakis, D. L. Youngs, and R. J. R. Williams. The influence of initial conditions on turbulent mixing due to Richtmyer–Meshkov instability. *J. Fluid Mech.*, 654:99, 2010.

B. Thornber, D. Drikakis, D. L. Youngs, and R. J. R. Williams. Growth of a Richtmyer-Meshkov turbulent layer after reshock. *Physics of Fluids*, 23:095107, 2011.

C. Tomkins, S. Kumar, G. Orlicz, and K. Prestridge. An experimental investigation of mixing mechanisms in shock-accelerated flow. *J. Fluid Mech.*, 611:131, 2008.

E. F. Toro. *Riemann solvers and numerical methods for fluid dynamics*. Springer, Berlin, 1999.

V. K. Tritschler, S. Hickel, X. Y. Hu, and N. A. Adams. On the Kolmogorov inertial subrange developing from Richtmyer-Meshkov instability. *Physics of Fluids*, 25:071701, 2013a.

V. K. Tritschler, X. Y. Hu, S. Hickel, and N. A. Adams. Numerical simulation of a Richtmyer-Meshkov instability with an adaptive central-upwind 6th-order WENO scheme. *Phys. Scr.*, T155:014016, 2013b.

V. K. Tritschler, A. Avdonin, S. Hickel, X. Y. Hu, and N. A. Adams. Quantification of initial-data uncertainty on a shock-accelerated gas cylinder. *Physics of Fluids*, 26(2): 026101, 2014a.

V. K. Tritschler, B. J. Olson, S. K. Lele, S. Hickel, X. Y. Hu, and N. A. Adams. Numerical simulation of the Richtmyer-Meshkov instability evolving from a generic multimode planar interface. *J. Fluid Mech.*, 755:429–462, 2014b.

V. K. Tritschler, M. Zubel, S. Hickel, X. Y. Hu, and N. A. Adams. Evolution of length scales and statistics of Richtmyer-Meshkov instability from direct numerical simulations. *Phys. Rev. E*, 90:063001, 2014c.

H. K. Versteeg and W. Malalasekera. *An introduction to computational fluid dynamics: the finite volume method*. Pearson Education, 2007.

C. Weber, N. Haehn, J. Oakley, D. Rothamer, and R. Bonazza. Turbulent mixing measurements in the Richtmyer-Meshkov instability. *Physics of Fluids*, 24:074105, 2012.

C. R. Weber, N. S. Haehn, J. G. Oakley, D. A. Rothamer, and R. Bonazza. An experimental investigation of the turbulent mixing transition in the Richtmyer-Meshkov instability. *J. Fluid Mech.*, 748:457–487, 6 2014.

C. R. Wilke. A viscosity equation for gas mixtures. *The Journal of Chemical Physics*, 18 (4):517–519, 1950.

J. Yang, T. Kubota, and E. E. Zukoski. Applications of shock-induced mixing to supersonic combustion. *AIAA J.*, 31:854, 1993.

Q. Yang, J. Chang, and W. Bao. Richtmyer-Meshkov instability induced mixing enhancement in the Scramjet combustor with a central strut. *Advances in Mechanical Engineering*, 2014.

Q. Zhang and S.-I. Sohn. Nonlinear theory of unstable fluid mixing driven by shock wave. *Physics of Fluids*, 9(4):1106–1124, 1997.